

Tic
8005120 209

NUREG/CR-1112
SAND79-2057
Vol. 12
R3

Light Water Reactor Safety Research Program Quarterly Report April-June 1979 Volume 12

Marshall Berman

12555031337 2 WNRJ
US NRC
SECY PUBLIC DOCUMENT ROOM
BRANCH CHIEF
HST LOBBY
WASHINGTON DC 20555

Printed February 1980



Sandia Laboratories

SF 2000 (17-73)

Prepared for
U. S. NUCLEAR REGULATORY COMMISSION

THIS DOCUMENT CONTAINS
POOR QUALITY PAGES

NOTICE

This report was prepared as an account of work sponsored by an agency of the United States Government. Neither the United States Government nor any agency thereof, or any of their employees, makes any warranty, expressed or implied, or assumes any legal liability or responsibility for any third party's use, or the results of such use, or any information, apparatus, product or process disclosed in this report, or represents that its use by such third party would not infringe privately owned rights.

The views expressed in this report are not necessarily those of the U. S. Nuclear Regulatory Commission.

Available from
National Technical Information Service
Springfield, VA 22161

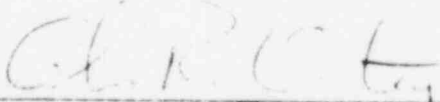
NUREG/CR-1112
SAND79-2057
Vol. 12
R3

LIGHT WATER REACTOR SAFETY RESEARCH PROGRAM
QUARTERLY REPORT APRIL-JUNE 1979
Volume 12

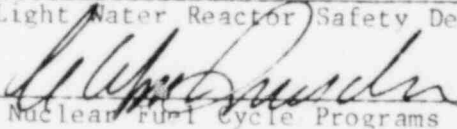
Marshall Berman, Person in Charge

Manuscript Submitted: October 1979
Date Published: February 1980

Approved:



Manager, Light Water Reactor Safety Department



Director, Nuclear Fuel Cycle Programs

Sandia Laboratories
Albuquerque, NM 87185
Operated by
Sandia Laboratories
for the
U.S. Department of Energy

Prepared for
Division of Reactor Safety Research
Office of Nuclear Regulatory Research
U.S. Nuclear Regulatory Commission
Washington, DC 20555
Under Memorandum of Understanding DOE 40-550-75
NRC FIN Nos. A-1019, -1030, -1205, -1207, -1216

Contributing Authors:

W. B. Benedick	L. S. Dike
M. Berman	M. A. Ellis
F. G. Blottner	D. E. Mitchell
B. M. Bulmer	J. F. Muir
L. D. Buxton	L. S. Nelson
R. K. Byers	D. A. Powers
R. K. Cole, Jr.	G. P. Steck
M. L. Corradini	W. R. Trebilcock
	R. Woodfin

CONTENTS

	<u>Page</u>
1. Molten Core/Concrete Interactions Study	13
1.1 Summary	13
1.2 Molten Core/Concrete Interaction Experimental Program	14
1.3 Molten Core/Concrete Interaction Analytical Program	32
1.4 References	50
2. Steam Explosion Phenomena	53
2.1 Summary	53
2.2 Small-Scale Experiments	57
2.3 Open-Geometry Test Series	66
2.4 Fully Instrumented Test Series	66
2.5 Theoretical Analysis	67
2.6 Assessment of Containment Failure Capability	83
2.7 References	91
3. Statistical LOCA Analysis	93
3.1 Summary	93
3.2 RELAP Blowdown Calculations and Statistical Analysis	93
3.3 Statistical LOCA Program - TRAC Progress	112
3.4 References	113
4. UHI Model Development	115
4.1 Summary	115
4.2 TRAC Progress	116
4.3 RELAP Reflood Progress	124
4.4 References	141
5. Two-Phase Jet Loads	143
5.1 Summary	143
5.2 Comparisons of TRAC-PLA Results With Battelle-Frankfurt Research Project RS-50	144
5.3 Sonic Plane Locations Using CSQ	148

CONTENTS (cont)

		<u>Page</u>
5.4	Containment Modelling Using the TRAC-PIA Vessel Component	152
5.5	Current and Future Work	165
5.6	References	166

ILLUSTRATIONS

Figure

1-1	Model Results for Blast Furnace Problem Without Convergence Forcing	25
1-2	Model Results for Blast Furnace Problem With Convergence Forcing	25
1-3	Bubble Size as a Function of Superficial Gas Velocity	35
1-4	Terminal Velocity Variations for Single Bubbles Rising Through Several Liquids	38
1-5	Upward Gas Flow	40
1-6	Example Void Fraction Variations for Representative Oxidic and Metallic Melts	41
1-7	Molten Pool-Concrete Cavity Configuration With Pool Interior-to-Boundary Heat Transfer Regions	42
1-8	Heat Transfer for Surfaces With Bubble Agitation	45
1-9	Heat Transfer for Surfaces With Gas Injection	46
1-10	Liquid/Liquid Interface Heat Transfer With Gas Bubbling - Slag-Metal	48
1-11	Liquid/Liquid Interface Heat Transfer With Gas Bubbling - Oil-Water	48
2-1	Bubbles of Noncondensing Gas Generated by Molten Iron Drop Injected Into Water Subcooled 95 K	58
2-2	Bubbles of Noncondensing Gas Generated by Molten Zirconia Drop Injected Into Water Subcooled ≈ 75 K	60
2-3	The Compositions of Dissociating Water Vapor at Thermodynamic Equilibrium	60
2-4	Scanning Electron Micrographs of Debris in Cross Section Retrieved From a Steam Explosion Involving a Single Drop of Laser-Melted Iron Oxide	62

ILLUSTRATIONS (cont)

<u>Figure</u>		<u>Page</u>
2-5	Scanning Electron Micrographs of Debris in Cross Section Retrieved From a Steam Explosion Involving a Single Drop of Laser-Melted Aluminum Oxide	63
2-6	Peak Pressures, P_p , Recorded for Bridgewire Pressure Transients as a Function of Firing Voltage	64
2-7	Schematic Description of the Shock Tube	69
2-8	Variance of the Peak Heat Flux Due to Wall Heater Temperature	70
2-9	Variance of the Peak Heat Flux Due to Ambient Pressure	71
2-10	Variance of the Peak Heat Flux Due to Shock Pressure	71
2-11	Variance of the Peak Heat Flux Due to Shock Rise Time	72
2-12	Initial Geometry for a Mercury Drop in Water	74
2-13	Shock Tube Pressure in the Water Upstream of the Mercury Droplet	74
2-14	Pressure Within Mercury 0.12 cm Downstream of the Droplet Center	75
2-15	Pressure Within Mercury 0.18 cm Downstream of the Droplet Center	75
2-16	Propagation Phase; a Mechanistic View	80
2-17	Simple Model for Heat Transfer Between Fuel and Coolant After Local Film Collapse	81
2-18	Experiment 11-2-1 Results and Comparison With the Simple Model	82
2-19	Artist's Conception of Interaction Vessel With Honeycomb Blocks and Melt Generator Installed	84
2-20	Slug Kinetic Energy as a Function of the Initial Coolant Vapor Pressure With and Without Heat Transfer	85
2-21	Transient Pressure Comparison of the Simple Expansion Model to Open Geometry Test No. 43 With and Without Heat Transfer	85
2-22	Idealized Schematic of the Vapor-Liquid Expansion After the Explosion	86
2-23	Full Scale Slug Kinetic Energy With and Without Heat Transfer	87
2-24	Full Scale Slug Kinetic Energy as a Function of the Coolant Vapor Pressure ($M_c \approx 1000$ kg)	88

ILLUSTRATIONS (cont)

<u>Figure</u>		<u>Page</u>
2-25	Full Scale Slug Kinetic Energy as a Function of the Coolant Vapor Pressure ($M_c \approx 4000$ kg)	88
2-26	Full Scale Slug Kinetic Energy as a Function of the Coolant Mass	89
3-1	RELAP4 Nodalization for Statistical Study	94
3-2	Surface Temperature, Slab 14; Effect of CHF Multiplier	96
3-3	Surface Temperature, Slab 15; Effect of CHF Multiplier	97
3-4	Surface Temperature, Slab 16; Effect of CHF Multiplier	97
3-5	Fuel Stored Energy; CHFx3 and CHFx1	98
3-6	Pump Side Break Flow; CHFx3 and CHFx1	98
3-7	Intact Loop Accumulator Flow; CHFx3 and CHFx1	99
3-8	Flow at Midplane of Average Core; CHFx3 and CHFx1	99
3-9	Intact Loop Pump Torque; Effect of Loss of Pump Power	101
3-10	Broken Loop Pump Torque; Effect of Loss of Pump Power	101
3-11	Intact Loop Pump Head; Effect of Loss of Pump Power	102
3-12	Broken Loop Pump Head; Effect of Loss of Pump Power	102
3-13	Intact Loop Pump Outlet Flow; Effect of Loss of Pump Power	103
3-14	Broken Loop Pump Outlet Flow; Effect of Loss of Pump Power	103
3-15	Flow at Midplane of Hot Channel; Effect of Loss of Pump Power	104
3-16	Quality at Midplane of Hot Channel; Effect of Loss of Pump Power	105
3-17	Surface Temperature, Slab 16; Effect of Loss of Pump Power	105
3-18	Volume Temperature in Hot Channel; Effect of Loss of Pump Power	106
3-19	Intact Loop Pump Speed; Effect of Loss of Pump Power	106
3-20	Broken Loop Pump Speed; Effect of Loss of Pump Power	107
4-1	Cross Section Through Vessel 13	119
4-2	UHI Drain Test Nodalization	121
4-3	Mixture Velocity in Broken Loop Pump	123
4-4	RELAP4/MOD5-FLOOD Nodalization	124
4-5	Core Mixture Level; Hot vs Cold Rod Conditions	126

ILLUSTRATIONS (cont)

<u>Figure</u>		<u>Page</u>
4-6	Core Inlet Flow; Hot vs Cold Rod Conditions	127
4-7	Core Mixture Level; Effect of Core Exit Enthalpy (Cold Rod)	128
4-8	Core Inlet Flow; Effect of Core Exit Enthalpy (Cold Rod)	129
4-9	Core Mixture Level; Effect of Core Exit Enthalpy (Cold Rod) (Closeup)	129
4-10a	Core Mixture Level; Effect of Core Exit Enthalpy (Hot Rod)	131
4-10b	Core Mixture Level; Effect of Core Exit Enthalpy (Hot Rod) (Closeup)	131
4-11	Core Mixture Level; Effect of CRF Discontinuity (Closeup)	132
4-12	Core Mixture Level; Effect of CRF Discontinuity	133
4-13	Core Mixture Level; No Accumulator Fill vs 30-s Fill	133
4-14	Core Mixture Level; No Accumulator Fill vs 30-s Fill (Closeup)	134
4-15	Core Mixture Level; Effect of Water Pack Option	135
4-16	Core Mixture Level; Effect of Water Pack Option (Closeup)	135
4-17	Core Mixture Level; Effect of Flow Error Correction	136
4-18	Downcomer Nodalization	137
4-19	Downcomer Mixture Level; Effect of Flow Error Correction	139
4-20	Typical CRF Profile	140
5-1	Battelle-Frankfurt RS-50 Circulation System	144
5-2	Battelle-Frankfurt RS-50 Nozzle Configuration	145
5-3	TRAC 6 Component RS-50 Model	146
5-4	RS-50 Pressure Calculation	147
5-5	RS-50 TRAC Force Calculation	147
5-6	CSQ Blowdown Model	148
5-7	CSQ Sonic Plane Location (5-cm pipe)	149
5-8	CSQ Sonic Plane Location (15-cm pipe)	149
5-9	CSQ Sonic Plane Location (5-cm 2-D pipe)	150
5-10	CSQ Sonic Plane Location (5-cm 2-D pipe)	151
5-11	CSQ Velocities (5-cm 1-D pipe)	151
5-12	TRAC-PIA KWU Model	153

ILLUSTRATIONS (cont)

<u>Figure</u>		<u>Page</u>
5-13	Top View of Vessel Showing Four-Angle Seven-Ring Model	154
5-14	TRAC-PIA Static Pressure; Cell 4, Level 15	156
5-15	TRAC-PIA Static Pressure; Cell 4, Level 15 (Closeup)	157
5-16	TRAC-PIA Static Pressure; Cell 1, Level 12	157
5-17	TRAC-PIA Static Pressure; Cell 1, Level 13	158
5-18	TRAC-PIA Static Pressure; Cell 1, Level 14	158
5-19	TRAC-PIA Static Pressure; Cell 1, Level 15	159
5-20	TRAC-PIA Density (0.000000 s)	160
5-21	TRAC-PIA Density (0.005000 s)	160
5-22	TRAC-PIA Density (0.010023 s)	161
5-23	TRAC-PIA Density (0.035001 s)	161
5-24	TRAC-PIA Void Fraction; Cell 1, Level 15	162
5-25	TRAC-PIA Void Fraction; Cell 1, Level 14	162
5-26	TRAC-PIA Void Fraction; Cell 1, Level 13	163
5-27	TRAC-PIA Axial Pressure Profile (T = 120 ms)	163
5-28	TRAC-PIA Static Plate Pressure	164

TABLES

<u>Table</u>		
1-I	Comparison of Results From the Model With Literature Results for the Pyrolysis of Propane in Varying Amounts of Air	27
1-II	Comparison of Results of Model With Results Published by Others for the Blast Furnace Problem	28
1-III	Effect of Initial Guess on the Solution Obtained for the Blast Furnace Problem	30
1-IV	Chemical Species To Be Considered in Chemical Equilibria Calculations in CO	31
1-V	Flow Regimes and Gas Velocities for Air Bubbling Through Water	33
1-VI	Critical Velocities	34
1-VII	Equivalent Spherical Radius of Bubbles	35

TABLES (cont)

<u>Table</u>		<u>Page</u>
1-VIII	Bubble Properties	36
1-IX	Natural Convective Heat Transfer	44
2-I	Analytical Results for Sample 10-39-2	65
3-I	Seven Most Important Variables	108
3-II	Response Surface CG-II	109
3-III	Relative Importance of Input Variables to PCT Surface for CG-II Model	110
3-IV	Influence of 1σ Parameter Variations ($^{\circ}$ F) (CG-II Response Surface)	111
3-V	Influence of 1% Parameter Variations ($^{\circ}$ F) (CG-II Response Surface)	111
3-VI	Influence of 1σ Parameter Variation ($^{\circ}$ F) With Parameters at Off-Nominal Conditions (CC-II Response Surface)	112
4-I	Steady-State Values for UHI Drain Test	122
4-II	FLOOD Parameter Study Calculations	125
5-I	Axial Segment Locations	154
5-II	Ring Locations	155

LIGHT WATER REACTOR SAFETY RESEARCH PROGRAM
QUARTERLY REPORT, APRIL - JUNE 1979

1. Molten Core/Concrete Interactions Study

1.1 Summary

The Molten Core/Concrete Interactions Study was begun on July 15, 1975 as a qualitative, extensive exploration of the phenomena associated with contact between molten core materials and concrete. The experimental elements of this study are divided into four categories:

- Deposition of corium-type melts onto concrete
- Kinetics and stoichiometry of the thermal decomposition of concrete
- Response of concrete to high heat fluxes at one surface
- Simulation experiments which explore phenomena at the interface between a melt and a decomposing solid

Experiment results are being incorporated in a computer model of the interaction. The model will be utilized to establish scaling parameters for the system and identify key elements of the melt/concrete interaction. A project description of the study was issued in October 1975.¹

Efforts during the quarter were devoted primarily to the analytical portion of the program. These activities emphasized phenomenological model development and computer programming for the improved molten core/concrete interaction code, CORCON.

A subroutine that allows highly accurate descriptions of chemical interactions between gases and a core melt has been tested and implemented. The routine will be used to determine the rate at which oxidation

depletes the metallic phase of the melt, the heat contributed to the melt by these reactions, and transformations in the gas-phase so that the properties of gases at the melt/concrete interface may be realistically estimated.

A review of the thermal hydraulics of melts with gas injection has been completed and a summary is presented below. This review led to predictions that the flow regime that is produced by concrete decomposition gases entering a core melt would vary between laminar bubbling and a transitional regime between laminar and film bubbling. These predictions are in keeping with experiment results obtained earlier by using x-ray image intensification to monitor the behavior of high temperature melts in contact with concrete. The predictions and experiment verification may call into question the importance of the gas film model for melt-to-concrete heat transfer.

Other aspects of the review bring together existing correlations for heat transfer within and from the melt. The serious absence of experimental data to confirm the validity of the correlations for melt/concrete interactions is made readily apparent in the review.

1.2 Molten Core/Concrete Interaction Experimental Program (D. A. Powers)

1.2.1 Experimental Activities

Two tests in the BURN series were completed during this report period. These tests, BURN 5 and BURN 6, exposed concrete to core debris (heated inductively) at about half the rate used in tests BURN 2 and BURN 3. Results will be used to compile power-vs-erosion rate curves for basalt and for limestone concretes. Data reduction for the large-scale melt/concrete interactions tests is almost complete but other activities have delayed assembling the data into a comprehensible format. These delays are not expected to affect release of the data report in autumn 1979.

A crucible has been fabricated for the standard COIL test; it will be used along with a German test to compare computer models of melt/concrete interactions. The crucible has a 45-point thermocouple array to measure temperature and erosion rates; it also has a three-station moisture migration sensor. The crucible will be used in a test in September 1979 and the data necessary for model predictions of test results will be made available at that time.

1.2.2 Gas-Melt Thermodynamic Equilibrium Model

Power et al² has shown that the metallic phases of molten core materials are responsible for far more attack on concrete than the oxidic phases during melt/concrete interaction. The aggressive behavior of the metallic phases has been rationalized as due to high thermal conductivity with the consequent ability to transfer heat to the concrete.

The metallic phases are, however, not thermodynamically compatible with volatile products of concrete decomposition; carbon dioxide and water liberated from the concrete will oxidize zirconium, chromium, manganese, iron, nickel, and metallic fission products in the melt. If there were no reverse reaction, the metallic phases of a core melt would be completely consumed by the oxidation. Disappearance of the metallic phases from the core melt would sharply reduce the rate of melt attack on the concrete.

A reverse reaction, however, does develop if the gaseous products of the metal-gas reaction are not vented nor burned as they emerge from the melt. These reduced gas species will reduce metallic oxidation in the core melt and thus prolong the presence of metallic phases in a core melt, extending the duration of rapid attack on the concrete.

The importance of metallic phases during melt/concrete interactions requires that any process tending to deplete them be understood well and be explicitly included in any computer model of melt/concrete interactions. Also melt/gas chemistry must be well characterized because gas behavior within reactor containment is important during reactor meltdown accidents.

Modelling the melt/gas chemistry is complicated because kinetic and thermodynamic factors are both involved and, while thermodynamics of the system may be considered, kinetic factors are much more difficult to do so because appropriate data are neither available nor obtainable at any practical cost. Therefore melt/gas chemistry must be considered within a thermodynamic framework. However, it would be unwise, even theoretically to treat the melt/concrete system as a thermodynamically balanced system. Lip service, at least, must be paid to the kinetic aspects of the system. The following observations from the ongoing experimental program are pertinent to the formulation of a model:

- Oxides and metals are largely immiscible. Molten materials usually stratify into at least an oxidic and a metallic layer; in some cases, two oxide layers could sandwich the metallic layer. This stratification suggests that the molten materials can realistically be separated into oxidic regions and a metallic region. Thermodynamic equilibrium between the regions will be slowed by the limited interaction across their boundaries.
- Composition of gases emerging from melts are similar regardless of thickness, suggesting that gas-metal interactions are quite rapid and thermodynamic equilibrium between the metals and the gases liberated from the concrete will be quickly attained.
- Metal droplets are often found within the oxide phases of a solidified melt, suggesting that chemical reactions in the oxide phases are kinetically slow as is mass transfer of condensed species within and from the oxide melt.
- The solidified oxide phase is not uniform in color, suggesting that oxide-gas reactions occur predominately at the surface of the oxide melt.

A model to compute thermodynamic equilibria during core meltdown situations has been developed and is described below. The model is to be used as a subroutine in CORCON, a model of melt/concrete interactions. The model and the way it is called out by CORCON will allow the above qualitative observations to be reproduced.

1.2.2.1 Derivation of Model

The primary purpose of the model proposed here is to minimize the free energy of a reacting chemical system subject to the mass balance constraints. The fact that minimum free energy corresponds to chemical equilibrium is a standard result of chemical thermodynamics.³ Every system has a chemical equilibrium and that this equilibrium is unique.^{4 5}

The mathematical statement of the model is

$$\begin{aligned} &\text{Min } G(\vec{N}) \\ &\vec{N} \\ &\text{subject to } [A]\vec{N} = \vec{B}, \end{aligned}$$

where

\vec{N} = vector of species concentrations in the system

G = free energy of the system at a composition expressed by \vec{N}

$[A]$ = Stoichiometry coefficients for elements in the species included in the system

\vec{B} = molar amounts of elements in the system

In addition to the equality constraints defined above, (the so-called "stoichiometry constraints") there are a set of implied "nonnegativity" constraints:

$$N_i \geq 0 \text{ for } \{N_i | N_i \in \vec{N}\}$$

The "nonnegativity" constraints are necessary to insure physically real solutions and constrain the volume of Euclidean space to be searched for the minimum of G . The "nonnegativity" constraints may be removed from specific consideration by the transformation of variables

$$N_i = \exp(\xi_i) \quad \text{for } \{N_i | N_i \in \vec{N}\} .$$

The chemical equilibrium problem then becomes

$$\begin{aligned} & \underset{\vec{\xi}}{\text{Min}} \quad G(\xi) \\ & \text{subject to: } [A] e^{\vec{\xi}} = \vec{B} . \end{aligned}$$

The transformation has at least two undesirable features. Since all adjustments to the composition vector, \vec{N} , are made by multiplying (ie, $N_i^{\text{new}} = \exp(\xi_i^{\text{old}} + \Delta\xi_i) = N_i^{\text{old}} \exp(\Delta\xi_i)$), the phase rule cannot be satisfied without complicated programming. Also, some numerical problems such as "solution trapping" and "overshooting" may arise if initial guesses to a solution are poor.

Solutions to the above constrained minimization problem are made iteratively. Since the solution procedure is to be incorporated in a large computer model, it should contain the following qualities:

- Be reasonably fast
- Use minimal memory
- Not require high quality initial guesses for the start of the minimization procedure
- Assure convergence to an answer

In view of the assumptions in the CORCON model, highly accurate solutions are not required. Solutions must, however, satisfy the stoichiometry constraints to very high accuracy if we are to avoid unrealistic depletion or growth in mass due to numerical errors in repeated calls at each time step to the routine. Also, the use of the subroutine in CORCON requires that chemical equilibrium be computed at constant temperature and pressure.

An examination of the many methods for constrained minimization shows that a modification of the steepest descent method proposed by Van Zeggeren and Storey will meet most of the above requirements.^{6 7 8} Steepest descent methods are not especially fast (linear convergence at best) and are subject to oscillations. These disadvantages are counter-weighted by the modest programming and memory requirements of the methods.

The essential elements of the Van Zeggeren and Storey steepest descent method are outlined below. The development is done algebraically rather than with matrix notation. Let

$$G = \sum_{i=1}^N \mu_i \exp(\xi_i) = \sum_{i=1}^N \mu_i N_i \quad ,$$

where

N = number of species present and

μ_i = chemical potential of the i th species.

Expand G about the point $\{\xi_1, \xi_2, \dots, \xi_N\}$ in a Taylor series to first order:

$$G(N_i^{\text{New}}) = G(N_i^{\text{Old}}) + \sum_{i=1}^N \mu_i N_i \Delta \xi_i \quad .$$

The object of the minimization procedure is to reduce the second term on the right-hand side of the above equation to a minimal value subject to the stoichiometry constraints. However, first-order expansion of G is not especially accurate and would not be suitable for long-range extrapolation of G . The first-order steepest descent method is therefore constrained to proceed toward the minimum in a series of short steps. If a steplength, σ , is defined, another constraint must be introduced:

$$\sum_{i=1}^N (\Delta \xi_i)^2 = \sigma^2 \quad .$$

The steepest descent analysis to this point has assumed that the following stoichiometry constraints are satisfied throughout the problem:

$$\sum_{i=1}^N A_{i,j} N_i = B_j \quad \text{and} \quad j = 1 \text{ to } E \quad ,$$

where

E = the number of elements in the system

B_j = moles of the j th element in the system

$A_{i,j}$ = atoms of the j th element in the i th species in the system.

Typically, the initial guess, from which the iteration procedure begins, may not satisfy these constraints. Even if it does, as iteration proceeds, the truncation error introduced by first-order expansion of G will lead to the solution drifting out of the constrained solution space. To avoid these difficulties let

$$F_j(N) = \sum_{i=1}^N A_{i,j} \exp(\xi_i) .$$

Then expand F_j in a first order Taylor series about $(\xi_1, \xi_2, \dots, \xi_N)$

$$F_j(N^{\text{new}}) = F_j(N^{\text{old}}) + \sum_{i=1}^N A_{i,j} \exp(\xi_i) \Delta \xi_i .$$

Since $F_j(N^{\text{new}})$ is to equal B_j ,

$$B_j - C_j = \sum_{i=1}^N A_{i,j} \exp(\xi_i) \Delta \xi_i \quad \text{and} \quad j = 1 \text{ to } E$$

where

$$C_j = \sum_{i=1}^N A_{i,j} \exp(\xi_i) \quad \text{for} \quad j = 1 \text{ to } E .$$

With the stoichiometry constraints rewritten in this form, the minimization problem can be solved by using the method of Lagrangian undetermined multipliers to find the unknown $\Delta \xi_i$'s ($i = 1$ to N).

The Lagrangian for the system is

$$L = \sum_{i=1}^N \mu_i N_i \Delta \xi_i - \sum_{j=1}^E \pi_j \left(\sum_{i=1}^N A_{i,j} N_i \Delta \xi_i + C_j - B_j \right) - \frac{X}{2} \left(\sum_{i=1}^N (\Delta \xi_i)^2 - \sigma^2 \right),$$

where π_j for $j = 1$ to E and X are undetermined multipliers. Setting the derivative of L with respect to $\Delta \xi_i$ to zero yields

$$\mu_i N_i - \sum_{j=1}^E \pi_j A_{i,j} N_i - X \Delta \xi_i = 0, \quad i = 1 \text{ to } N$$

and

$$\Delta \xi_i = \left(\mu_i N_i - \sum_{j=1}^E \pi_j A_{i,j} N_i \right) / X \quad \text{for } i = 1 \text{ to } N.$$

Multiplying this equation by $A_{i,k} N_i$ and summing over i yields

$$0 = \sum_{i=1}^N \mu_i A_{i,k} N_i^2 - \sum_{j=1}^E \pi_j \sum_{i=1}^N A_{i,k} A_{i,j} N_i^2 - X \sum_{i=1}^N A_{i,k} N_i \Delta \xi_i \quad \text{for } k = 1 \text{ to } E.$$

From the revised stoichiometry constraints,

$$\sum_{i=1}^N A_{i,k} N_i \Delta \xi_i = B_k - C_k \quad \text{for } k = 1 \text{ to } E.$$

Therefore

$$0 = \sum_{i=1}^N \mu_i A_{i,k} N_i^2 - \sum_{j=1}^E \pi_j \sum_{i=1}^N A_{i,k} A_{i,j} N_i^2 - X(B_k - C_k).$$

This set of E equations shows that the Lagrangian multipliers, π_j for $j = 1$ to E, are linearly related to the multiplier X. Let

$$\pi_j = U_j + V_j X \quad \text{for } j = 1 \text{ to } E$$

then

$$\sum_{j=1}^E U_j \sum_{i=1}^N A_{i,k} A_{i,j} N_i^2 = \sum_{i=1}^N \mu_i A_{i,k} N_i^2$$

and

$$\sum_{j=1}^E V_j \sum_{i=1}^N A_{i,k} A_{i,j} N_i^2 = - (B_k - C_k) \quad \text{for } k = 1 \text{ to } E$$

These two sets of linear equations allow the Lagrangian multipliers π_j for $j = 1$ to E to be defined in terms of X. In following this development, the N dimensional minimization problem has been reduced to an E dimensional problem. Since $E \leq N$, some simplification in the minimization has been realized. Note also the coefficients of U_j and V_j for $j = 1$ to E in the above linear equations are identical and would form a symmetric matrix. This simplifies programming the method.

Solution of the linear equations allows the computed corrections to the composition vector to be written as

$$\Delta \xi_i = (D_i - X E_i) / X \quad \text{for } i = 1 \text{ to } N$$

where

$$D_i = \mu_i N_i - \sum_{j=1}^E U_j A_{i,j} N_i$$

and

$$E_i = \sum_{j=1}^E V_j A_{i,j} N_i$$

The multiplier X is defined by the stepsize constraint:

$$\sum_{i=1}^N (\Delta \xi_i)^2 = \sigma^2 = \sum_{i=1}^N \frac{1}{X^2} (D_i - X E_i)^2 .$$

Since

$$\sum_{i=1}^N D_i E_i = 0 ,$$

$$X = - \sqrt{\sum_{i=1}^N D_i^2 / \left(\sigma^2 - \sum_{i=1}^N E_i \right)^2} .$$

The sign for X must always be negative for the procedure to minimize the free energy. Van Zeggeren and Storey suggested the sign be chosen according to which value of X reduced G.^{7 8} However, the derivation of first-order methods demonstrates that the sign must be negative. The procedure used to assure that the "stoichiometry constraints" are satisfied makes it difficult to choose a sign based on reduction of G.

1.2.2.2 Implementation of the Model

As might be expected, implementation of the above procedure involved some computation difficulties. These difficulties arose in two areas:

- As with all iterative solution methods, the procedure requires an initial guess. It was desired that the procedure not be sensitive to the initial guess, that "infeasible" guesses - guesses that do not satisfy the stoichiometry constraints - are to be allowed.
- When an arbitrary step length was chosen and kept constant throughout the iterative process, the estimates of the equilibrium solution oscillated about the true solution. Oscillations were

particularly severe when the minimum of the free energy was located at the bottom of a very deep hyperparabola in the search space. This occurred whenever the amount of one or more elements in the system was very difficult from the amount of other elements in the system.

Convergence of first-order methods is guaranteed. However, the rate of convergence is slow and, in fact, may slow hopelessly in the vicinity of the solution.⁹ When initial guesses that are wildly different from the equilibrium compositions were provided for the above model, an excessive number of iterations were required to recover. To avoid this, a subroutine was added to the model to correct the initial guesses so that the "stoichiometry constraints" were approximately satisfied and to limit the composition of any species to be less than or equal to its upper bound. Also, a lower bound on the initial guess of any species was established so that an excessive number of iterations was not required to correct this guess.

Oscillations in the computed values of the free energy (G/RT), moles of hydrogen (M_{H_2}), and moles of carbon monoxide (M_{CO}) when a constant steplength is used are shown in Figure 1-1. The results in this figure are for the "Blast Furnace Problem" described below. To eliminate the oscillations, the steplength was shortened as the iterative process progressed.

The shortening was done arbitrarily whenever required. Optimal stepsize calculations based on the change in the free energy, such as that suggested by Smith & Missen,¹⁰ could not be implemented because of the way satisfaction of the stoichiometry constraints is forced in the model. The results shown in Figure 1-2 demonstrate the striking improvement produced by the convergence forcing due to shortening the steplength.

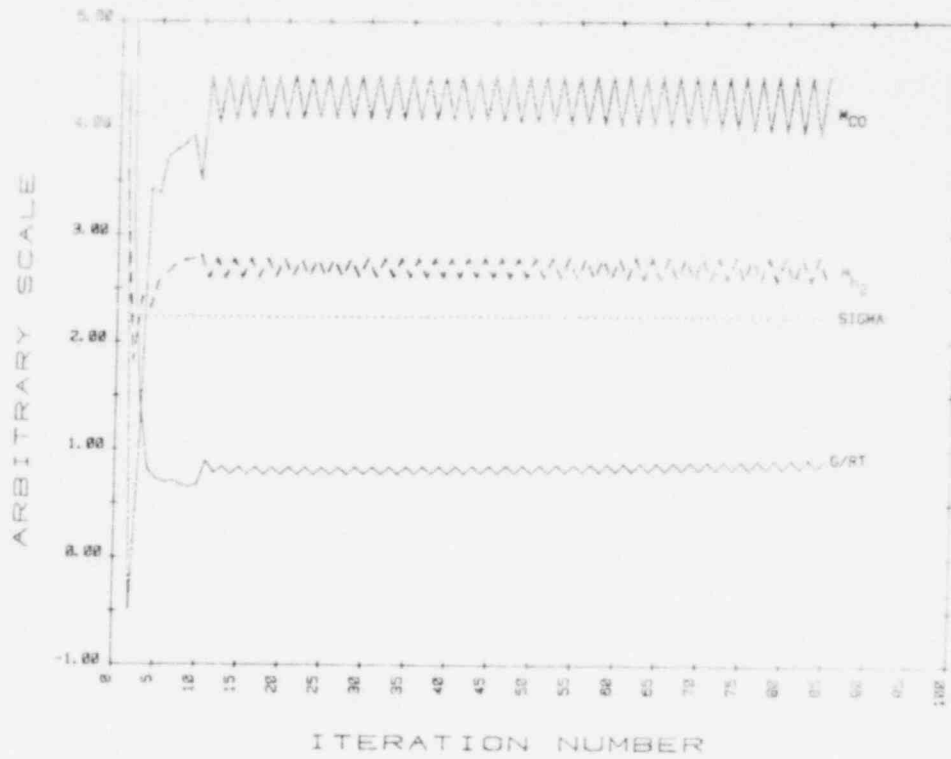


Figure 1-1. Model Results for Blast Furnace Problem Without Convergence Forcing

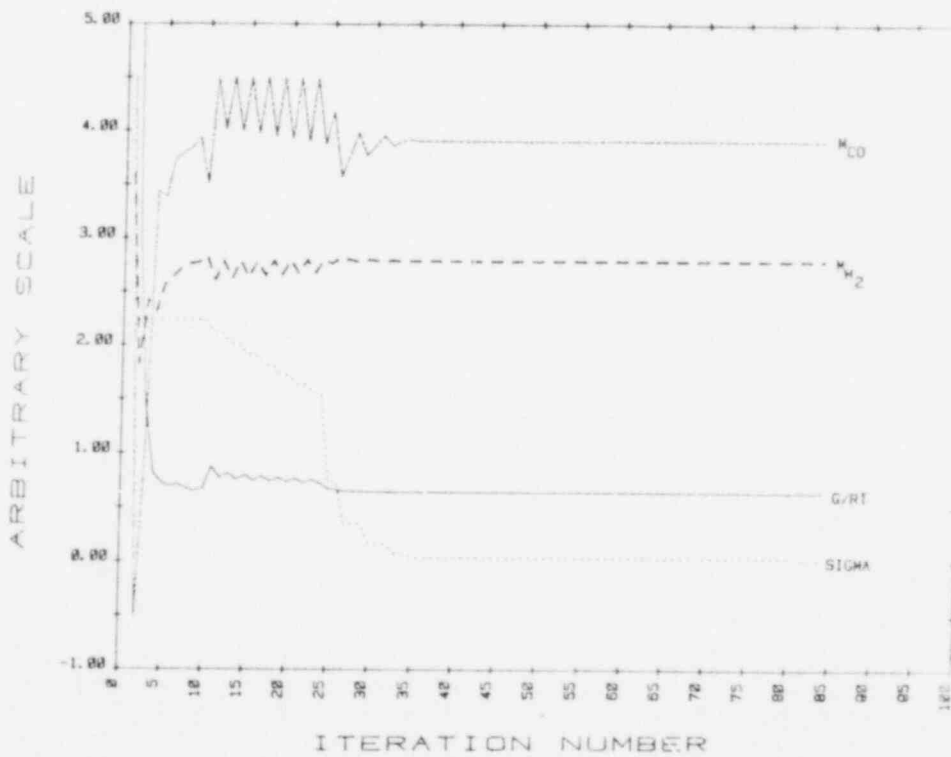


Figure 1-2. Model Results for Furnace Problem With Convergence Forcing

Convergence of the iterative process was defined when

- Change in $G/Rt \leq t$
- $|B_k - C_k| \leq \epsilon B_k$ for $k = 1$ to E

where $t = 0.001$ and $\epsilon = 1 \times 10^{-16}$. Convergence based on the size of X as suggested by Van Zeggeren and Storey yielded unsatisfactory solutions.⁸

1.2.2.3 Testing the Model

The performance of the model was tested by computing two problems for which results obtained by other methods were available:

- Pyrolysis of propane at 2200 K at 40 atmospheres in varying amounts of air⁷
- The so-called Blast Furnace Problem - carbonothermic reduction of iron oxides in the presence of limestone at 1050 K and 1 atm^{11 12}

The latter of these test problems is especially interesting since much of the chemistry is similar to that encountered in melt/concrete interactions.

Results produced by the model for the pyrolysis of propane are compared to published results in Table 1-I. The ratio of air to propane (R) was varied over the range of $R = 1$ to $R = 5$. The compositions listed in Table 1-I are in units of mole fraction based on the gas phase. The comparison of results shows that the model solutions and the published solutions agree to not worse than 1 part in 1000.

Two solutions to the Blast Furnace Problem are available. The first, published by Madeley and Toguri, was obtained by a first-order steepest descent technique similar to that outlined above.¹¹ The second solution, published by Smith,¹² was obtained by an equilibrium constant method similar to that proposed many years ago by Brinkley¹³. The Smith solution has a lower free energy than that of Madeley and Toguri and must therefore be the better estimate of the equilibrium composition.

Table 1-I

Comparison of Results From the Model With Literature Results for the Pyrolysis of Propane in Varying Amounts of Air ($C_3H_8 + R(O_2 + 4N_2)$ Products)

Products	R = 1		R = 2		R = 3		R = 4		R = 5	
	Lit.*	Model ⁺	Lit.*	Model ⁺	Lit.*	Model ⁺	Lit.*	Model ⁺	Lit.*	Model ⁺
CO ₂	0.00002	0.00002	0.00989	0.00987	0.03404	0.03399	0.06891	0.06868	0.10795	0.10795
N ₂	0.39996	0.39997	0.53322	0.53320	0.63147	0.63141	0.69554	0.69549	0.73874	0.73874
H ₂ O	0.00018	0.00018	0.05675	0.05671	0.12376	0.12370	0.14830	0.14827	0.14673	0.14674
CO	0.19976	0.19977	0.19006	0.19007	0.12383	0.12386	0.06151	0.06155	0.00294	0.00293
H ₂	0.39953	0.39951	0.20966	0.20967	0.08657	0.08660	0.02546	0.02547	0.00077	0.00077
H	0.00056	0.00055	0.00041	0.00041	0.00026	0.00027	0.00014	0.00015	0.00002	0.00003
OH	0.00000	0.00000	0.00002	0.00003	0.00005	0.00006	0.00012	0.00012	0.00068	0.00065
O	0.00000	0.00000	0.00000	0.00001	0.00000	0.00002	0.00000	0.00001	0.00001	0.00002
NO	0.00000	0.00000	0.00000	0.00001	0.00001	0.00004	0.00003	0.00005	0.00097	0.00097
O ₂	0.00000	0.00000	0.00000	0.00000	0.00000	0.00002	0.00000	0.00002	0.00119	0.00119
NO ₂	0.00000	0.00000	0.00000	0.00000	0.00000	0.00001	0.00000	0.00000	0.00000	0.00000
C	0.10020	0.10019	0.00000	0.00001	0.00000	0.00001	0.00000	0.00000	0.00000	0.00000

*Literature solutions taken from Reference 7.

⁺All solutions provided by the model satisfied stoichiometry constraints based on the elements to 1 part in 10⁸ at worst.

Comparison of the solution obtained by the model described here and the published solutions is made in Table I-II. The model produces a solution that agrees quite closely with that of Smith. Substantial deviations occur only for trace species. If convergence forcing is not used in the model, one of the resulting oscillation points is the Madeley and Toguri solution. It would appear that any convergence forcing used in the Madely and Toguri steepest descent method was not adequate to allow convergence.

Table I-II

Comparison of Results of Model With Results Published by Others for the Blast Furnace Problem

Species	Model*	Madeley & Toguri**	Smith ⁺
O ₂	0.00007	0.0004508	0.173 x 10 ⁻¹⁸
N ₂	187.10000	187.100	187.100
H ₂ O	0.44259	6.873	0.444
CH ₄	0.00680	0.001362	0.00655
CO	81.60342	78.75	81.62
CO ₂	6.66599	4.871	6.66
H ₂	6.43024	0.001584	6.43
CHO	0.00036	0.0008584	0.00000105
CH ₂ O	0.00041	0.004594	0.00000236
OH	0.00017	0.0006745	0.793 x 10 ⁻¹⁰
Fe ₃ O ₄	0.00024	0.001979	0
"FeO"	0.00113	0.009097	0
Fe	42.82514	42.81	42.87
C	0.00815	4.661	0
CaCO ₃	0.00142	0.0002633	0
CaO	0.75458	0.7559	0.756

*The model yielded results satisfying stoichiometric constraints to 1 part in 10⁷ at worst

**W. D. Madeley and J. M. Toguri, Ind. Eng. Chem. Fund. 12, 261(1973).

⁺W. R. Smith, Ind. Eng. Chem. Fund. 15, 227(1976).

The effect of initial guess on the solution produced by the model was investigated with the Blast Furnace Problem. The results for three different initial guesses are shown in Table I-III. Though initial guesses may influence the number of iterations, it is apparent that the guesses have only modest impact on the final solution.

The following conclusions were obtained from testing the model:

- The model is suitable for obtaining the equilibrium composition of a reactive, multiphase mixture to an accuracy suitable for the computer model CORCON.
- The solutions provided by the model do not satisfy the phase rule. Because the model uses multiplicative corrections, no species may be eliminated completely from the final mixture.
- The model compares favorably with other methods of calculating equilibrium compositions, especially with regard to major constituents of the final equilibrium mixture. The accuracy of model predictions for species of low concentration in the equilibrium mixture is poor.
- An initial guess of unity for each species in a system analyzed by the model is satisfactory. More educated guesses speed operation of the model.

1.2.2.4 Status of Model

The chemical equilibrium model will be used in CORCON to estimate the extent of reaction of CO_2 and H_2O with metal phases of a core melt and to estimate reaction of reduced containment gases with oxide phases of a core melt. It will also compute heat of reaction, density of the equilibrium gas phase, and heat capacity of the gas phase. It will not initially, but may in the future, be used to evaluate chemical equilibria in the gas phase within the reactor containment.

Table 1-III

Effect of Initial Guess on the Solution Obtained for the Blast Furnace Problem

Species	Initial Guess	Solution	Initial Guess	Solution	Initial Guess	Solution
O ₂	0.00451	7 x 10 ⁻⁵	1.0	7 x 10 ⁻⁵	1.0	8 x 10 ⁻¹²
N ₂	187.1	187.1	1.0	187.1	20.0	187.10
H ₂ O	6.873	0.44324	1.0	0.44259	1.0	0.4426
CH ₄	0.00136	0.00686	1.0	0.00680	0.01	0.0069
CO	78.75	81.60312	1.0	81.60342	10.0	81.602
CO ₂	4.871	6.66570	1.0	6.66599	10.0	6.66599
H ₂	0.00158	6.42944	1.0	6.43024	0.001	6.42986
CHO	0.00086	0.00038	1.0	0.00036	0.001	0.00040
CH ₂ O	0.00459	0.00043	1.0	0.00041	1.0	0.00040
OH	0.00675	0.00017	1.0	0.00016	0.001	0.00016
Fe ₃ O ₄	0.00198	0.00025	1.0	0.00024	10.0	0.00024
"FeO"	0.00910	0.00119	1.0	0.00113	1.0	0.00134
Fe	42.81	42.82505	1.0	42.82514	2.0	42.8249
C	4.661	0.00861	1.0	0.00815	100.0	0.0087
CaCO ₃	0.00026	0.00147	1.0	0.00142	1.0	0.00160
CaO	0.7559	0.75453	1.0	0.75458	1.0	0.75438
No. of Iterations		95	84		62	
G/RT		-2501.38	-2501.38		-2501.38	
MAX $\frac{B_i^*}{B_i}$		19.5 x 10 ⁻⁸	4.43 x 10 ⁻⁸		5.36 x 10 ⁻⁸	

*Maximum of $C_j - B_j / B_j$ for $j = 1$ to E

The species to be considered in the model when called by CORCON are listed in Table 1-IV. Species that do not react appreciably under core meltdown accident conditions - mostly refractory oxides - are to be treated as inerts made up exclusively of an element X. Consequently, calls to the model by CORCON will entail solution of an 11-element, 34-species problem. Speed of the routine will be of great importance. Substantial testing of the model to optimize its performance for meltdown problems remains to be done. These performance tests will also be used to determine if the list of species in Table 1-IV needs to be altered.

Table 1-IV
Chemical Species To Be Considered in
Chemical Equilibria Calculations in CORCON

<u>Gas Species</u>	<u>Oxidic Species</u>	<u>Metallic Species</u>
CO	"FeO"	Fe
CO ₂	Fe ₃ O ₄	Cr
H ₂	Fe ₂ O ₃	Ni
H ₂ O	Cr ₂ O ₃	Zr
H	CrO ₃ (c)	Mn
OH	NiO	Mo
N ₂	ZrO ₂	
O ₂	MnO	
CH ₄	MnO ₂	
C ₂ H ₄	MoO ₂	
C ₂ H ₆	MoO ₃	
CHO	Inert Oxides	
CH ₂ O		
C ₂ H ₂		
O		
CrO ₃ (g)		

The model currently contains no provisions for treating condensed mixture. That is, stainless steel is treated by the model as a mechanical mixture of iron, nickel, chromium, and manganese. Modifications of the

model to treat condensed mixtures are easily done and will be made if performance tests with meltdown problems indicated such a need.

1.3 Molten Core/Concrete Interaction Analytical Program (J. F. Muir)

Development of the improved core/concrete interaction model, CORCON, continued. CORCON is a user-oriented computer program written in a modular structure in which most computational units are contained in separate subroutines. Maximum use is being made of existing codes and subroutines. Phenomenological models are being developed as required with a heavy reliance on existing techniques, and data and correlations available in the literature. Numerous input options provide a flexibility that enables a variety of problems to be solved by merely changing input data. Efforts during the present quarter concentrated on computer programming and phenomenological model development and implementation.

1.3.1 Phenomenological Model Development (F. G. Blottner, J. F. Muir, and D. A. Powers)

A chemical equilibrium model which treats chemical reactions of gases present during core/concrete interactions with constituents of the core melt has been developed by D. A. Powers. The chemical reactions are modelled using a first-order, steepest-descent, free-energy minimization technique. The model provides equilibrium chemical composition, heat of reaction, and gas phase density and heat capacity for each melt/gas system treated. A detailed description of the model along with the results of sample problem calculations are presented in Section 1.2.2.

A study of the hydrodynamics and heat transfer characteristics of liquid pools with bubble agitation has been performed by F. G. Blottner. Previous simulant experiments and correlations are used to define hydrodynamics and heat transfer models suitable for describing phenomena occurring when a pool of molten core materials interacts with concrete. Presented in the following paragraphs is a brief summary of results obtained for gas bubble size, bubble velocity, local void fraction, average layer void fraction and level swell, and convective heat transfer from the interior of a pool to its periphery (i.e., the pool interface

region boundary), and across liquid/liquid interfaces, in a pool with gas-driven circulation. Details of the analysis and supporting data are presented in a report on the study that is currently in preparation.¹⁴

Hydrodynamic studies of gases bubbling through liquids, produced by either boiling of the liquid or controlled gas injection, indicate that the velocity of the gas as it enters the liquid has a significant influence on the type of bubble flow that occurs. Flow regimes observed for air bubbling through water are listed in Table 1-V.

Table 1-V
Flow Regimes and Gas Velocities for Air Bubbling
Through Water

Flow Regime	Superficial Gas Velocity (m/s)
I Nucleate or laminar bubbling	$V_s < (V_s)_{LB} \sim 0.06$
II Patchy or foam bubbling	$V_s \sim 0.06$ to 0.76
III Blanketed or film bubbling	$V_s > (V_s)_{FILM} \sim 0.76$

Expressions for the critical values of the superficial velocity in terms of liquid and gas properties are

$$(V_s)_{LB} = 0.38 \sqrt{\frac{\sigma}{\rho_l A}} \quad (1.1)$$

$$(V_s)_{FILM} = k_s \sqrt{\frac{\sigma}{\rho_l A}} \quad (1.2)$$

where

$$k_s = \begin{cases} 30 M_*^{2/3} & \text{for } Ar_* > 10^4 \\ 6.3 M_*^{2/3} Ar_*^{1/6} & \text{for } Ar_* < 10^4 \end{cases}$$

and

$$M_* = \left[\frac{g \rho_g A}{\rho} \right]^{1/2}$$

$$Ar_* = \frac{g A^3}{\nu_l^2}$$

$$A = \left[\frac{\sigma}{g(\rho_l - \rho_g)} \right]^{1/2} \quad - \text{ Laplace constant.}$$

Equation (1.1) is given by Wallis for the maximum superficial velocity for laminar bubbly flow.¹⁵ Equation (1.2) is given by Kutateladze for the minimum superficial velocity required to have stable gas film bubbling.¹⁶ Order of magnitude values for these parameters for the liquids of interest are presented in Table 1-VI. These calculations were made by using average property values for typical LWR oxidic and metallic melts, molten concrete (slag) characteristic of the three representative LWR concretes included in CORCON, water, and the associated gas mixtures.

Table 1-VI
Critical Velocities
(m/s)

Liquid	$(V_s)_{LB}$	$M_* \times 10^4$	Ar_*	k_s	$(V_s)_{FILM}$
Water	0.062	5.63	1.99×10^5	0.204	0.96
Oxidic	0.060	2.22	5.06×10^5	0.110	3.26
Metallic	0.085	3.16	2.75×10^6	0.139	5.30
Slag	0.070	2.60	2.63	0.030	0.62

The size of bubbles generated in the three flow regimes described in Table 1-V is based on expressions for the equivalent spherical radius of bubbles in the nucleate and film bubbling regimes; these expressions are listed in Table 1-VII.

Table 1-VII

Equivalent Spherical Radius of Bubbles

Flow Regime	Bubble Radius (m)	
Nucleate bubbling	$(R_e)_I = 0.0105 \beta A, \beta = 45^\circ$	(1.3)
Film bubbling	$(R_e)_{III} = 3.97A$	(1.4)
Patchy bubbling	$(R_e)_{II} = \text{linear interpolation -}$ Eqs (1.3) and (1.4)	

A schematic representation of the resulting variation in bubble size with superficial gas velocity is given in Figure 1-3. Characteristic values of bubble radius given by Eqs (1.3) and (1.4) for the liquids of interest are presented in Table 1-VIII.

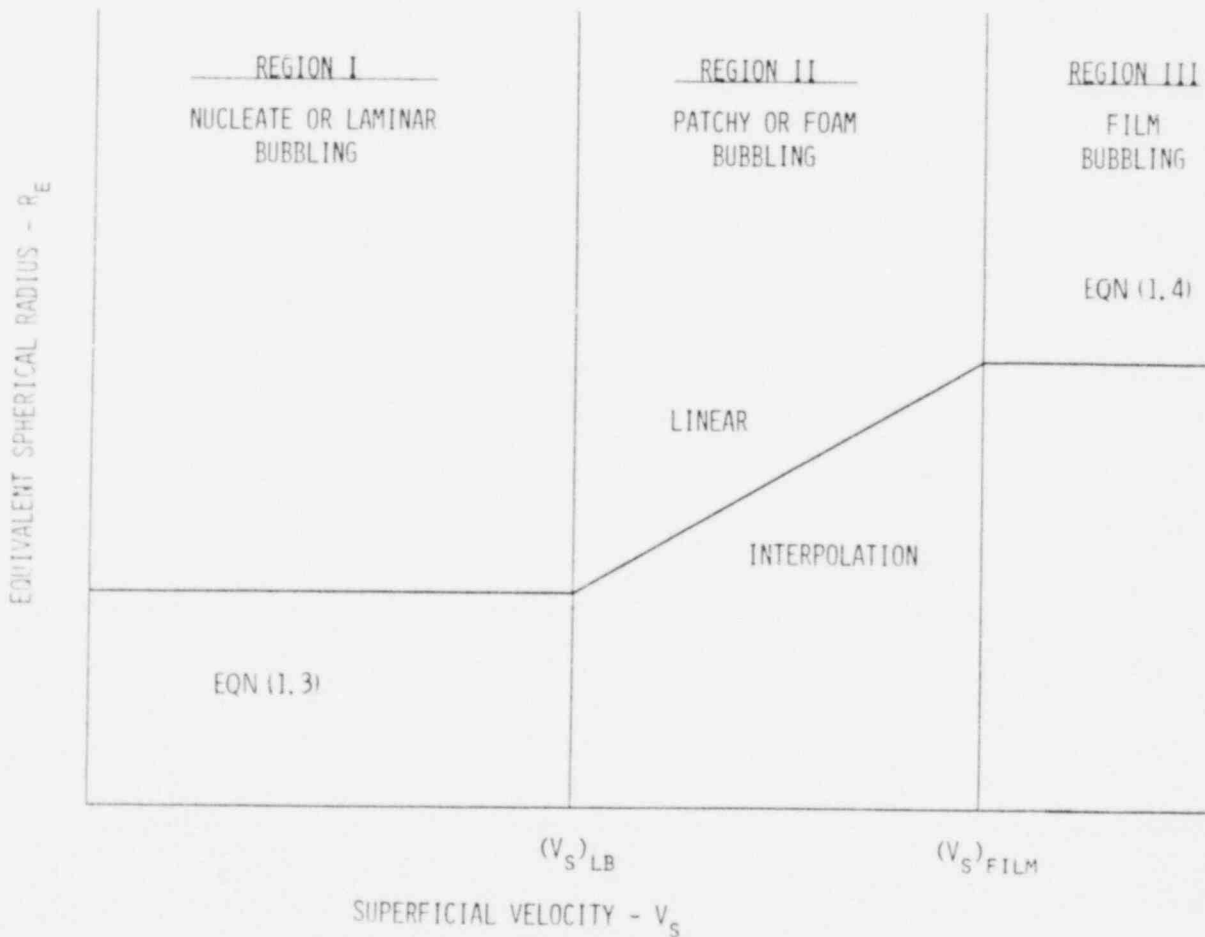


Figure 1-3. Bubble Size as a Function of Superficial Gas Velocity

Table 1-VIII
Bubble Properties

<u>Liquid</u>	<u>(R_e)_I (cm)</u>	<u>(R_e)_{III} (cm)</u>
Water	0.13	1.08
Oxidic	0.12	1.02
Metallic	0.24	2.05
Slag	0.16	1.39

An estimation of the flow regime and associated bubble size that might occur during melt/concrete interaction may be obtained from estimates of the superficial velocity of gaseous decomposition products emanating from the surface of ablating concrete. For a typical surface erosion rate of approximately 10^{-4} m/s (36 cm/hr), superficial velocities for the representative basaltic aggregate, limestone aggregate, and CRBR limestone concretes were found to be 0.10, 0.25, and 0.34 /s, respectively. Comparing these with the critical superficial velocities given in Table 1-VI suggests that the patchy or foam flow regime would exist during melt/concrete interactions with bubble sizes on the order of a centimeter in diameter. An order of magnitude smaller erosion rate would result in nucleate or laminar bubbling. However, for film bubbling to occur for the oxidic and metallic mixtures, a significantly larger increase in concrete erosion rate would be required.

These predictions are in keeping with results obtained by Powers^{17 18} for the test BURN 1. In this test an x-ray image intensification system was used to monitor the behavior of a thermitically generated steel melt in contact with limestone aggregate concrete. Melt temperature was uncontrolled in this test and varied between 2600° and 1550°C. Gas flow rates varied between 300 and 30 L/min. Conversion of the flow measurements yields superficial gas velocities of 1.44 to 0.09 m/s. At the highest superficial velocities, the thin melt was so badly agitated and dispersed that characterization of the operative flow regime would be ambiguous. At the lower superficial velocities, the melt flow could be characterized as laminar bubbling or transitional flow. Bubble sizes

observed during the test and voids frozen in the solidified melt varied between 0.3 and 2.4 cm in diameter.

The velocity of gas bubbles passing through a liquid is commonly related to the terminal velocity of a single bubble rising through the liquid. The latter is usually expressed as a function of bubble size and material properties. Thus, for small bubbles characterized by Stoke's flow, the terminal velocity is given by

$$U_{T_1} = \frac{2}{9} \frac{gR_e^2}{\nu_1} \quad (1.5)$$

For medium-sized bubbles rising through low viscosity liquids, the terminal velocity tends to be independent of bubble size and is expressed as

$$U_{T_2} = 1.53 \sqrt{gA} \quad (1.6)$$

Finally, the terminal velocity of large spherical-cap bubbles is given by the relation

$$U_{T_3} = \sqrt{gR_e} \quad (1.7)$$

Equations (1.5) through (1.7) are compared in Figure 1-4 with the terminal velocity data for single bubbles rising through several liquids. Clearly the viscosity of the liquid has a significant effect on the terminal velocity variation with bubble size.

The procedure employed in CORCON for determining bubble terminal velocities is based on a critical value of the equivalent radius,

$$R_{e_c} = 2.34 A \quad (1.8)$$

determined by equating the terminal velocities given by Eqs (1.6) and (1.7), i.e., $U_{T_2} = U_{T_3}$. Terminal velocities in the two regions separated by R_{e_c} are determined as follows:

When $Re \leq Re_c$,

$$U_T = \text{smaller of } U_{T1} \text{ and } U_{T2}; \quad (1.9)$$

when $Re > Re_c$,

$$U_T = \text{smaller of } U_{T1} \text{ and } U_{T3}.$$

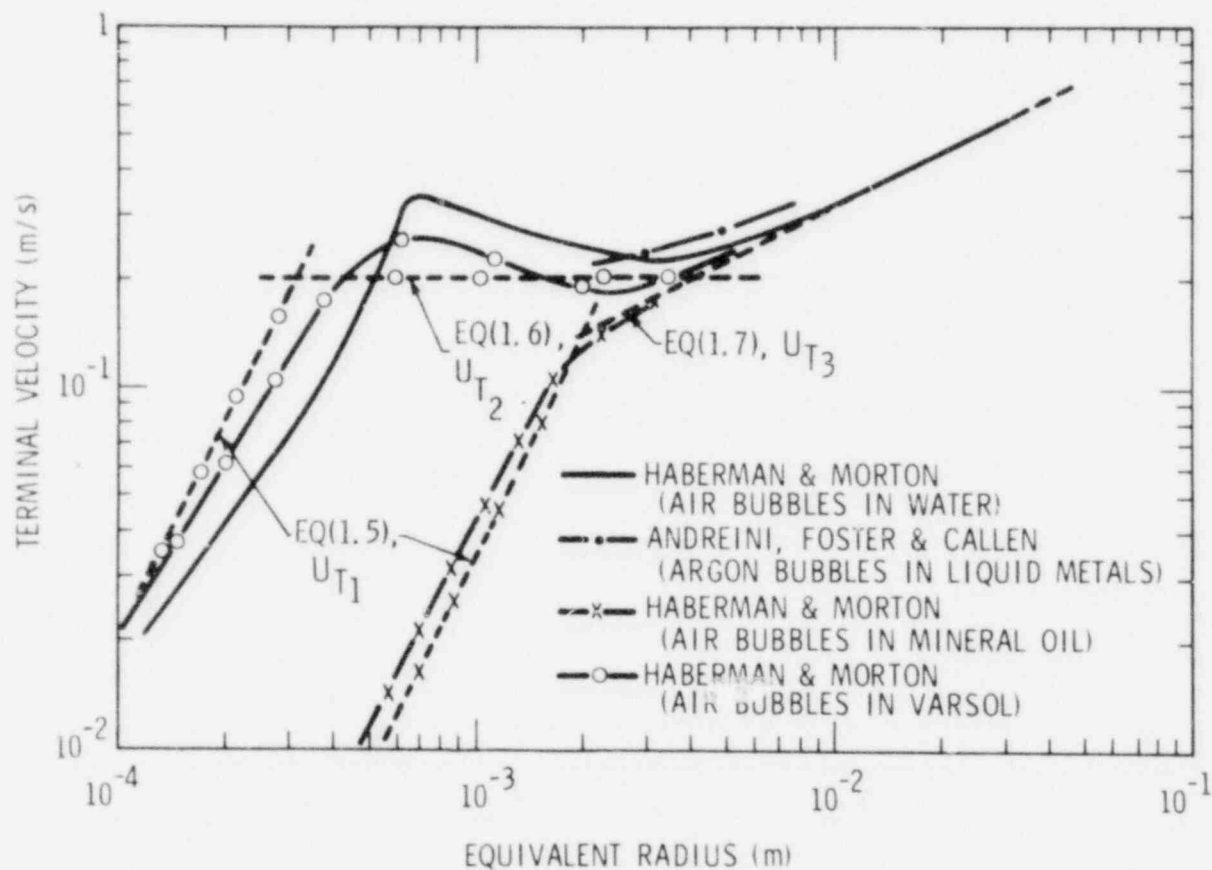


Figure 1-4. Terminal Velocity Variations for Single Bubbles Rising Through Several Liquids

In a multilayered pool of molten core materials interacting with concrete, the depth of each layer, as well as the overall height of the pool, is increased as a result of the concrete decomposition gases bubbling up through the pool. These changes in layer and pool height can be determined if the volume, or void fraction, of gas in the pool is known. The void fraction is defined as

$$\alpha = \frac{\text{volume of gas}}{\text{total volume of gas and liquid}} \quad (1.10)$$

It can also be shown that the local void fraction at any vertical location z is

$$\alpha(z) = \frac{\text{area of gas phase}}{\text{total crosssectional area of gas and liquid}} \quad (1.11)$$

Thus, the upward gas flow in a liquid pool across an area, A , perpendicular to the pool centerline at vertical location z is

$$\dot{m}_g = \rho_g u_g A_g = \rho_g u_g \alpha A \quad (1.12)$$

From continuity, this is equal to all the gas that entered the pool through its outer surface, A_s , up to the vertical location, Z (Figure 1-5):

$$\dot{m}_{g_s} = \rho_{g_s} V_s A_s = \dot{m}_g \quad (1.13)$$

where V_s = superficial velocity of gas entering pool across A_s . As mentioned above, it has been found that the local gas velocity can be related to the terminal velocity of a single bubble with the expression:

$$u_g = (1 - \alpha)^{n-1} U_T \quad (1.14)$$

where

$n = 2$ for ideal bubbly flow, and

$n = 0$ for churn-turbulent bubbly flow.¹⁵

Thus, for churn-turbulent bubbly flow,

$$u_g = \frac{1}{1 - \alpha} U_T \quad (1.15)$$

and

$$\dot{m}_g = \rho_g U_T A \left(\frac{\alpha}{1 - \alpha} \right) \quad (1.16)$$

Solving for α yields:

$$\alpha = \frac{\beta}{1 + \beta} \quad (1.17)$$

where

$$\beta = \frac{m_{g_s}}{\rho_g U_T A}$$

Assuming, for illustrative purposes, that $\rho_g = \rho_{g_s}$, $A_s = A$ (ie, a cylindrical pool with gas injected only through its flat bottom), and with U_T calculated with Eq (1.6), the void fraction has been determined, for representative oxidic and metallic melts as a function of superficial gas velocity. The results for both ideal bubbly and chur-turbulent bubbly flows are presented in Figure 1-6 along with a possible upper limit of $\alpha = 0.42$ based on the occurrence of gas columns or jets through the pool having a separation distance equal to the wave length predicted with the Taylor instability gas film model ($\lambda = 2\pi\sqrt{3} A$).^{19 20}

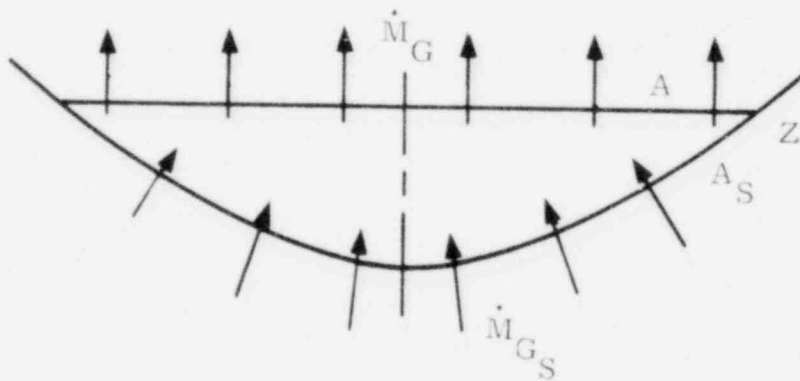


Figure 1-5. Upward Gas Flow

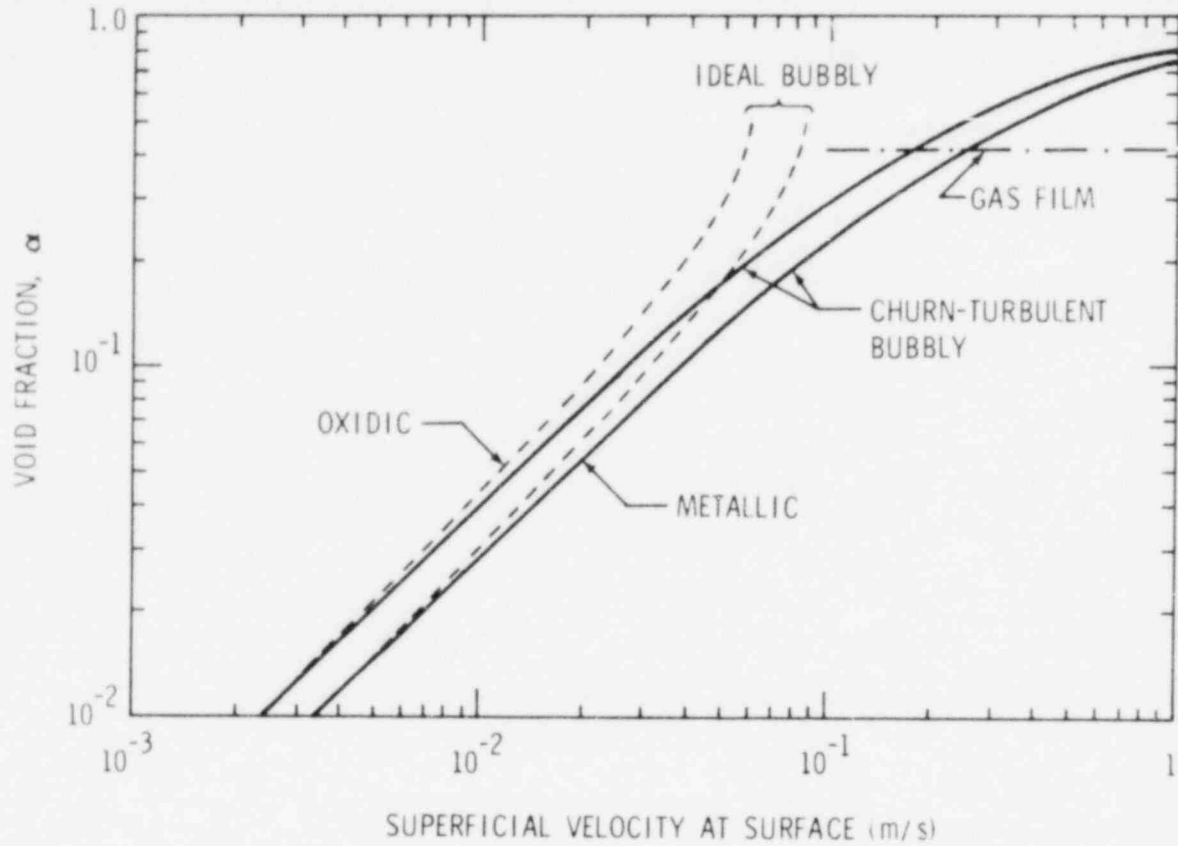


Figure 1-6. Example Void Fraction Variations for Representative Oxidic and Metallic Melts

From the local void fraction definition given in Eq (1.11), the following expression is obtained for the volume of liquid, V_e , contained in any pool layer extending from z_{BOT} to z_{TOP} :

$$\int_{z_{BOT}}^{z_{TOP}} (1 - \alpha) A dz = (V_L)_L \quad (1.18)$$

The value of $(V_L)_L$ for each layer is known at every time step, as are the axial variations in total pool (cavity) cross-sectional area, A , and gas mass flow into the pool, \dot{m}_{g_s} . Thus, by employing Eq (1.17) and assuming the product $(\rho_g U_T)$ is constant across each layer, Eq. (1.18) can be solved, beginning with the bottom layer (where z_{BOT} is known) and working up, to find the layer interface locations and pool surface height with the gas present (ie, the level swell).

Once this is done, an average void fraction for each layer can be determined from

$$\bar{\alpha}_L = 1 - \left(\frac{V_g}{V_L} \right) \quad (1.19)$$

where V_L is the total cavity volume occupied by the layer (ie, between z_{BOT} and z_{TOP}).

Finally, and perhaps most important, are the models developed for describing the convective heat transfer from the interior of the pool to its periphery and across pool layer interfaces. Due to vigorous circulation of the melt by the gases passing through it, the temperature of each pool layer is considered constant everywhere except near the layer boundaries where the temperature varies to its boundary value across a relatively thin thermal boundary layer, δ_t . A schematic of the molten pool-concrete cavity configuration showing the heat transfer regions of interest is given in Figure 1-7.

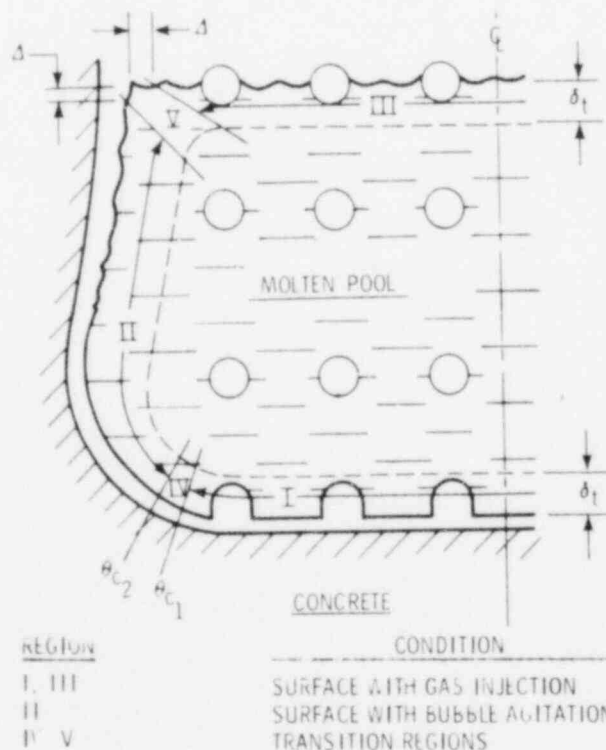


Figure 1-7. Molten Pool-Concrete Cavity Configuration With Pool Interior-to-Boundary Heat Transfer Regions

Although the effects of bubble agitation and injection on the heat transfer are the main concern, models were developed which faired into existing natural convection heat transfer correlations in the limit as the injected gas flow approaches zero. For this purpose, it was considered reasonable to utilize turbulent natural convection relations of the general form:

$$Nu_T = C Pr^{1/3} Ra^{1/3} .$$

The specific relations employed are as follows:

- For vertical or horizontal heated surfaces (regions II and III):

$$h = 0.14 k Pr^{1/3} \left[\frac{g\beta\Delta T}{\nu^2} \right]^{1/3} . \quad (1.20)$$

- For a cooled horizontal surface (region I):

$$h = 0.067 k Pr^{1/3} \left[\frac{g\beta\Delta T}{\nu^2} \right]^{1/3} \quad (1.21)$$

where all properties are liquid properties.

For the various liquids of interest, a lower bound value of the Rayleigh number, Ra, for the conditions existing in a melt/concrete interaction may be estimated by assuming a ΔT of 100 K and a characteristic length, L, of 0.1 m. The resulting values are presented in Table 1-IX along with the corresponding natural convection heat transfer coefficients computed with Eq (1.20) and (1.21). Note that the assumption of turbulent natural convection ($Ra \geq 10^7$) is reasonable for all but the slag, and even in this case the error introduced by using turbulent rather than laminar values is not prohibitively large for the present application.

Table 1-IX

Natural Convective Heat Transfer ($\Delta T = 100 \text{ K}$)

Liquid	Ra_{MIN}	h (vertical or heated horizontal wall)	h (cooled horizontal wall)
Water	1.23×10^9	9.00×10^2	4.3×10^2
Oxidic	2.18×10^8	2.78×10^3	1.3×10^3
Metallic	8.94×10^6	1.16×10^4	5.6×10^3
Slag	1.96×10^4	4.91×10^1	2.3×10^1

The effects of the gas flow through the pool on heat transfer fall into two categories:

- The effect for surfaces through which there is no gas flow, but enhanced heat transfer due to the increased circulation (gas driven) within the liquid
- The effect for surfaces having direct gas injection with a resulting local enhancement of the heat transfer

The combined turbulent natural convection/gas driven convection heat transfer correlations for the regions of interest are as follows:

- For surfaces with bubble agitation (region II), with the gas driven contribution based on a correlation developed by Konsetov²¹ combined with the natural convection relation given in Eq (1.20):

$$h = k \left(Pr \frac{g}{\nu^2} \right)^{1/3} [0.00274 \beta \Delta T + 0.05\alpha]^{1/3} \quad (1.22)$$

- For surfaces with direct gas injection (region I), with the gas driven contribution based on a correlation developed by Grief²⁴ combined with the natural convection relation of Eq (1.21):

$$h = k \left(Pr g/\nu^2 \right)^{1/3} [0.000301 \beta \Delta T + 0.4\alpha^2]^{1/3} \quad (1.23)$$

where, for the latter,

$$\alpha = \frac{b}{1 + b}$$

$$b = \frac{0.65 V_s}{\sqrt{gA}}$$

The heat transfer coefficients predicted by Eqs (1.22) and (1.23) are presented for the liquids of interest in Figures 1-8 and 1-9 are compared with results obtained using other correlations available in the literature.

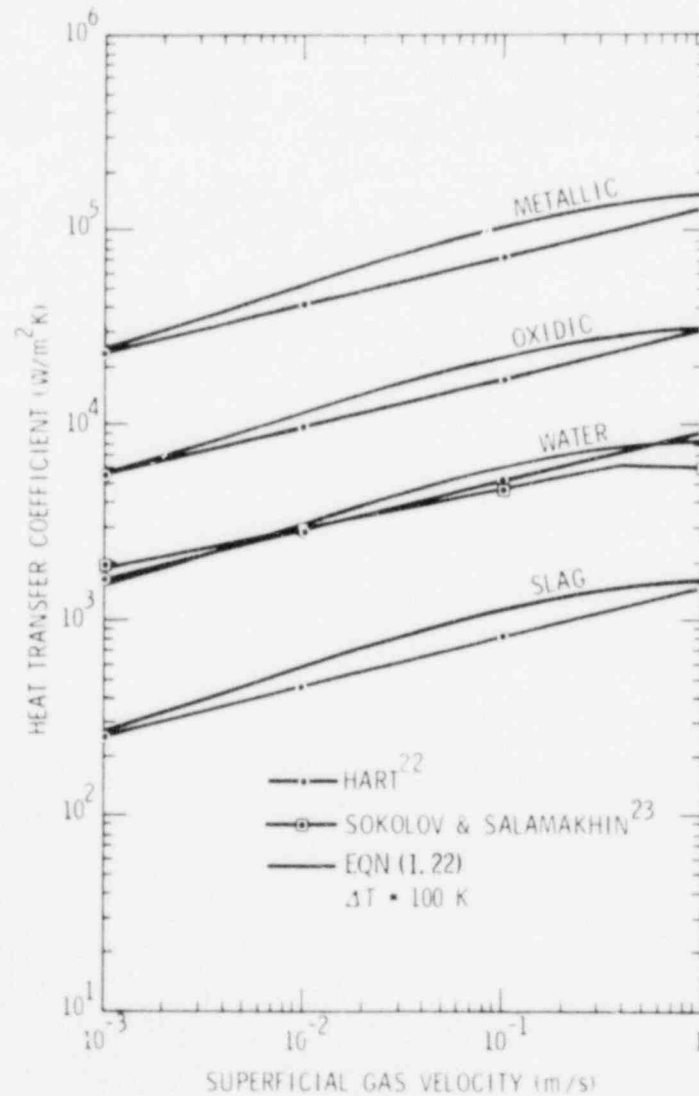


Figure 1-8. Heat Transfer for Surfaces With Bubble Agitation

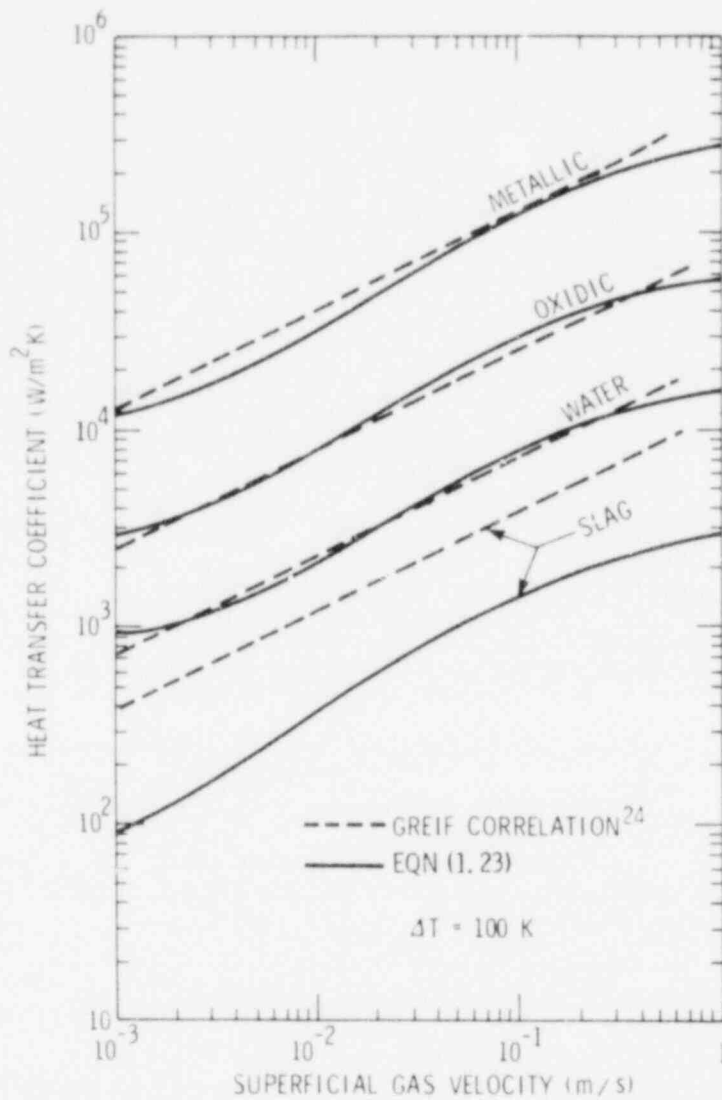


Figure 1-9. Heat Transfer for Surfaces With Gas Injection

The convective heat transfer across layer interfaces (liquid/liquid interfaces) through which gas is bubbling (region III) is modelled in terms of heat transfer coefficients for the upper and lower layers defined, respectively, as

$$h_U = \frac{q_I}{(T_U - T_I)}$$

(1.24)

$$h_L = \frac{q_I}{(T_I - T_L)},$$

where

T_u and T_L = the bulk temperatures of the upper and lower layers, respectively;

q_I = the heat flux across the interfaces; and
the interface temperature is

$$T_I = \frac{h_L T_L + h_U T_u}{h_L + h_U} \quad (1.25)$$

The combined or overall heat transfer coefficient across the interface is

$$h = \frac{q_I}{(T_u - T_L)} = \frac{h_U h_L}{h_U + h_L} \quad (1.26)$$

The resulting combined turbulent natural convection/gas driven convection heat transfer correlation is based on the natural convection relation given in Eq (1.20) and the Konsetov correlation modified to account for interface dynamics:

$$h_{u,L} = k \left(Pr g/\nu^2 \right)^{1/3} \left[0.00274 \beta \Delta T + 50 \alpha^2 \right]^{1/3} \quad (1.27)$$

Overall heat transfer coefficients predicted by Eqs (1.26) and (1.27) combined, with natural convection neglected, for a slag-metal interface and an oil-water interface are presented in Figures 1-10 and 1-11, respectively (dashed curve). Also included for comparison purposes are a limited number of experimental data, the results obtained using other available correlations, and the appropriate natural convection values. Although the general trends and magnitudes are of the proper order, the prediction methods are limited and additional experimental data are needed to verify or improve the correlations.

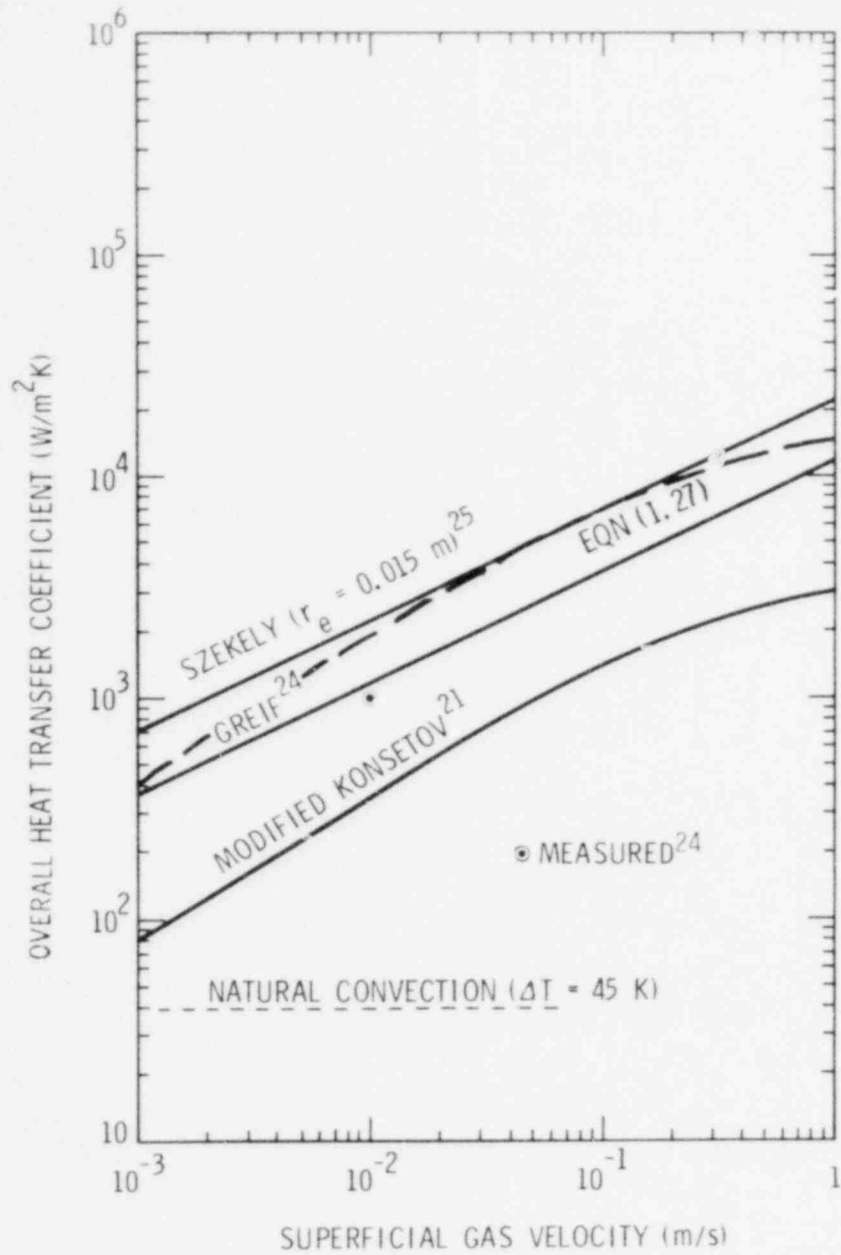


Figure 1-10. Liquid/Liquid Interface Heat Transfer With Gas Bubbling - Slag-Metal

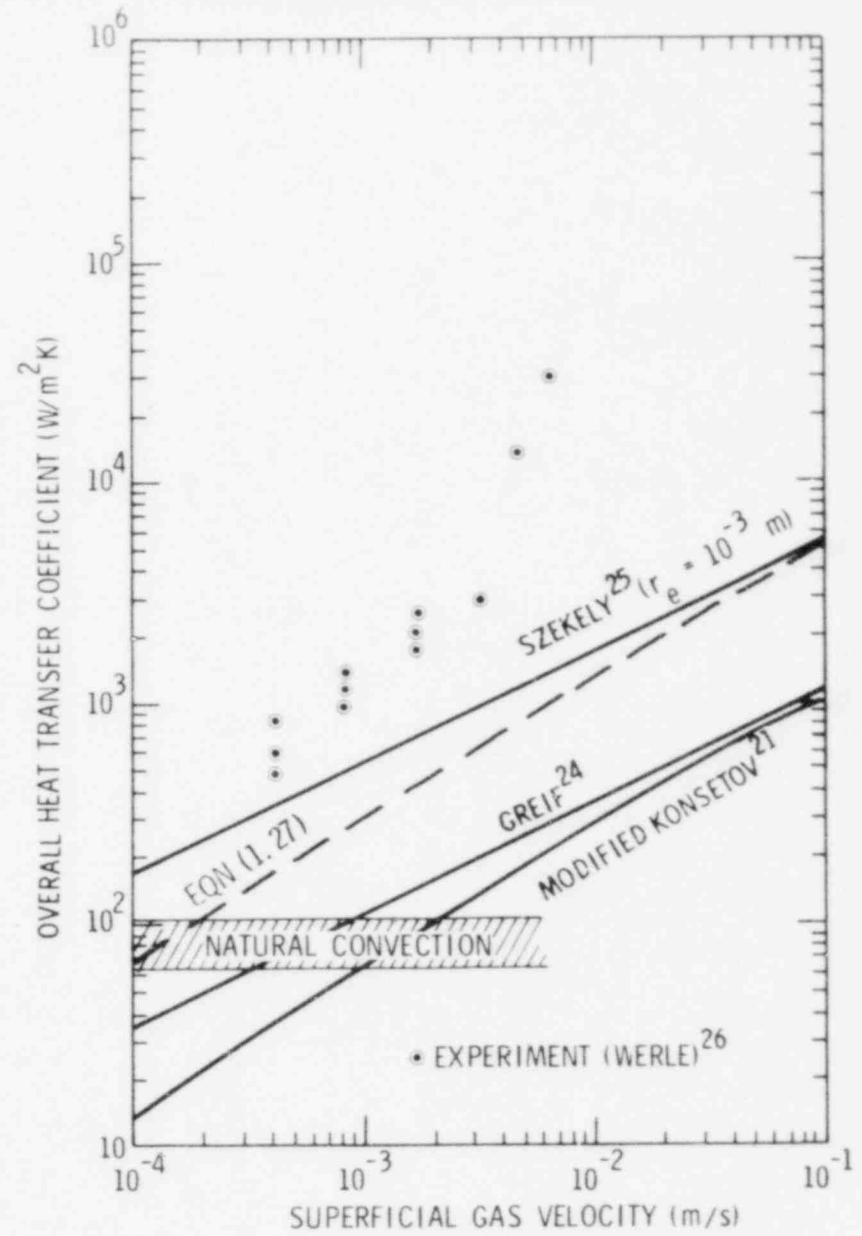


Figure 1-11. Liquid/Liquid Interface Heat Transfer With Gas Bubbling - Oil-Water

1.3.2 Programming and Numerical Concerns (L. S. Dike, M. A. Ellis, J. F. Muir, and W. R. Trebilcock)

Programming efforts during the quarter were devoted to a number of activities. Incorporation of the Concrete Ablation and Shape Change (CASC) program developed by ACUREX Corporation into CORCON was completed. After inserting CASC as a single unit, it was broken up and restructured to fit into the CORCON computation sequence. The resulting version of CORCON was then successfully checked out on a sample problem supplied with CASC.

Procedures were developed and implemented for handling three melt layers plus a coolant layer. Separate subroutines for determining layer orientation within the molten pool; layer geometries (ie, layer volumes and depths, and layer interface and pool surface locations, within the cavity); pressure as a function of vertical distance from the pool surface; and layer properties at each point on the pool periphery, from mixture properties to be provided (ie, a property-switching procedure), have been coded, programmed and partially checked out. Unfortunately, these improvements necessitated fairly extensive modification of the logic in the melt-property subroutine, a routine for handling the properties of the metallic and oxidic mixtures within the melt, to properly account for layer formation, switching and combining (eg, the combination of two oxidic layers into a single layer). A procedure for computing the total flow (quantity per unit time) of either species, total mass, or energy across the melt/concrete interface was developed. Fluxes of a given parameter (quantity per unit area per unit time) provided at each pool periphery point are integrated numerically over the periphery surface area, beginning at the centerline point of the pool bottom, to yield the total flow into or out of the pool up to each periphery point. Coding of this procedure has been initiated.

The melt/gas chemical equilibrium model described in Section 1.2.2 was translated from the HP language in which it was developed into standard Fortran and brought up on the CDC 7600. It was subsequently checked out on one of the sample problems provided, modified to reduce central processor time by about a factor of two, and rewritten into subroutine format.

1.4 References

- ¹D. A. Powers, Molten Core - Concrete Interactions Project Description, Schedule 189 No. A-1019 (Albuquerque: Sandia Laboratories, Oct 1975).
- ²D. A. Powers et al, Exploratory Study of Molten Core Material/Concrete Interactions July 1975 - March 1977, SAND77-2042, (Albuquerque: Sandia Laboratories, Feb 1978).
- ³I. Prigogine and R. Defay, Chemical Thermodynamics, (London, England: Longmans, 1962).
- ⁴N. Z. Shapiro and L. S. Shapely, RAND Corp Memo 4205-PR, NTIS No. AD-605 316, Rand Corp., Santa Monica, CA, "A Generalized Technique for Eliminating Species in Complex Chemical Equilibrium Calculations," Sept. 1964.
- ⁵H. J. Hancock and T. S. Motzkin, Proc 1st Conf High-Temp Sys, pp 82-9 (1960).
- ⁶S. H. Storey and F. Van Zeggeren, "Computation of Chemical Equilibrium Compositions," Canadian J Chem Eng 17:54 (1964).
- ⁷F. Van Zeggeren and S. H. Storey, The Computation of Chemical Equilibria, (Cambridge, MA: Cambridge University Press, 1970).
- ⁸S. H. Storey and F. Van Zeggeren, "Computation of Chemical Equilibrium Compositions II," Canadian J Chem Eng 48:591 (1970).
- ⁹W. Akaike, Ann Inst Statist Math Annual Report, Tokyo 11:1 (1959).
- ¹⁰W. R. Smith and R. W. Missen, "Calculating Complex Chemical Equilibria by an Improved Reaction Adjustment Method," Canadian J Chem Eng 46:269 (1973).
- ¹¹W. D. Madeley and J. M. Toguri, "Computing Chemical Equilibrium Compositions in Multiphase Systems," Ind Eng Chem Fund 12:261 (1973).
- ¹²W. R. Smith, "Some Remarks on the Calculation of Complex Chemical Equilibria by General Methods," Ind Eng Chem Fund 15:227 (1976).
- ¹³S. R. Brinkley, "Calculation of the Equilibrium Composition of Systems of Many Constituents," J Chem Phys 15:107 (1947).
- ¹⁴F. G. Blottner, Hydrodynamics and Heat Transfer Characteristics of Liquid Pools with Bubble Agitation, SAND79-1132 (NUREG/CR-0944; Albuquerque: Sandia Laboratories, nd). To be published.
- ¹⁵G. B. Wallis, "Some Hydrodynamic Aspects of Two-Phase Flow and Boiling," Proc of the 1961-62 Heat Transfer Conference, Boulder, Colorado (New York, NY: American Society of Mechanical Engineers, 1963).

- ¹⁶S. S. Kutateladze and I. G. Malenkov, "Boiling and Bubbling Heat Transfer Under the Conditions of Free and Forced Convection," 6th International Heat Transfer Conference, Toronto, Canada (1976) (Washington, DC: Hemisphere Publishing Corp., 1978).
- ¹⁷D. A. Powers, "Influence of Gas Generation on Melt/Concrete Interactions," Proc IAEA Symp Therm of Nucl Materials, 29 Jan-2 Feb 1979, Julich, Germany. To be published.
- ¹⁸D. A. Powers, Light Water Reactor Safety Research Program Quarterly Report, April-June 1978, SAND78-1901 (Albuquerque: Sandia Laboratories, Jan. 1979), Chap. 1.
- ¹⁹V. K. Dhir, I. Catton, and J. Castle, "Role of Taylor Instability on Sublimation of a Horizontal Slab of Dry Ice," J Heat Trans, 99(3): 411-18 (August 1977).
- ²⁰H. Alsmeyer et al, A Model Describing the Interaction of a Core-Melt with Concrete, (NUREG/TR-0039; Washington, DC: U.S. Nuclear Regulatory Commission, Sept 1978). Translation of KFK 2395 (Karlsruhe, West Germany: Kernforschungszentrum, 1977).
- ²¹V. V. Konsetov, "Heat Transfer During Bubbling of Gas Through Liquid," Int J Heat Mass Trans, 9:1103-08 (1966).
- ²²W. F. Hart, "Heat Transfer in Bubble-Agitated Systems. A General Correlation," Ind Eng Chem Process Des Dev, 15(1):109-14 (1976).
- ²³V. N. Sokolov and A. D. Solomakhin, "Heat Exchange Between a Gas-Liquid System and a Heat-Exchange Element," Zhurnal Prikladnoi Khimi, 35(11):2570-73 (1962).
- ²⁴R. Greif, "Heat Transfer with Gas Injected at the Surface," Int J Heat Mass Tran, 8:1254-54 (1965).
- ²⁵J. Szekely and N. J. Themelis, Rate Phenomena in Process Metallurgy, Wiley-Interscience (New York: John Wiley and Sons, 1971).
- ²⁶H. Werle, "Modellexperimenten zum Kernschmelzen," Halbjahresbericht 1978/1, PNS 4332 (Karlsruhe, West Germany: Kernforschungszentrum, nd). In progress.

2. Steam Explosion Phenomena
(L. D. Buxton, W. B. Benedict, M. L. Corradini,
D. E. Mitchell, L. S. Nelson, R. Woodfin)

2.1 Summary

The purpose of the steam explosion phenomena program is twofold: (1) to identify experimentally the magnitudes and time characteristics of pressure pulses and other initial conditions which are necessary to trigger and to propagate explosive interactions between water and molten Light Water Reactor (LWR) core materials; (2) to development criteria to assess the probability and consequences of steam explosions during a hypothetical meltdown accident in a LWR. The major efforts in this program encompass five areas which are discussed fully later on.

- Small-scale experiments using simulant molten materials (corium-A, -E, and iron-oxide, ≤ 15 g) with water. These experiments are directed toward understanding the applied triggering pressures needed to induce a vapor explosion; and the propagation phase under a variety of initial conditions.
- A large-scale open-geometry test series using thermitically generated melts (previously iron-alumina, now corium-E ~ 25 kg) dropped into water. The purpose of these experiments is to determine the explosive interaction potential of these melts at large scale in order to improve the design of the closed geometry tests.
- The large-scale, closed-geometry, fully-instrumented test series using induction-generated melts (iron-oxides, corium-E ~ 25 kg) dropped into water. These experiments are directed toward observing, at larger scale and with prototypic melts, the efficiency and

propagation of the explosion as functions of fuel and coolant temperatures, mass ratios, and composition.

- Theoretical analysis of steam explosions to interpret the observed experimental results in light of past theories and models of steam explosions (vapor explosion) and supplying additional modeling effort where past work has proven inadequate. The ultimate objective is to be able to relate the experiments performed and the results obtained to the possible behavior of a steam explosion during a meltdown accident by using a consistent modelling and scaling analysis.
- Assessment of containment failure resulting from steam explosions to evaluate how a steam explosion may lead to containment failure caused by missile generation or overpressure conditions, and to identify and evaluate the realistic mechanisms that could dissipate the explosions' energy and reduce the probability of containment failure.

2.1.1 Small-Scale Experiments

The single-drop scoping studies were continued this quarter, looking at several high temperature materials. An attempt was made to prepare thermite drops by laser ignition, but single, coherent drops could not be produced. Levitated drops of molten iron were injected into water, with bridgewire impulse added. Noncondensable gas formed around the drops, probably hydrogen; fragmentation could not be achieved with a bridgewire pressure transient. Molten zirconia drops (a simulant of molten uranium dioxide) were prepared by a metal combustion technique. These drops were injected into water at temperatures above 3000 K. They also seemed to generate noncondensable gas; also, coarse fragmentation could be initiated with the bridgewire. The noncondensable gas produced with the molten zirconia may involve the thermal dissociation of water. Some studies related to dropping single drops were performed; namely, the careful characterization of bridgewire pulses.

The debris from molten iron oxide and aluminum oxide single-drop explosions was examined. In both cases, essentially spheroidal particles were formed, with varying void fractions. No mossy particles were seen in contrast to their earlier observation in the arc melting and field studies.

Sifted debris from an unusual arc melting experiment with molten iron oxide was analyzed by wet chemistry. No correlation between melt oxygen content and particle size was noted.

2.1.2 Open Geometry Test Series

There was no significant activity to report this quarter.

2.1.3 Fully Instrumented Test Series (FITS)

The contract for construction of the design chamber has been placed. Delivery is scheduled for October 1979. In the area of melt generation and injection, 1- to 5-kg specimens of iron and iron-oxide (Fe_2O_3) seeded with about 20 weight percent (w/o) iron were inductively melted in graphite crucibles. The final composition is being analyzed. Also experiments using steel dropped into water were performed to evaluate the stressed glass cylinders which allow the melt to fall below the water surface. These experiments demonstrated the feasibility of the stressed glass technique. Finally, a preliminary test plan which defines the test sequence has been completed.

2.1.4 Theoretical Analysis

Phenomenological modelling of steam explosions this quarter addressed three areas.

An hypothesis has been advanced that the observed explosion cutoff for high ambient pressures and coolant temperatures is a function of the pressure trigger energy. As the trigger increases in impulse and energy, the cutoff pressures and temperatures should also increase. The film boiling and collapse which led to this hypothesis was used this quarter to predict the film collapse behavior in "separate effects" experiments

conducted by Inone et al.¹ The results show good agreement between model and experimental data, thereby lending credence to the results of the model when applied to film collapse in vapor explosions.

The melt fragmentation mechanism is a key element in the propagation phase of the explosion. Analysis indicates that, for the range of materials in the LWR core melt scenario, the dominant fragmentation mechanism appears to be due to Taylor instabilities generated by local pressurization of fuel and coolant where liquid-liquid contact has been established after film collapse. This conclusion is different from the proposed mechanism of Theofavous². Cavitation of melt may have a role in the fragmentation event although no definitive proof seems to exist. The same conclusion about cavitation can be made concerning the tests of Patel³.

A simple model for the propagation of the vapor explosion has been developed and was applied to the small-scale experiments of Nelson. The results indicate that the whole propagation event takes place in about 40 μ s considering local pressurization as the fragmentation mechanism. This is in agreement with high-speed movie observation that the event occurs in less than 200 μ s. Also the thermal-to-mechanical conversion ratio was calculated to be about 3%.

2.1.5 Assessment of Containment Failure

The dissipation of the kinetic energy of the coolant slug by heat transfer was parametrically investigated for full-scale LWR accident conditions. The results indicated that the kinetic energy prior to impact can be reduced by a factor of 2 to 5 depending on the initial conditions of the expansion; eg, amount of coolant vapor involved and/or the initial pressure of the interaction. This analysis was also applied to Buxton's open geometry tests to illustrate the reduction in work done by the coolant because of heat transfer.

Structural modelling of the slug impact on the vessel head and its possible failure were pursued in two areas this quarter:

- the short-time structural response of the vessel to shock waves generated by the explosion are being modelled by using the HONDO code; preliminary results were obtained.
- long-time structural response to vessel head impact is to be modelled using HONDO to determine the types of failure possible similarity analysis was completed for future scale modelling studies.

2.2 Small-Scale Experiments (L. S. Nelson 5836)

2.2.1 Thermite Drops

Several attempts were made to prepare single drops of thermite melt by laser initiation of the thermite reaction. Miscellaneous chunks, 3 or 4 mm across, were suspended on iridium wire, and moved into the focus of the carbon dioxide laser, which was operating at about 50-W continuous wave. Both stoichiometric magnetite-aluminum thermite, and 10 w/o excess iron thermite were used. In each case, the thermite pieces blew apart on ignition, and generated only tiny molten spheres. The experiments were discontinued.

2.2.2 Molten Iron Drops

Levitated iron drops (diameter = 5 mm; weight = 0.6 g) in flowing, high purity argon were prepared in the upper portion of the apparatus described by Stephens⁴. After raising the drop above the melting temperature, it was released through a fast-acting valve and injected into water at 273 K. High-speed films showed that immediately upon entering the water, the drop was encased in a "bag" of noncondensing gas 1 to 2 cm in diameter; a typical frame from one of the films is reproduced in Figure 2-1. Bridgewire stimulation of the interacting metal and water did not produce fragmentation or explosion. The noncondensable gas is probably hydrogen, produced by the iron-water reactions. Calculations of expected bubble diameters were made from reported rate constants as follows:⁶

For the reaction of molten iron with steam,

$$\frac{W^2}{t} = 1.41 \times 10^{11} \exp(-90\,800/RT) \quad (2.1)$$

or

$$\frac{W^2}{t} = 2.40 \times 10^{12} \exp(-84\,300/RT) \quad (2.2)$$

where

W = weight gain due to oxidation in mg/cm²

t = time in s

R = gas constant, 1.987 ca./gmole K

T = temperature in K



Figure 2-1. Bubbles of Noncondensing Gas Generated by Molten Iron Drop (marked by the arrow) Injected Into Water Subcooled 95 K. Drop (weight = 0.6 g) had been levitation-melted in argon prior to release through a fast-acting valve into the water. The cylindrical object at the left is the holder for the submerged exploding wire (bridgewire), which had been fired prior to this image. No explosion or fragmentation resulted. The bubbles shown rose and eventually popped at the surface of the water. Calibration bar at upper left is 10 mm long. (11-9-1).

Assume the reaction



An iron drop at 1800 K weighing 0.6 g should produce bubbles of $d = 4.1$ cm diameter from equation 2.1, or 0.39 cm diameter from equation 2.2 in a 10-ms reaction time. These diameters agrees approximately with those observed on the films for similar time intervals.

2.2.3 Molten Zirconia (Uranium Dioxide Simulant)

Another technique for preparing single drops of molten oxidic materials, typical of LWR core melts, was explored.* This technique uses the combustion of metal drops in free fall through oxygen-containing atmospheres.⁷ A piece of zirconium metal was ignited by radiation from a 1-kW quartz iodine lamp placed about 5 cm away. The experiment involved a strip of foil 12 x 25 mm, 51 μm thick, placed at the top of a 2-m-tall drop tube that contained a pure oxygen atmosphere at local atmospheric pressure, 0.083 MPa. At the end of the fall, the drop was injected into room temperature water. Bridgewire stimulation was applied a few tens of milliseconds after injection. As in the molten iron experiments, bubbles of noncondensable gas were formed; but coarse fragmentation could be initiated with the bridgewire. A frame from one of the films is shown in Figure 2-2. The conditions of injection of the drop were estimated from the literature, in the absence of direct measurements. The temperature of the drop was assumed to approach the boiling point of zirconium dioxide, (≈ 4000 K) according to the calculations of Doyle⁸. The composition of the drop was estimated to be approximately $\text{ZrO}_{1.6}$, using the total contact time and the oxygen uptake rate given by Nelson⁷. If the bubbles surrounding the drop truly contain noncondensable gas, as the films indicate, it is probably a mixture of hydrogen and oxygen produced by the thermal dissociation of water. At the temperature of drop injection, water is expected to be at least 50% dissociated (Figure 2-3).

*Three complementary techniques are being explored for generating single drops of prototypical core melt materials: (1) carbon dioxide laser melting of pendant drops (oxides), (2) levitation melting (metals), and (3) combustion heating (partially oxidized melts at very high temperatures).



Figure 2-2. Bubbles of Noncondensing Gas Generated by Molten Zirconia Drop Injected Into Water Subcooled ≈ 75 K. Drop (diameter ≈ 2.6 mm) had been prepared by combustion of a strip of zirconium foil in pure oxygen at a pressure of 0.083 MPa. Drop temperature upon injection into water was estimated to be >3000 K; drop can position, was estimated to be $ZrO_{\approx 1.6}$. The bubbles shown rose and eventually popped at the surface of the water. Calibration bar at upper left is 10 mm long. (11-18-1).

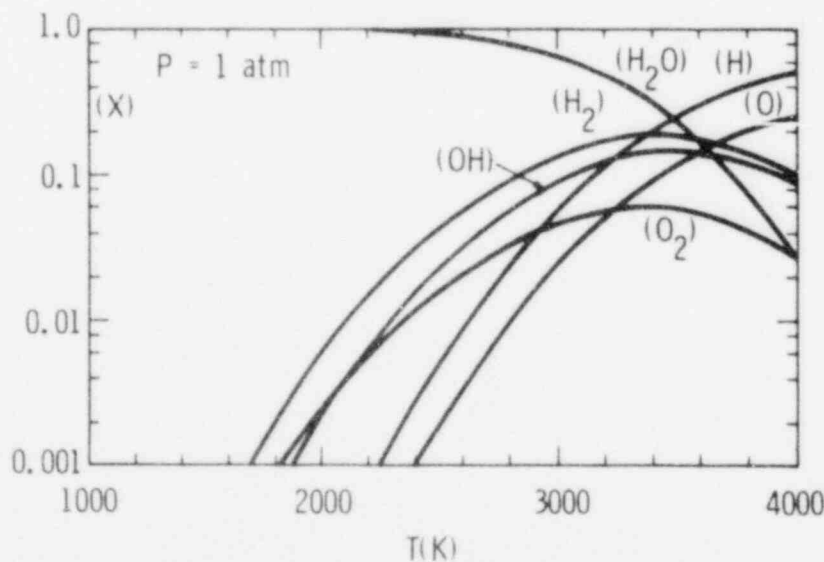


Figure 2-3. The Compositions of Dissociating Water Vapor at Thermodynamic Equilibrium⁵

2.2.4 Debris From Single Drop Experiments

Some debris particles retrieved from the explosions of single drops of molten iron oxide ($O/Fe = 1.33$) and aluminum oxide (Al_2O_3), retrieved from the explosions were cross-sectioned and examined with the scanning electron microscope. These samples of debris had a characteristic not seen before in our steam explosion experiments, that is, both floating and sinking debris. These two types of particles were examined separately for each oxide, with typical results shown in Figures 2-4 and 2-5. The debris from both materials is essentially spheroidal, with some void formation in both sets of particles. The aluminum oxide particles generated were about an order of magnitude larger in diameter (approximately $500 \mu m$) than those in the iron oxide debris (approximately $50 \mu m$). In neither case could mossy debris be observed, as was common in both the arc melted⁹ and field test experiments.¹⁰

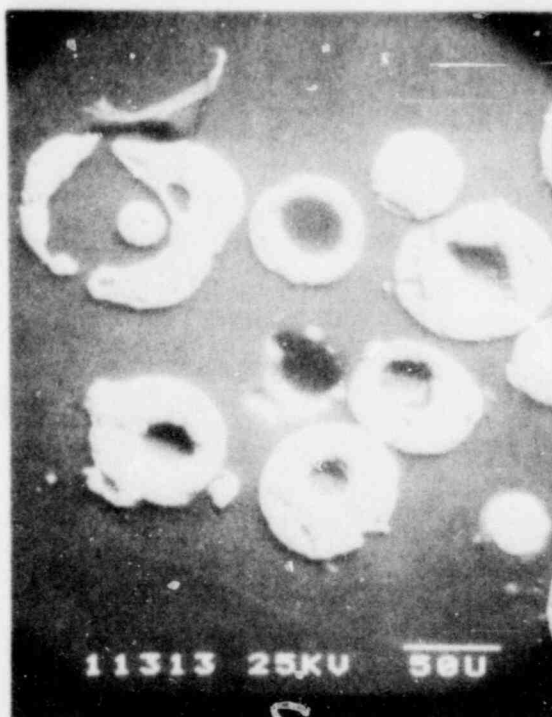
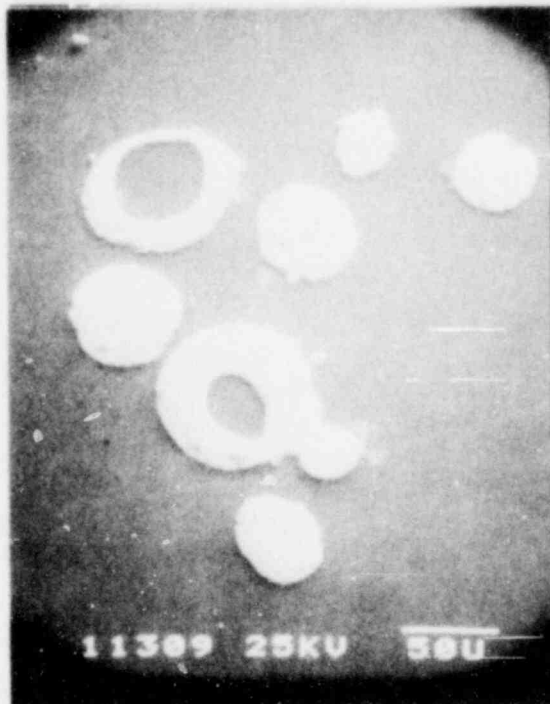
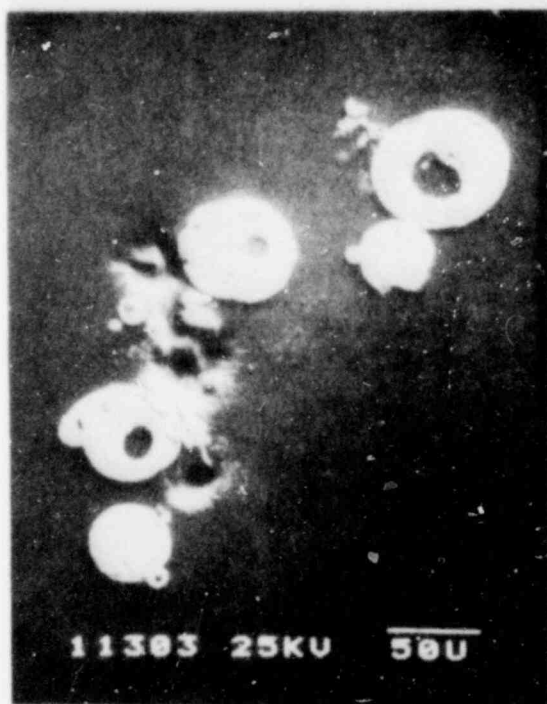
2.2.5 Related Studies

A series of experiments was performed to obtain an accurate measure of the impulse generated by a bridgewire in the single drop experiment. A special holder was built in which the bridgewire and two lithium niobate pressure transducers were carefully mounted in a reproducible position (80 mm apart, 65 mm beneath the water surface). The results of peak pressure measurements at three different voltages is shown in Figure 2-6. It should be noted that, at the lower voltage, perhaps a +20% uncertainty between points exists, while at the two higher voltages, the uncertainty was about +10%.

2.2.6 Wet Chemistry of Sifted Arc-Melting Debris

The purpose of this analysis was to correlate O/Fe ratio with particle size.

Debris from Single Drop of Laser-Melted $\text{FeO}_{\approx 1.3}$



Sank

Floated

Figure 2-4. Scanning Electron Micrographs of Debris in Cross Section Retrieved From a Steam Explosion Involving a Single Drop of Laser-Melted Iron Oxide. Composition of drop was $\text{FeO}_{\approx 1.3}$ at interaction time. Images at the left are those from debris which sank in the water after the explosion; those at the right floated. Bars are 50 micrometers long. (11-4-2).

Debris from Single Drop of Laser-Melted Al_2O_3

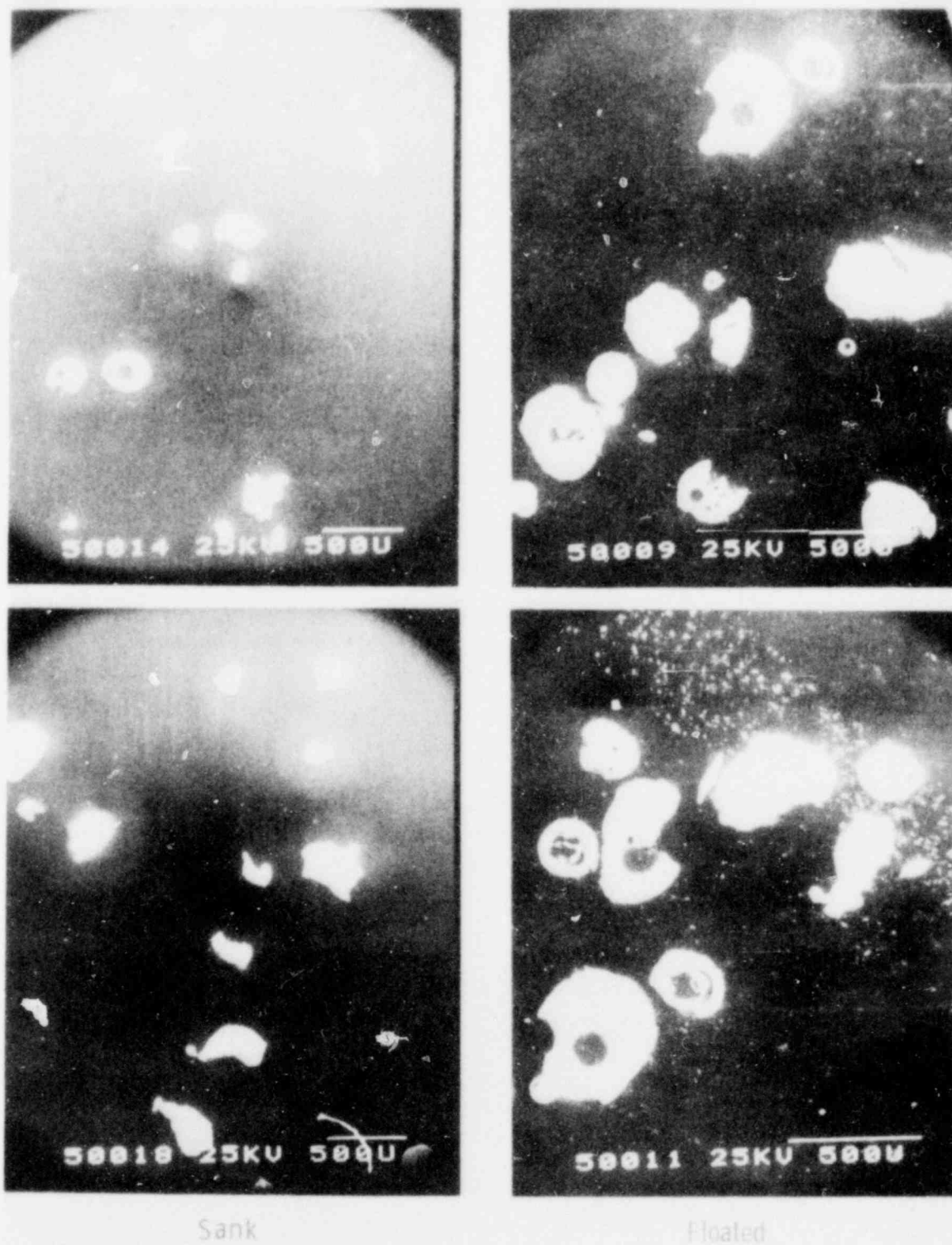


Figure 2-5. Scanning Electron Micrographs of Debris in Cross Section Retrieved From a Steam Explosion Involving a Single Drop of Laser-Melted Aluminum Oxide. Drop composition was Al_2O_3 at interaction time. Images at the left are those from debris which sank in the water after the explosion; those at the right floated. Bars are 500 micrometers long. (11-4-2).

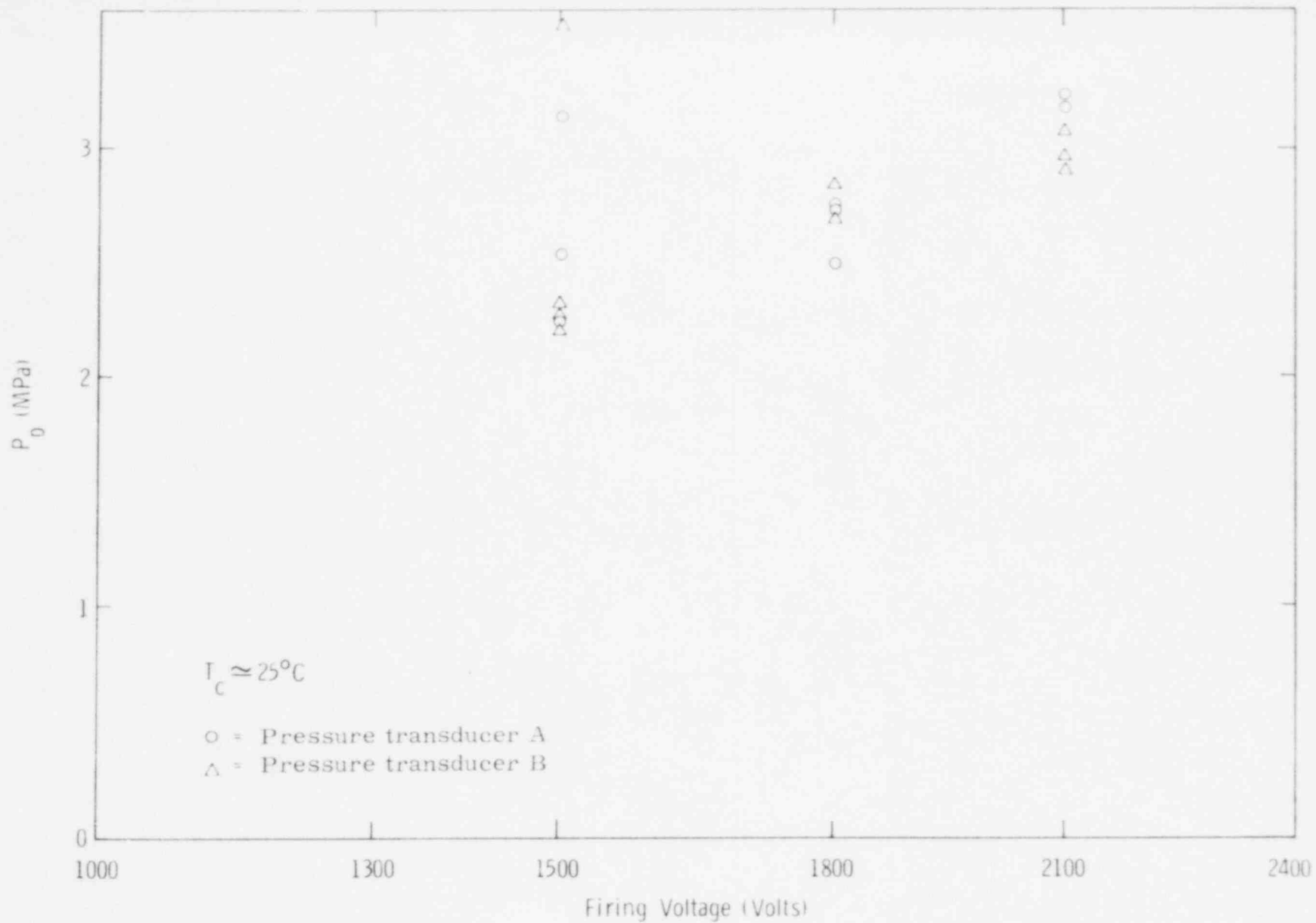


Figure 2-6. Peak Pressures, P_p , Recorded for Bridgewire Pressure Transients as a Function of Firing Voltage. Pressures were measured with two lithium niobate pressure transducers each placed 80 mm from the bridgewire, all at a common depth of 65 mm below the surface of the water.

A carefully sifted sample of debris (experiment 10-39-2) was subjected to wet chemical analysis for each of the six fractions of the debris. This sample was selected because it was produced in the experiment which generated the highest peak pressure of any experiment done in the arc melter (5.7 MPa). In this particular experiment, which used the initial oxygen-iron ratio of 1.33, (produced by mixing iron and hematite powders) much of the debris had a reddish cast, particularly in the larger size fractions. The results presented in Table 2-I seem to show no particular O/Fe ratio for a given particle size range, and no trends to the other sizes. Further chemical analyses of individual sifted debris samples from the arc melting experiments will be attempted.

Table 2-I
Analytical Results for Sample 10-39-2

Size Fraction (μ m)	Weight Percent Fe	Ratio O/Fe	Method
0-45	75.6	1.127	Gravimetric (G)
	75.2	1.151	G
	73.1	1.285	Volumetric (V)
75-150	72.6	1.317	G
	75.0	1.164	G
	79.5	0.900	V
	73.0	1.291	V
	72.0	1.357	V
	71.9	1.364	
150-180	71.6	1.385	G
	72.4	1.331	G
180-250	79.1	0.922	G
	71.6	1.385	G
425-850	72.2	1.344	G
	75.6	1.267	G
	67.6	1.673	V
	68.1	1.635	V
7850	74.1	1.220	G
	70.6	1.454	G
	66.4	1.766	V
	68.3	1.620	V

2.3 Open-Geometry Test Series (L. D. Buxton, 5551, W. Benedick, 5131)

There is no significant activity to report during this quarter.

2.4 Fully Instrumented Test Series (D. E. Mitchell, 2514)

Progress in preparing for the FITS experimental programs is described by subject below.

2.4.1 Interaction Chamber

Design drawings for the interaction chamber were reviewed, and a contract for construction has been placed. Delivery is scheduled for October.

The high-speed closure, for isolating the melt section from the interaction chamber, has been evaluated and found to be satisfactory, although it will require some modification.

2.4.2 Melt Generation and Injection

Melting experiments are in progress at Building 9939. The experiments are being used to gain familiarity with the power supply, optimize furnace coil design, and evaluate crucibles.

Items critical to producing successful metal and metal oxide melts include the balance of capacitance in the power supply with the inductance of the coil, lead length, and coil parameters. Also the composition, quantity, and density of material to be melted, size of susceptor effectiveness of thermal insulation, and ability to measure the melt temperature are considered. Most of these items have been defined in terms of the power available from the Inductotherm power supply.

Specimens of 1 to 5 kg of iron and iron oxide (Fe_2O_3) seeded with about 20 w/o iron were prepared in graphite crucibles. The melt temperature of the iron/iron oxide melt was measured by pyrometer to be 1460°C. The composition of the resulting material has not yet been determined.

2.4.3 Instrumentation

Additional support from Ktech Corporation has been obtained to assist in installing and setting up instrumentation. A preliminary test plan which defines the test event sequence, types of instrumentation, and number of data channels has been completed.

2.4.4 Site Preparation

Site plans have been reviewed, a contract for construction has been placed, and construction has begun. Site completion is scheduled for September.

2.4.5 Experiment Development

Experiments using ~10 g of molten steel were performed. These specimens were melted using an oxy-acetylene torch and were dropped into stressed glass cylinders which were submerged in water. Glass breakage was not repeatable due to the fact that the quantity and temperature of the molten specimens could not be precisely controlled. In order to perform more repeatable experiments, the glass was broken with a TC817 mini-slapper device after the melt entered the cylinder. These experiments showed that the stressed glass technique is feasible and that the melt can be viewed before coming in contact with the water. Explosions were not expected and none were produced.

2.5 Theoretical Analysis (M. L. Corradini 4441)

The experimental results of the small-scale experiments have been reported by Nelson and Buxton (Reference 8 for arc melter experiments and this quarterly for new melting techniques). The purpose of this portion of the steam explosion research is to analyze the experimental results in regard to full-scale reactor conditions.

2.5.1 Effect of Melt Composition on the Vapor Explosions

In the last quarterly it was suggested that a change in thermo-physical properties (eg, T_{melt} , σ_{melt}) may be responsible for the explosion suppression at low oxygen contents. However recent experiments by

Nelson, as reported in this quarterly, indicate another feasible explanation. The dropping experiments using pure iron have indicated that noncondensable gases surrounded the iron droplet (~1 cc). This noncondensable gas, probably hydrogen, came from water reduction and iron oxidation. Thus film collapse needed to initiate an explosion could be retarded by the thick noncondensable film, given the constant bridgewire trigger pulse. This same behavior may also explain the lack of explosivity of the stainless steel, corium-A, and FeO tests in the arc melter. All of these substances are metal rich and, in the oxidizing environment of hot steam, hydrogen could be produced and could retard film collapse. More tests are planned to sample the cover gas to detect hydrogen, and analysis is underway to see the effect of noncondensibles on film boiling collapse.

2.5.2 Water Subcooling and Ambient Pressure Effects on Vapor Explosions

In previous quarterlies,^{10 11} the hypothesis has been advanced that the explosion cutoff for ambient pressure and water temperature is a function of trigger magnitude. This has been shown to be the case, based upon a transient film boiling and collapse model which was applied to the Fe₂O₃ - water system using Nelson's initial test conditions for the explosive second stage interaction. To further investigate the transient model used, the same analysis has been done for the "separate effects" film collapse tests of Inoue.¹ The objective here was to compare the model prediction for the peak heat flux after film collapse with that obtained from the experiment. In this way a more definitive test of the model and its assumptions could be made. The film collapse model has been previously explained¹² and the only difference here is the geometry and the initial conditions of the test. The apparatus employed by Inoue was a low pressure vertical shock tube into which a heated hollow nickel wire, 3 mm OD and 0.07 mm thick, was placed (Figure 2-7). Resistive heating of the wire established film boiling between it and the coolant (Freon-113) at a known nickel surface temperature. The experiment consisted of passing a shock wave of adjustable peak pressure (P_p) and rise time (τ_p) through the liquid coolant causing film destabilization. The current and voltage were monitored during the transient to determine the peak heat

flux (q_p'') during film destabilization. The tests measured q_p'' over a range of initial (P_∞) and final pressures (P_p), shock rise times (τ_p), and heater surface temperatures (T_H). A more detailed description of the apparatus is given by Inoue¹.

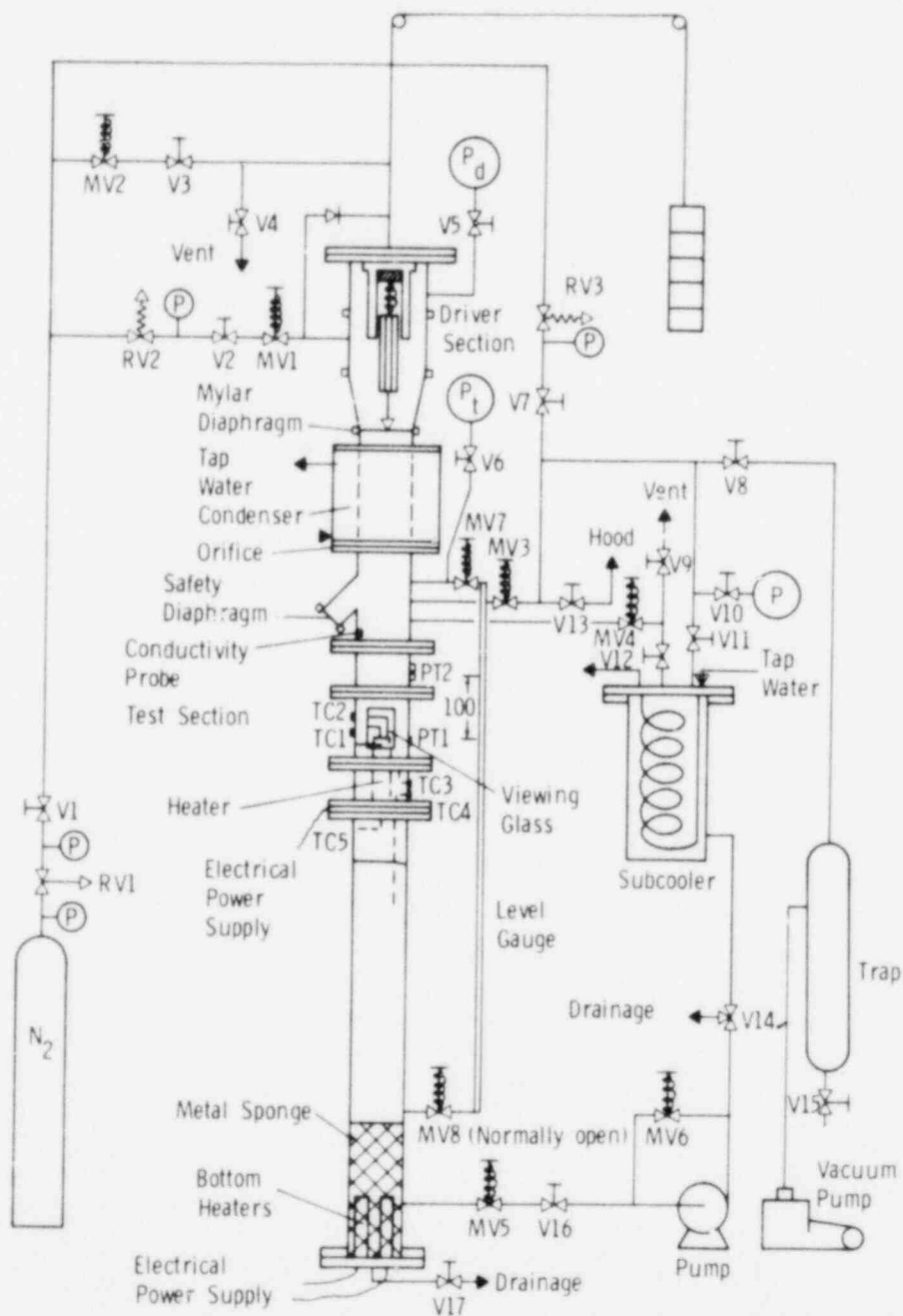


Figure 2-7. Schematic Description of the Shock Tube. Dimensions in mm. MV - magnetic valve; RV - regulating valve; V - manual valve.

Both equilibrium and nonequilibrium vapor-liquid conditions were used to describe the heat and mass transfer at the interface. The results of the analysis are given in Figures 2-8 through 2-11. A quick survey of all these figures leads one to the conclusion that the nonequilibrium interface condition successfully predicts the results over the range of experimental variables while the equilibrium model, although following the qualitative trends of the experiment, quantitatively underestimates the peak heat flux by a factor of 2 to 3. The reason for this difference is directly tied into how each model describes the rate of vapor condensation. The equilibrium model sets the interface temperature, T_I , equal to T_{sat} at the film vapor pressure. Therefore, instantaneous adjustment of T_I causes the condensation at the interface to change to net evaporation at an earlier stage of film collapse as film thickness decreases and heat transfer becomes dominant. This, in turn, increases the minimum film thickness, δ_{min} , during collapse lowering q_p'' which is inversely proportional to δ_{min} :

$$q_p'' \propto \frac{k_v}{\delta_{min}} (T_H - T_I) \quad (2.2)$$

The nonequilibrium model conversely retards coolant evaporation or condensation by a rate-dependent mass transfer model thereby causing δ_{min} to be smaller and q_p'' to be larger.

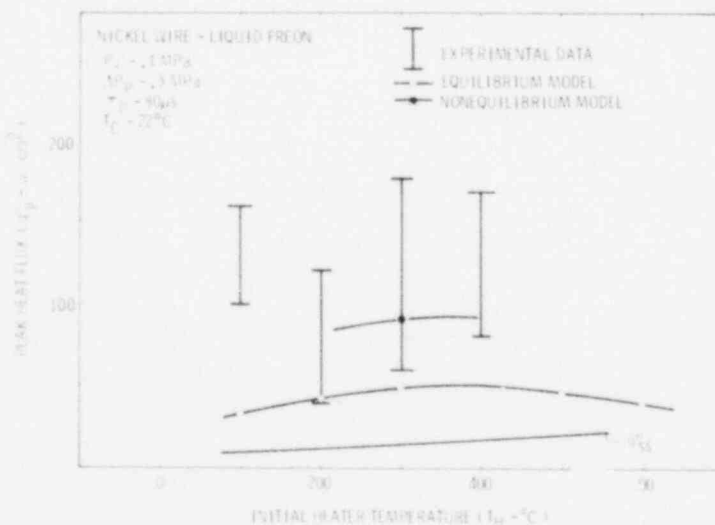


Figure 2-8. Variance of the Peak Heat Flux Due to Wall Heater Temperature

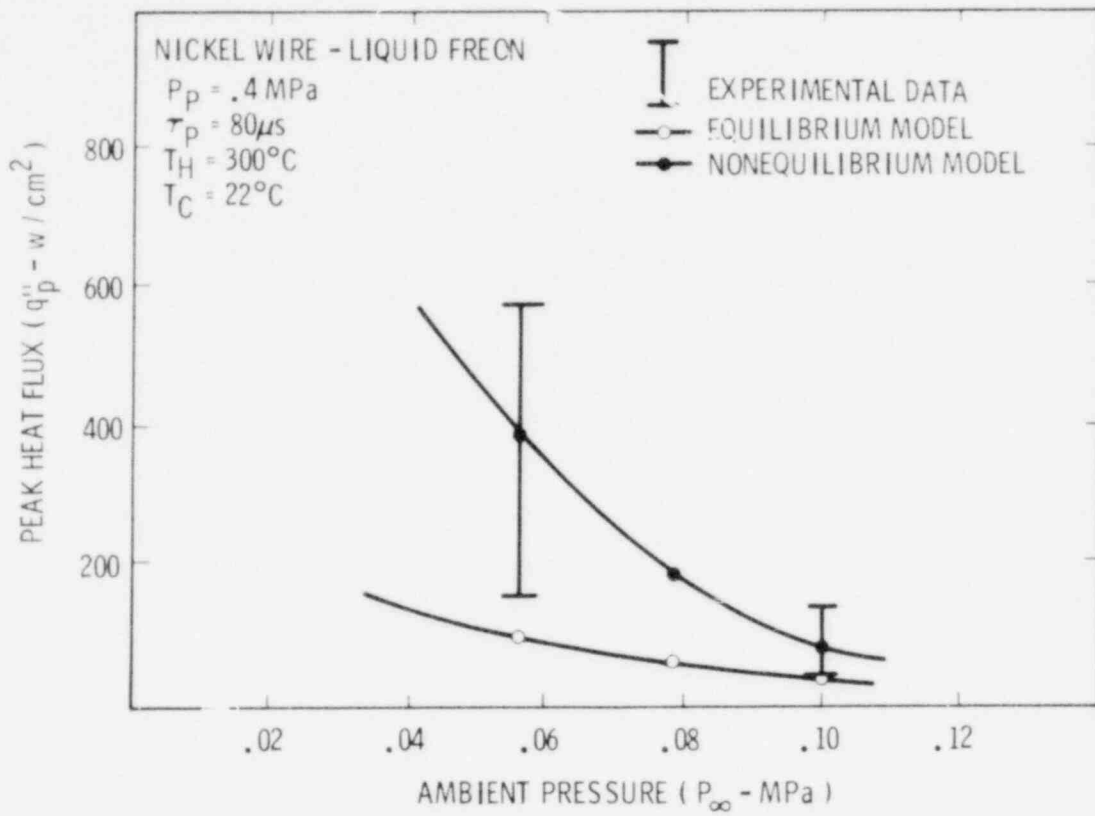


Figure 2-9. Variance of the Peak Heat Flux Due to Ambient Pressure

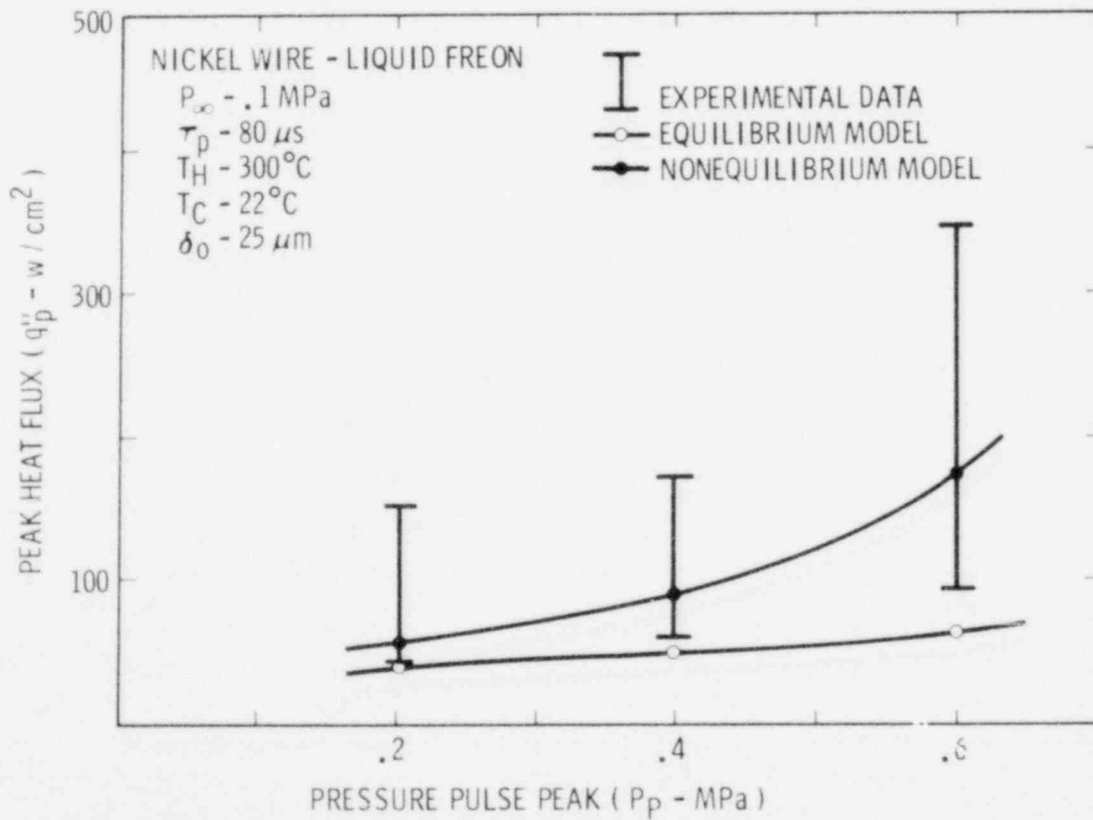


Figure 2-10. Variance of the Peak Heat Flux to Shock Pressure

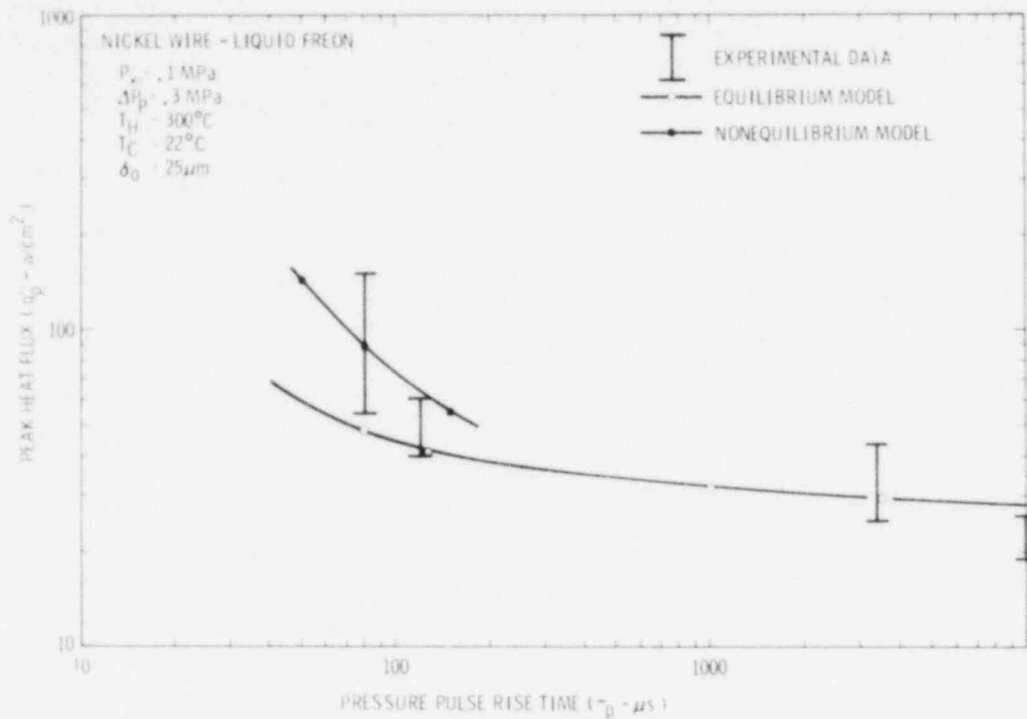


Figure 2-11. Variance of the Peak Heat Flux Due to Shock Rise Time

The second thing to observe in Figure 2-8 is that q''_p goes through a maximum. This is caused by two counter-balancing effects: a higher temperature difference as T_H increases can increase q''_p , yet as T_H increases the minimum film thickness becomes larger. Figures 2-9 and 2-10 indicate the pressure trigger effect which is applicable to the question of explosion cutoff with increasing P_∞ . If the ambient pressure, P_∞ , is decreased or the shock pressure, P_p , increased, the film collapse is more complete, indicated by the higher values of q''_p . Thus an increase in P_∞ only serves to lower the trigger energy and thus makes the film more stable. If film collapse is needed to initiate the interaction, as is presently believed, then increases in P_∞ affect the ability of the trigger to collapse the film.

The effect of increasing the shock rise time, Figure 2-11, is to lower q''_p as both models predict. Also it indicates that the assumption of an equilibrium interface condition appears valid for $\tau_p > 100 \mu\text{s}$.

The successful prediction of these experimental results with the film collapse model lends credence to the analytical tools used in the vapor explosion analysis.

2.5.3 Fragmentation Mechanism in the Propagation Phase

The liquid-liquid fragmentation experiments of Patel and Theofanous at Purdue have been the focus of the melt fragmentation analysis.³ The code CSQ has been used to try to model the fragmentation event. Some success has been made in observing the whole event as the previous quarterly indicated.¹¹ However in trying to refine the mesh size we found that the calculation, although possible, became too expensive to attempt for more than $20 \mu\text{s}$ even though $t_{\text{FRAG}} \sim 500 \mu\text{s}$. Thus the purpose of the analysis was altered to identify if acoustic cavitation as well as Taylor instabilities were viable fragmentation mechanisms for the mercury-water tests. Theofanous has maintained that a negative pressure pulse is not generated in the mercury; therefore no cavitation can occur.⁹ Kazimi, however, maintains that a negative pressure pulse will be created by the passage of the planar shockwave across the mercury drop, and this allows the possibility of cavitation as well as breakup due to Taylor instabilities.¹²

A sample calculation was run with CSQ to determine if negative pressure and/or cavitating voids would develop in the mercury. Figures 2-12 through 2-15 illustrate the results of the calculation. The initial geometry of the analysis matches the experiment with a mercury drop (~ 0.5 cm diameter) in a water shock tube of 5-cm width. Because of the computational expense and time, the shock imposed here for the calculation ($P_{\text{sh}} \approx 80$ MPa) was a factor of two larger than that used in Theofanous experiment. The small dots are tracer particles used to follow the flow variables (eg pressure, temperature, velocity,) during the transient. The Figures 2-13 through 2-15 are tracer particle plots of pressure along the shock tube centerline in front of the drop, and at two points in the droplet downstream of its center.

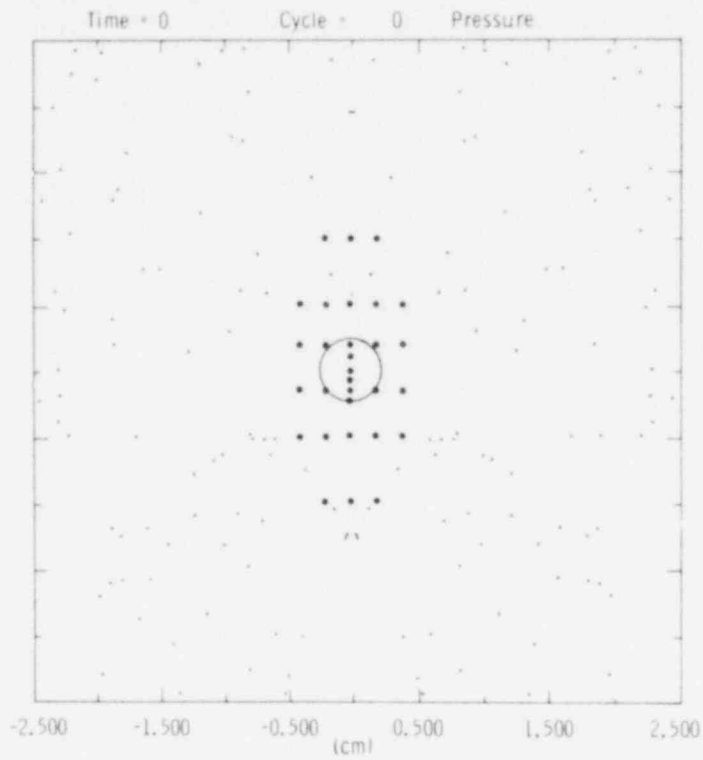


Figure 2-12. Initial Geometry for a Mercury Drop in Water

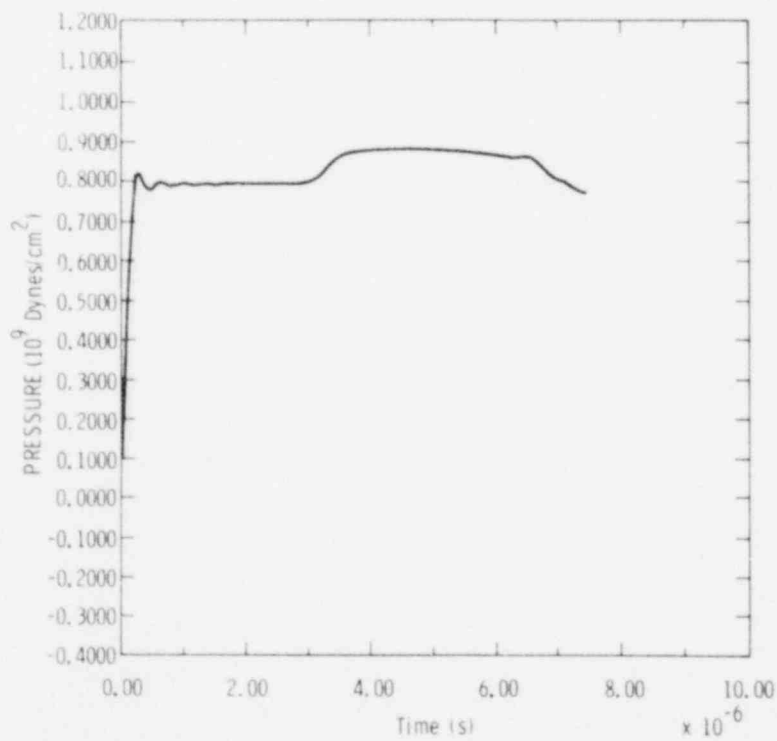


Figure 2-13. Shock Tube Pressure in the Water Upstream of the Mercury Droplet

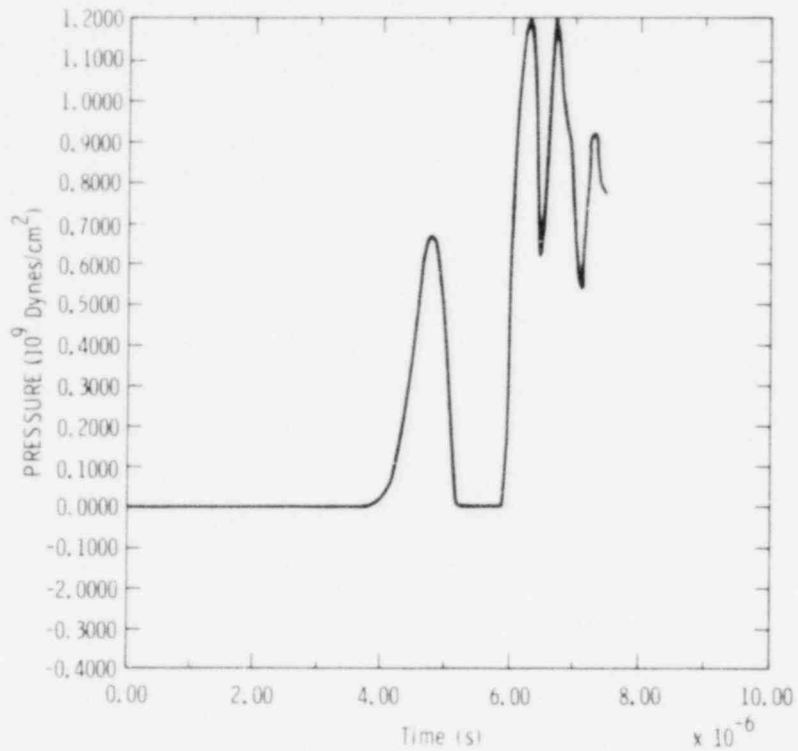


Figure 2-14. Pressure Within Mercury 0.12 cm Downstream of the Droplet Center

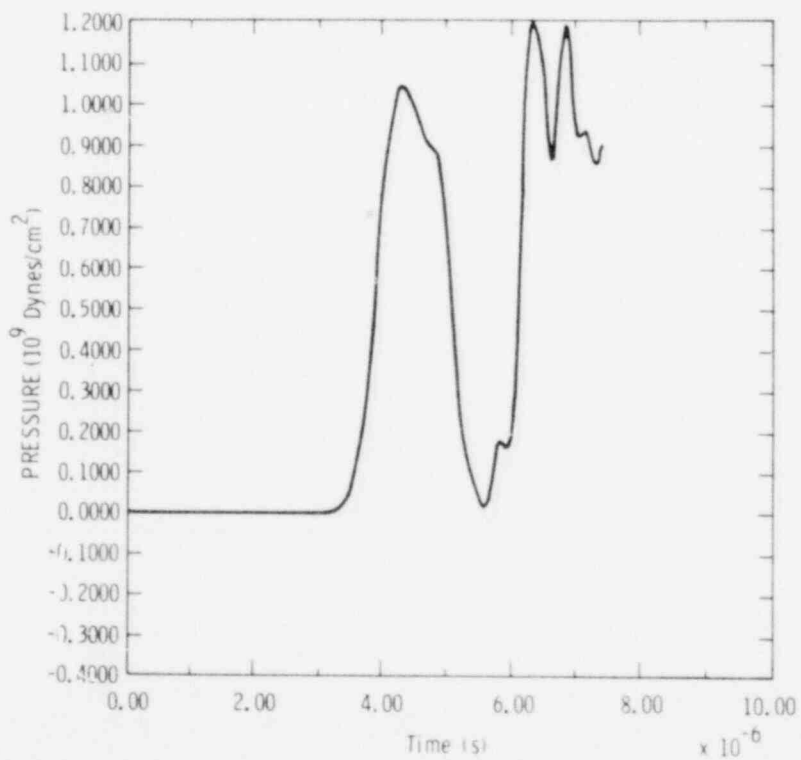


Figure 2-15. Pressure Within Mercury 0.18 cm Downstream of the Droplet Center

The figures indicate that the pressure indeed falls to zero at about 5.5 μ s to 6 μ s and a void forms. CSQ does not allow the pressure to go negative but rather forms a vapor bubble when the pressure falls near zero. The conclusion then is that a small portion of the mercury can experience negative pressures and voids can form. The next step in the analysis will be to determine if the void formation is sufficiently large to account for some portion of the observed fragmentation.

These two fragmentation mechanisms (Taylor instability caused by relative motion), and (cavitation due to shock passage) can also be operative in the vapor explosions Nelson has observed. There is also one other important fragmentation mechanism to consider, that being local pressurization of the coolant due to liquid-liquid contact after vapor film collapse. The interface temperature is so high for the LWR melt-water combinations that the local pressure associated with it is in the kilobar range and could account for the observed fragmentation. In Nelson's tests the explosion occurs in less than 0.2 ms (@ 5000 fps high-speed movie) and thus the time for the fragmentation is of this same order of magnitude.

Theofanous has suggested that the time of fragmentation due to relative velocity differences is U_{rel}

$$t_F = \left(\frac{1.7 D_d}{U_{rel}} \right) Bo^{-1/4} (\epsilon)^{1/2} \quad , \quad (2.3)$$

where

$$Bo = \frac{\rho_H a D_d^2}{4\sigma} \quad , \quad (2.4)$$

and

$$\epsilon = \left(\rho_H / \rho_c \right)^{1/2} \quad (2.5)$$

$$a = 3/4 \rho_c / \rho_H \left(\frac{U_{rel}}{D_d} \right)^2 \quad , \quad (2.6)$$

and where

D_d = drop diameter

ρ = density, H-melt, c-coolant

σ = surface tension

For Nelson's test with a trigger shock of 1 to 10 MPa, the maximum U_{rel} is 6.2 m/s; and for a 3-mm drop of Fe_2O_3 , $t_F \geq 0.30$ ms.

Fragmentation due to local pressurization occurs as the coolant in initial liquid-liquid contact with fuel melt rapidly expands as a vapor at high pressure. Thus the fragmentation time would be approximately

$$t_F \approx \frac{D_d}{V_r} , \quad (2.7)$$

where the relative fragmentation velocity V_r , is due to Taylor instability and is given by

$$V_r = 4.6 \sqrt{a\lambda_c} , \quad (2.8)$$

where

$$\lambda_c = 2\pi \sqrt{\frac{\sigma}{\rho_H a}} , \quad (2.9)$$

and the acceleration, a , is

$$a = \frac{(P_I - P_\infty)}{\rho_H D_d} , \quad (2.10)$$

for the local pressure P_I near or below the value

$$P_I = P_\infty + \left. \frac{\partial P}{\partial T} \right|_V (T_I - T_c) \quad (2.11)$$

$$T_I \approx \frac{\Gamma_H}{1 + \beta} \frac{\beta T_c}{1 + \beta} \quad (2.12)$$

$$\beta = \sqrt{\frac{k_{\rho^c c}}{k_{\rho^c H}}} . \quad (2.13)$$

Thus for Nelson's test let us assume film collapse occurs and generates liquid-liquid contact, for $T_H \approx 2500$ K and $T_C \approx 300$ K. Using constant properties in the equations above, the fragmentation time is $t_r \approx 20 \mu s$ or 0.02 ms. Thus the local pressurization mechanism is much faster and within the 0.2-ms experimentally observed explosion window.

The cavitation fragmentation mechanism is much harder to quantify beyond demonstrating there is a negative pressure field for voids to form in. The two crucial questions associated with it are (1) do voids grow at a fast enough rate, controlled by vapor production or noncondensable gas diffusion to the void and (2) how many voids are necessary to account for observed fragmentation and are both of these dynamic processes reasonable within the negative pressure regions of a melt drop.

More analysis for all these mechanisms is planned.

2.5.4 A Simple Propagation Model for Nelson's Small-Scale Tests

The new small scale experiments done by Nelson as reported in this quarterly allow much better analysis of the data for a number of reasons:

- The amount of fuel participating in the interaction is well known
- The geometry is spherical which allows some analytical simplifications
- The interaction can be more easily viewed by instruments and high-speed movie equipment

Nelson has reported a successfully triggered vapor explosion ($\Delta P_p \sim 1.6$ MPa) for $FeO_{1.3}$. From high-speed movies it appears the whole interaction occurs in one frame of the film or the time for the explosion, $\Delta t_{exp} \leq 0.2$ ms (200 μs).

The key assumption made in this analysis is that water properties in the range of pressures greater than 100 MPa and temperatures greater than 1000 K are constant. This is the best approach available at this

time because of the lack of data on water properties in this range. Work is currently underway to extend water properties analytically into this region. Figure 2-16 depicts the propagation mechanism that is believed to occur. The melt is in film boiling with the coolant and, after trigger pulse passage, the film collapses initiating liquid-liquid contact. The temperatures are such that in the region near the melt in a constant volume heating time, t_{Ht} , the coolant is at a supercritical temperature (T_I) and the local pressure (P_I) is large. The coolant locally expands as a vapor under this pressure and begins to fragment the melt and coolant in a time, t_F . This drives the melt into another liquid-liquid contact and the cycle starts over, until the coolant vapor drives the constituents apart or the melt has solidified and fragmentation essentially ceases.

The heat transfer rate for the process is shown in Figure 2-17 where the energy transferred per unit area in time, t_{Ht} is, from conduction theory,

$$\Delta q \Big|_{t_{Ht}} = \frac{2k_H (T_H - T_I) \sqrt{t_{Ht}}}{\sqrt{\pi\alpha_H}} \quad , \quad (2.14)$$

where T_I is given by Eqs 2.12 and 2.13. The heat transfer rate is found by dividing the energy transferred in t_{Ht} by the total cycle time, $t_{Ht} + t_F$. The rate of area generation due to fragmentation is modeled by

$$A(t) = \pi D_d^2 \left(1 + \pi D_F^2 N (1 - e^{-t/t_F}) \right) \quad , \quad (2.15)$$

where

D_d is the drop diameter

D_F is the fragmented diameter given by λ_c (Eqn 2.8)

N is the number of fragments given as

$$N = \frac{\pi}{6} D_d^3 / \frac{\pi}{6} D_F^3 \quad . \quad (2.16)$$

The two characteristic times, t_F and t_{Ht} , are defined in Figure 2-17; t_{Ht} being the local pressure relief time and t_F being given by eqs 2.7 to 2.11.

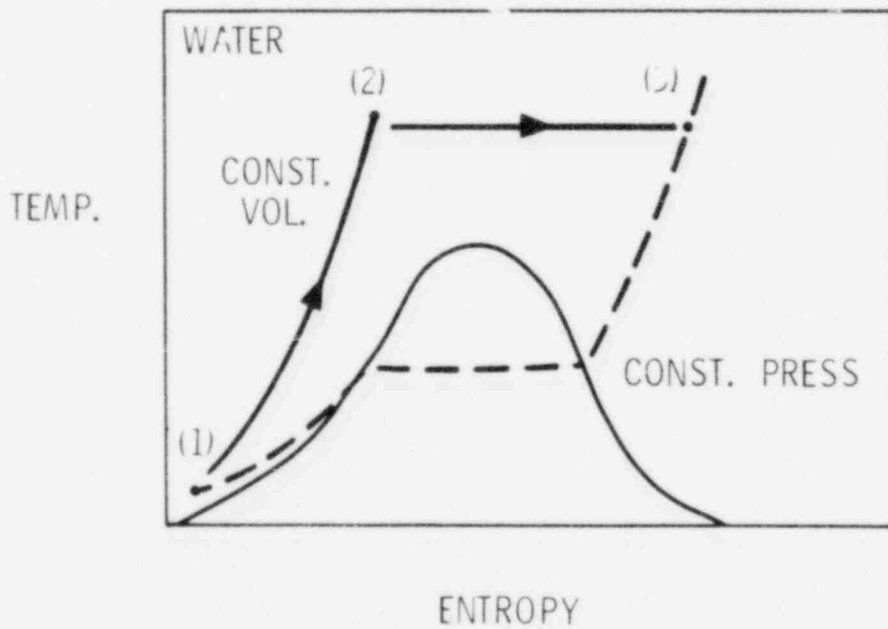
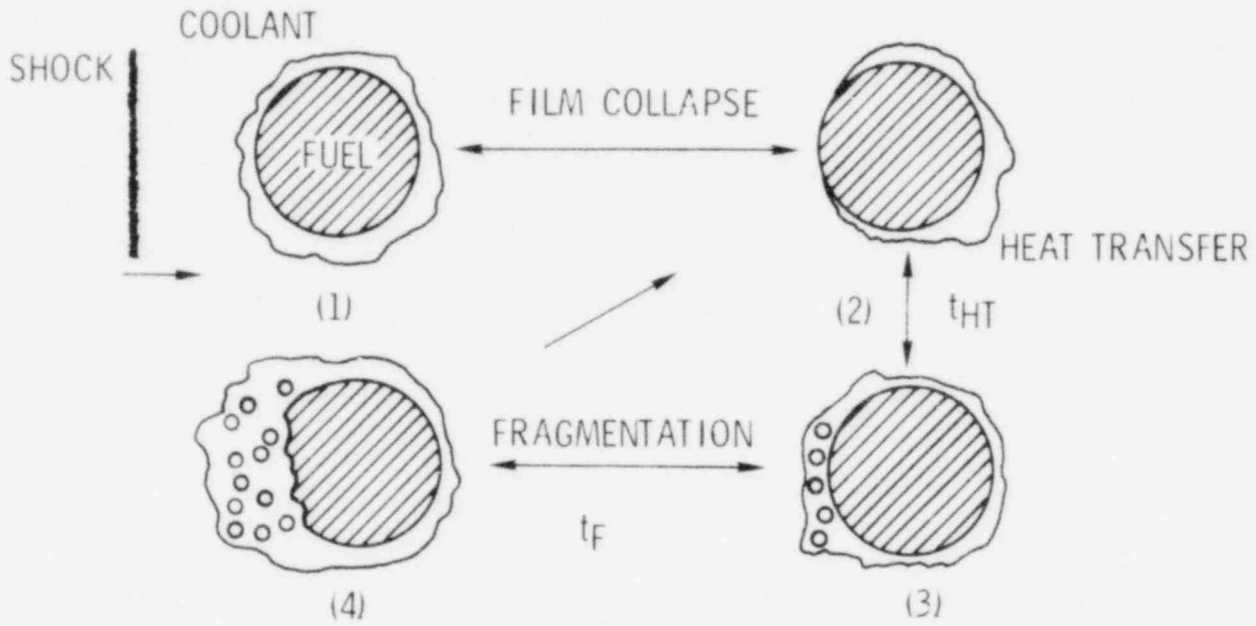


Figure 2-16. Propagation Phase; a Mechanistic View

This analysis is applied to Nelson's experiment and the results obtained are given in Figure 2-18. The droplet cooled down in air (Δt_{air}) by about 75° and 35°C in the water (Δt) mainly by radiation before the interaction began. For a pressure trigger similar to a bridgewire pulse (0.8 MPa for 20 μs) the film collapse process took about 40 μs . The explosive interaction occurs quite rapidly $\sim 40 \mu\text{s}$ mainly because the fragmentation size is more than a factor of 100 less than D_d . This fragmentation size agrees reasonably well with posttest SEM where all the fuel particles were less than 50 μm in size. Also the time for the interaction falls within the explosion time window of $t_{\text{exp}} \leq 0.2 \text{ ms}$.

HEAT TRANSFER RATE BASED ON A SIMPLE CONDUCTION MODEL

$$q'' = \frac{2 k_H (T_H - T_C)}{\sqrt{\pi \alpha_H}} \left(\frac{\beta}{1 + \beta} \right) \sqrt{t_{\text{HT}}} \left(\frac{1}{t_{\text{HT}} + t_F} \right)$$

energy transferred in t_{HT} total cycle time where the Area for Heat Transfer is:

$$A(t) = \pi D_d^2 \left(1 + \frac{D_d}{D_F} (1 - e^{-t/t_F}) \right)$$

where $t_{\text{HT}} = 2D_d/c$

where c is the melt acoustic velocity

and $t_F = D_d/v_r$

where v_r is the relative growth velocity for Taylor instabilities

$$v_r \approx \sqrt{a \lambda_c}$$

$$D_F \approx \lambda_c = 2\pi \sqrt{\frac{\sigma}{a \Delta \rho}}$$

$$\beta = \sqrt{\frac{k_c \rho_c c_c}{k_f \rho_f c_f}}$$

Figure 2-17. Simple Model for Heat Transfer Between Fuel and Coolant After Local Film Collapse

NELSON'S SMALL SCALE TESTS - FeO_{1.3}

Test Conditions

$T_H = 2200 \text{ K}$	$\Delta t_{\text{air}} = 66 \text{ ms}$	Peak Bubble Radius = 32 mm
$T_C = 300 \text{ K}$	$\Delta t_{\text{fb}} = 34 \text{ ms}$	Bubble Period = 3.5 ms
$D_d = 2.7 \text{ mm}$	$\Delta t_{\text{exp}} = 0.2 \text{ ms}$	

Cooldown in Air $\Delta t_{\text{air}} = 66 \text{ ms}$
Mainly due to radiation $\Delta T \approx 75^\circ\text{C}$

Cooldown in Water $\Delta t_{\text{fb}} = 34 \text{ ms}, 35^\circ\text{C}$
 $\Delta T \approx 35^\circ\text{C}$

Film boiling	$\delta \approx 0.3 \text{ mm}$
Film collapse for $P \approx 0.8 \text{ MPa @ } 20 \mu\text{s}$	$\delta_{\text{MIN}} \approx 2 \text{ m}$ $\Delta t_{\text{coll}} \approx 40 \mu\text{s}$

Explosion Stage

$T_I = 1750 \text{ K}$	$\tau_{\text{HT}} = 1 \mu\text{s}$
$P_I = 1000 \text{ MPa}$	$\tau_F = 20 \mu\text{s}$

If fuel solidification halts the heat transfer process, the whole event occurs in 40-100 μs .

MINIMUM ISENTROPIC WORK = 1.5 - 2. J
MINIMUM CONVERSION RATIO = 3%

Figure 2-18. Experiment 11-2-1 Results and Comparison With the Simple Model

Finally the work from the explosive can be estimated from underwater explosion analysis of Cole¹³ by knowing the bubble maximum radius and frequency. The result is given in Figure 2-18 and it corresponds to 3% of the total thermal energy content of the melt drop.

These new small-scale experiments afford a greater chance of analysis and understanding and the simple model presented suggests that the dominant fragmentation mechanism is heat-transfer related. More detailed work is planned next quarter.

2.6 Assessment of Containment Failure Capability

Steam explosions are of interest in hypothetical core melt accidents because they may provide a radiological transport path to the environment by containment failure due to a dynamic overpressure of missile generation. Therefore the final portion of this research work is to couple the experimentally observed interaction results with analyses to determine containment failure capability. The approach is based on four tasks:

- Assume a conservative upper bound on the coherent release of energy from triggering and propagation of the interaction and then assess various mechanisms by which the work energy may be dissipated during the coolant slug acceleration prior to reactor vessel head impact
- Determine the ways the reactor vessel may be failed and/or a missile be generated due to the impact of the coolant slug
- Perform order-of-magnitude analyses to assess mechanisms that may dissipate the missile energy in its flight toward the containment
- Use simple structural models or analyses to predict if containment failure could occur due to missile impact or dynamic overpressure.

2.6.1 Energy Dissipation Mechanisms Prior to Reactor Vessel Impact (M. L. Corradini 4441)

In the last quarterly, a simple model for heat transfer to the cold water and structure above the explosion interaction zone indicated for SRI tests that heat transfer can substantially reduce the slug kinetic energy at impact.¹¹ During this quarter the model was used to analyze one open-geometry test and parametrically analyze the expansion phase at full scale.

In the experiments performed by Buxton, the thermite mixture was poured into water (~850 kg) in a steel tank (Figure 2-19) and the

explosion usually occurred near the bottom. An analysis to determine the effect of heat transfer was done where the coolant slug kinetic energy exiting the steel tank was compared for isentropic and heat transfer conditions. The results are shown in Figure 2-20 where the coolant in the interaction zone is assumed to be nearly saturated water ($X_c \sim 0.04$) giving a mass of coolant of about 25 kg. The initial vapor explosion pressure was varied over the range of values seen in the open geometry tests. The results indicate that heat transfer significantly reduces the slug kinetic energy and gives mechanical-thermal conversion ratios very similar to those experimentally determined by Buxton ($\sim 1-2\%$). As another indication of the effect of heat transfer, one specific test (Test 43) was compared to the analytical model of the expansion (Figure 2-21). Here again the data of the transient pressure during the expansion matches quite well the analytical model when heat transfer is included.

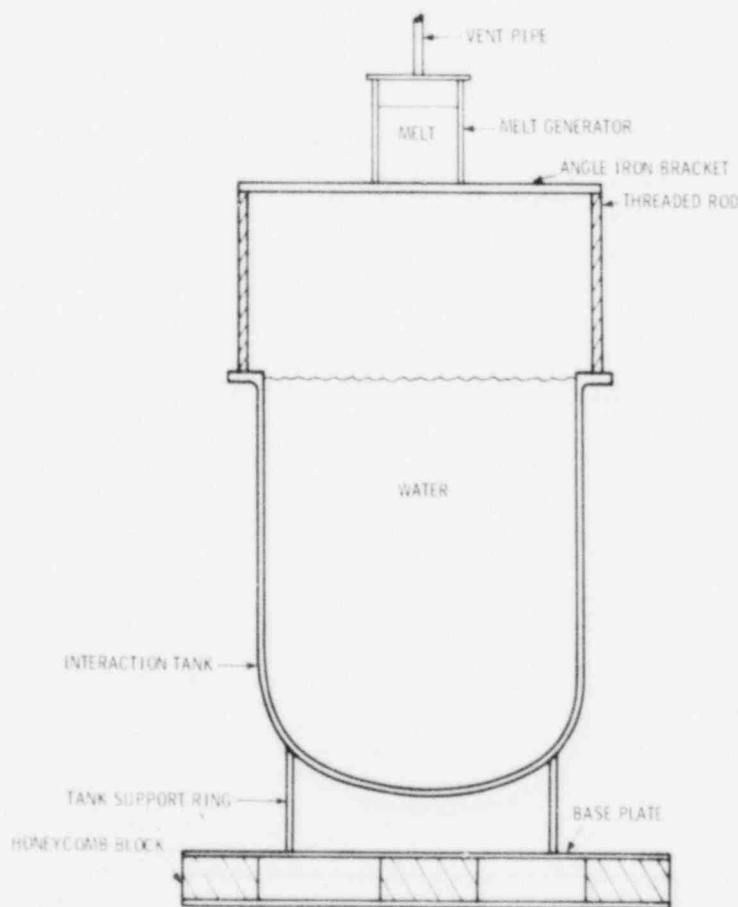


Figure 2-19. Artist's Conception of Interaction Vessel With Honeycomb Blocks and Melt Generator Installed

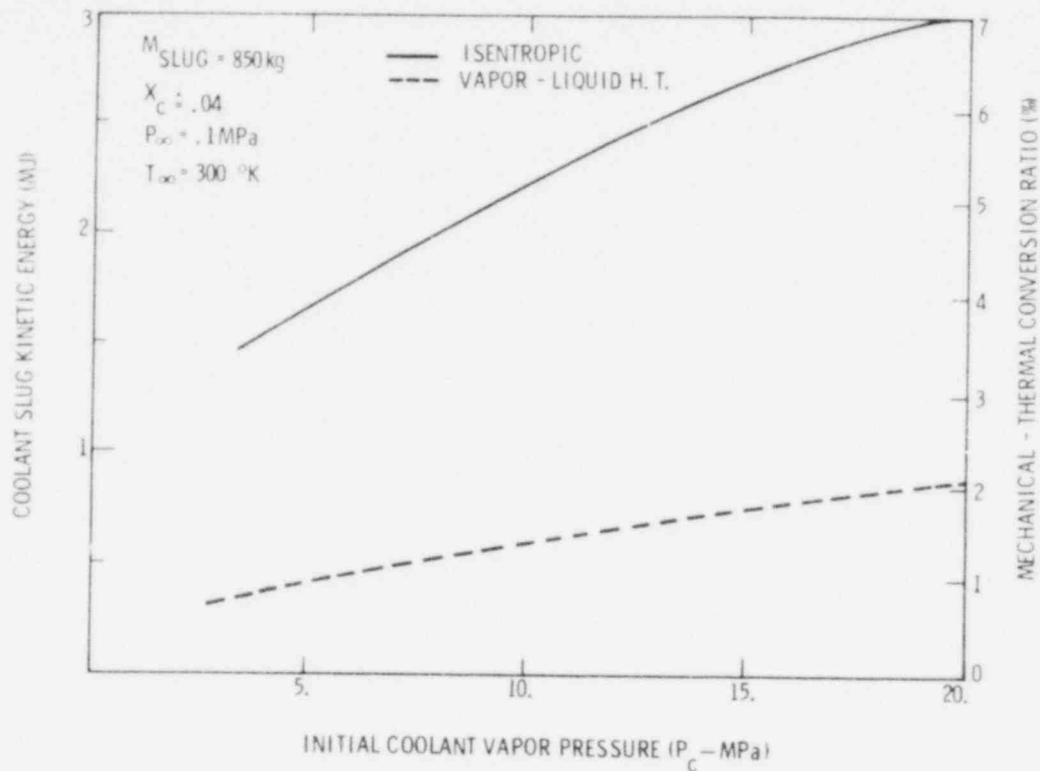


Figure 2-20. Slug Kinetic Energy as a Function of the Initial Coolant Vapor Pressure With and Without Heat Transfer

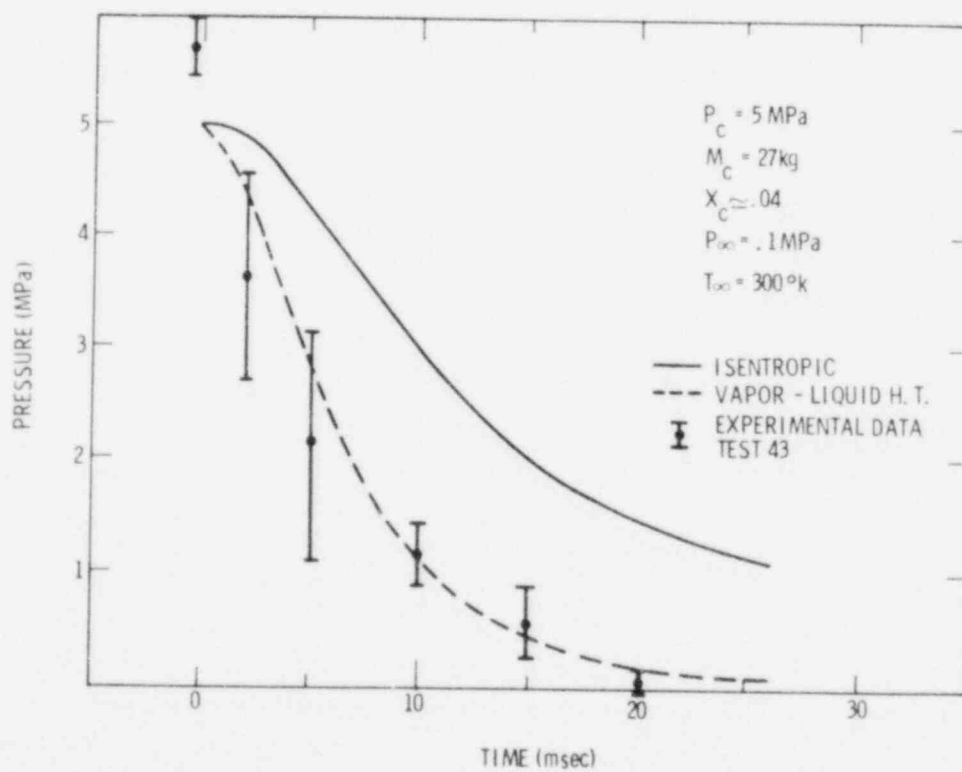


Figure 2-21. Transient Pressure Comparison of the Simple Expansion Model to Open Geometry Test No. 43 With and Without Heat Transfer

Parametric calculations of the full-scale expansion were also done where a simplified physical picture of the expansion is given in Figure 2-22. The hot two-phase coolant in the interaction zone accelerates the cold coolant above it and entrains some of the cold coolant transferring energy to it, thereby reducing the vapor pressure and the slug kinetic energy. For the full-scale hypothetical accident, the following initial conditions are not well known:

- The amount of coolant participating in the interaction, m_c
- The coolant vapor pressure after the propagation phase, p_c
- The cold coolant slug mass above the propagation interaction zone, M_{slug}

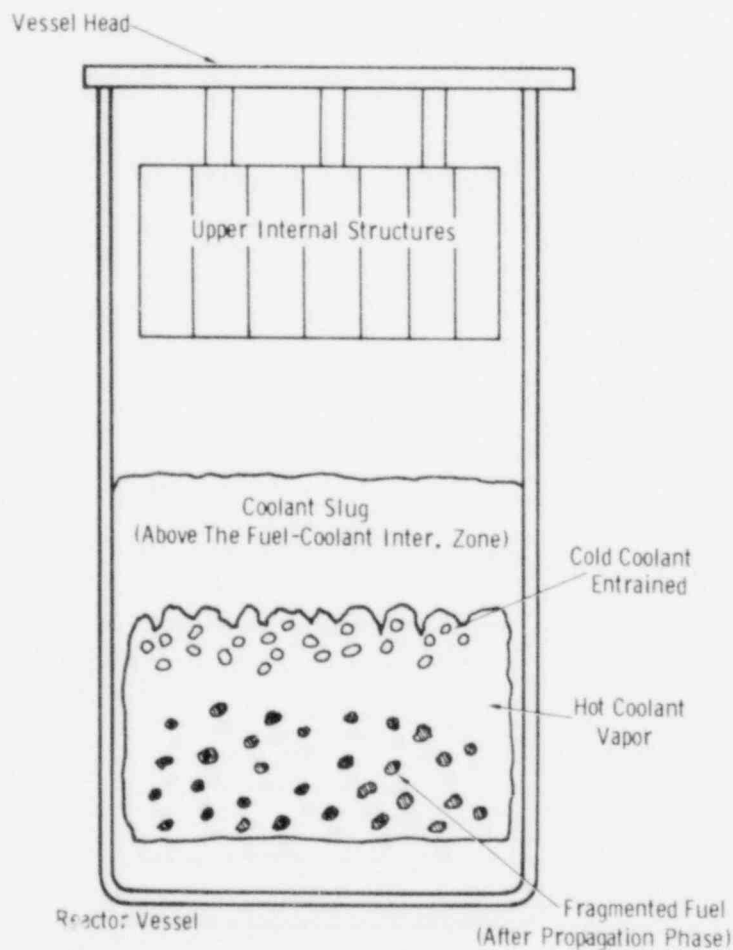


Figure 2-22. Idealized Schematic of the Vapor-Liquid Expansion After the Explosion

For the parametric analysis the range of values for these three are taken to be in the range,

$$1000 \text{ kg} < M_c < 16000 \text{ kg}$$

$$5 \text{ MPa} < P_c < 20 \text{ MPa}$$

$$14000 \text{ kg} < M_{\text{slug}} < 72000 \text{ kg}$$

The range on M_c is based on 5 to 100% of the water in the lower plenum, P_c , on the range of initial vapor pressures seen in Buxton's tests, and M_{slug} on the water height of 20% to 100% of the active core height. The results of the analysis are given in Figures 2-23 to 2-26. Figure 2-23 illustrates the significant effect of heat transfer in reducing the slug kinetic energy for one set of initial conditions as a function the expansion volume.

The final volume, $\Delta V \sim 120 \text{ m}^3$, corresponds to the slug entering the upper head region where upper internal structure may be present.

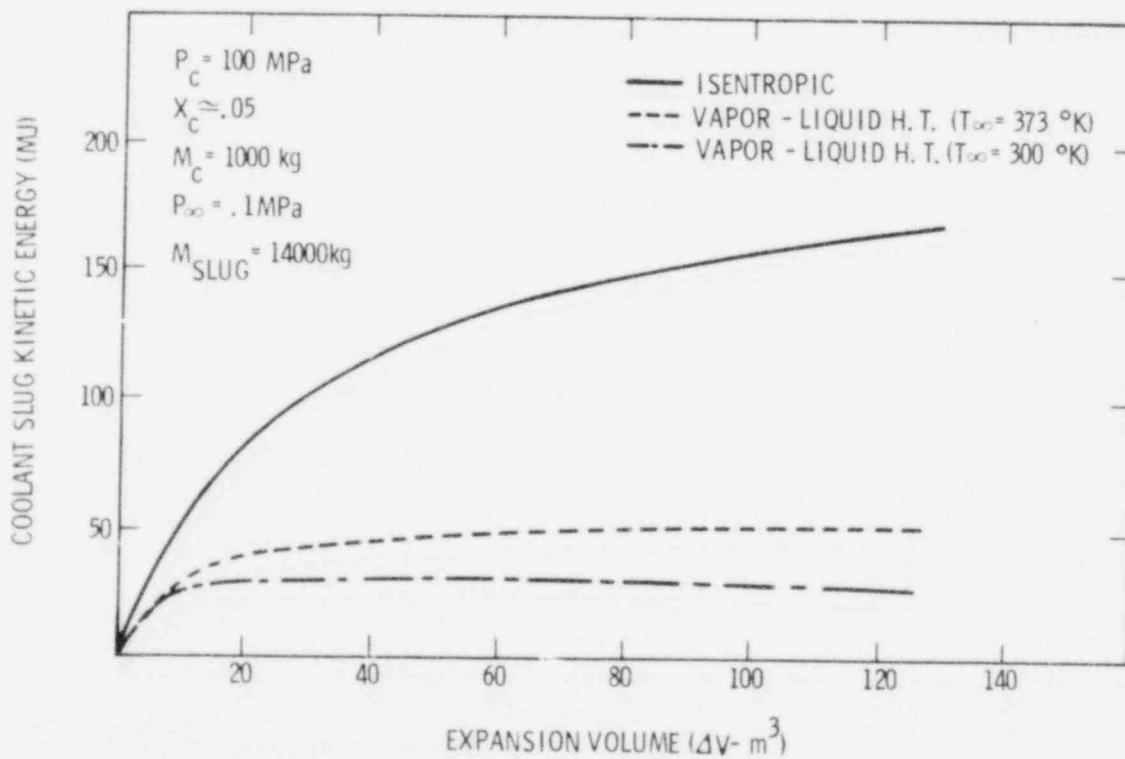


Figure 2-23. Full Scale Slug Kinetic Energy With and Without Heat Transfer

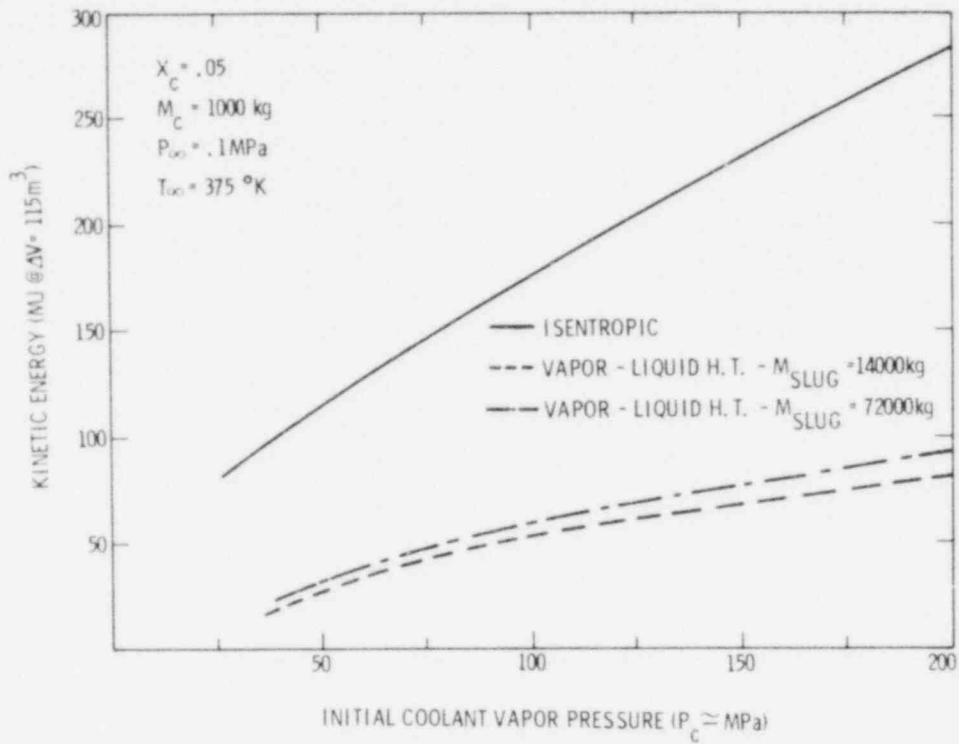


Figure 2-24. Full Scale Slug Kinetic Energy as a Function of the Coolant Vapor Pressure ($M_c \approx 1000 \text{ kg}$)

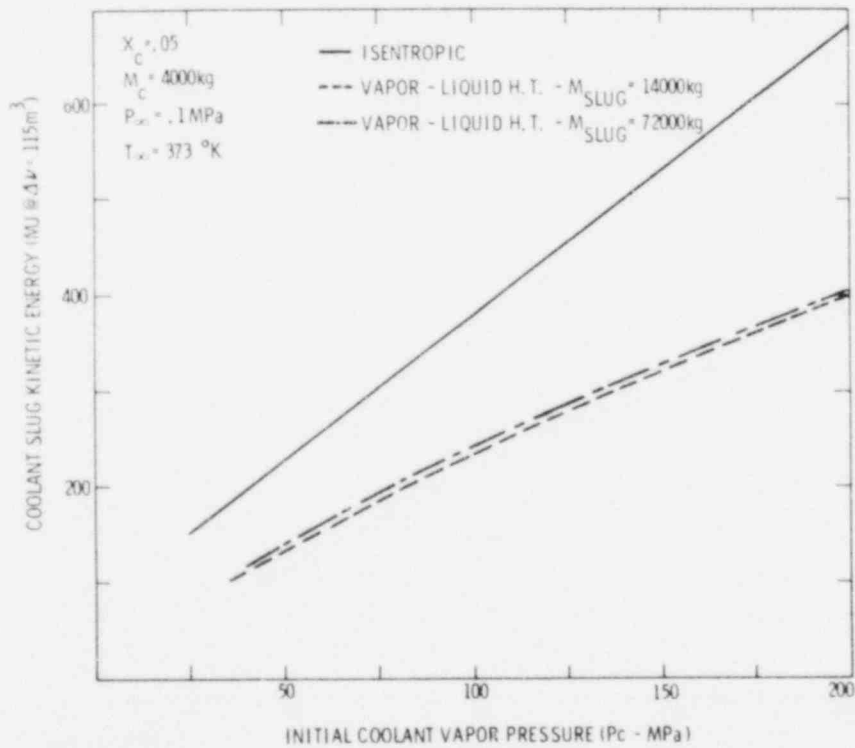


Figure 2-25. Full Scale Slug Kinetic Energy as a Function of the Coolant Vapor Pressure ($M_c \approx 4000 \text{ kg}$)

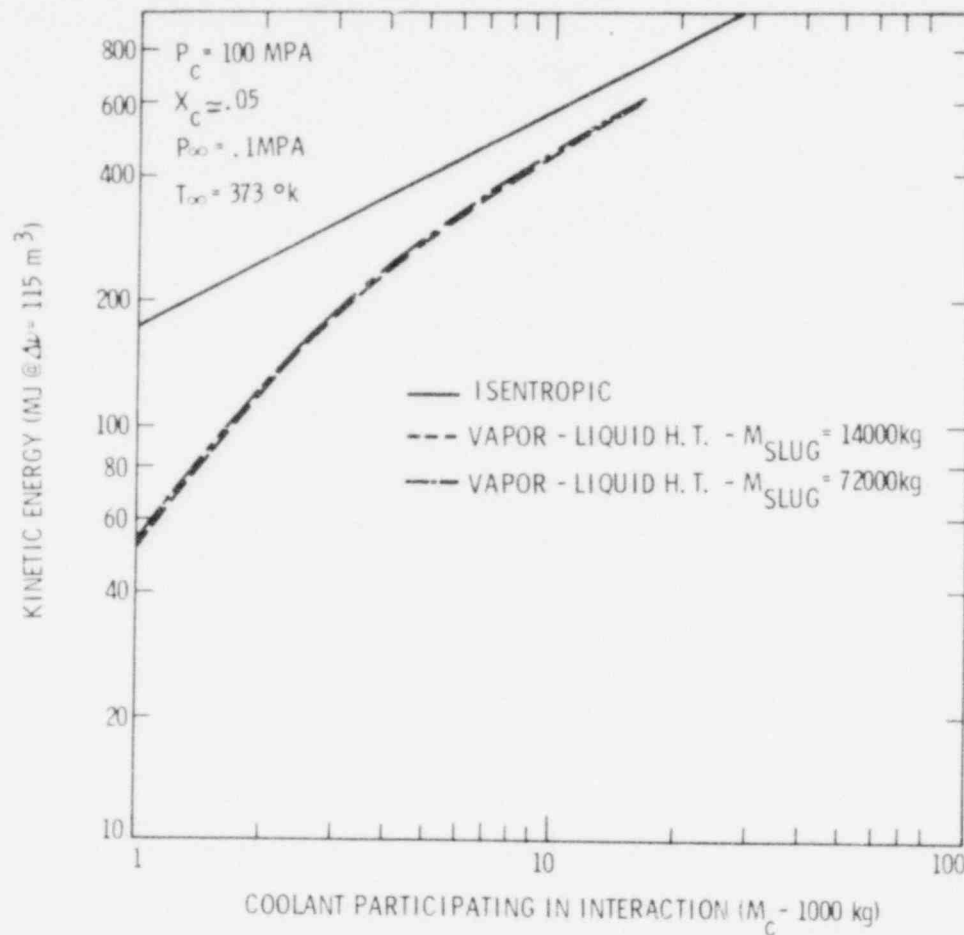


Figure 2-26. Full Scale Slug Kinetic Energy as a Function of the Coolant Mass

Figures 2-24 and 2-25 indicate the effect of the initial vapor pressure on the slug kinetic energy for two values of M_c and M_{slug} . Some observations can be made from these results:

- The slug mass does not appreciably affect the kinetic energy. This is due to two counter-balancing effects; as M_{slug} increases, the expansion time increases, allowing more heat transfer; at the same time the heat transfer area decreases, reducing the rate
- The percentage reduction in slug kinetic energy due to heat transfer given M_c is not drastically affected by varying P_c

The percentage reduction in slug kinetic energy is strongly dependent on the mass of coolant participating in the explosion; for $M_c \approx 1000$ kg, $K.E._{HT}/K.E._{ISEN} \approx 0.25$ while, for $M_c \approx 4000$ kg, $K.E._{HT}/K.E._{ISEN} \approx 0.5$. This effect is more graphically demonstrated in Figure 2-26 for a given value of P_c . Therefore the most crucial parameters that effect the slug kinetic energy prior to vessel impact are the amount of coolant participating in the interaction, M_c , and its initial pressure, P_c .

2.6.2 Reactor Vessel Failure Analysis (R. Woodfin 4442)

Preliminary analysis results of the reactor vessel in the early time have been obtained but no conclusions concerning failure mode are yet complete. The HONDO code is being used for some work, but it is expected that the bulk of the first set of conclusions will be based on energy balance analyses. These results will be available in the next quarterly report.

A first generation similarity analysis was conducted to investigate the feasibility of conducting a scale model experimental investigation. These results indicate that this would be reasonable and productive. Plans are being developed for this effort to be conducted in FY80.

2.6.3 Missile Energy Dissipation (R. Woodfin 4442)

There was no significant progress to report in this area.

2.6.4 Containment Failure Analysis (R. Woodfin 4442)

There was no significant progress to report in this area.

2.7 References

- ¹A. Inoue et al, Destablization of Film Boiling Due to the Arrival of a Pressure Shock P + I, Experimental, DOE-COO-2512-15 (Evanston, Illinois: Northwestern University, December 1978).
- ²T. G. Theofanous et al, "The Role of Hydrodynamic Fragmentation in Fuel-Coolant Interactions," 4th Specialist Meeting on FCIs, Bournemouth, Eng, Apr 1979. Proceedings to be published.
- ³P. D. Patel, "Hydrodynamic Fragmentation of Drops," (PhD Thesis, Purdue Univ, Dec 1978).
- ⁴H. P. Stephens, "Determination of the Enthalpy of Liquid Copper and Uranium With a Liquid Argon Calorimeter," High Temp Sci, 6:156-66 (1974).
- ⁵T. Nakamura, "Hydrogen Production from Water Using Solar Heat at High Temperatures," Solar Energy 19:467-75 (1977).
- ⁶D. A. Powers, Core Meltdown Experimental Review, SAND74-0382 (Albuquerque: Sandia Laboratories, 1975), Chap 4.
- ⁷L. S. Nelson et al, "The Combustion of Zirconium Droplets in Oxygen/Rare Gas Mixtures," High Temp Sci, 2:343-75 (1970).
- ⁸W. L. Doyle, J. B. Conway, and A. V. Grosse, "The Combustion of Zirconium in Oxygen," J Inorg Nucl Chem 6:138-44 (1958).
- ⁹L. S. Nelson and L. D. Buxton, Steam Explosion Triggering Phenomena. Part 2. Corium-A and Corium-E Simulants and Oxides of Iron and Cobalt Studies with a Floodable Arc Melter, SAND79-0260 (Albuquerque: Sandia Laboratories, 1979).
- ¹⁰L. D. Buxton and W. B. Benedick, Steam Explosion Efficiency Studies, SAND79-1399, (Albuquerque: Sandia Laboratories, 1979).
- ¹¹Light Water Reactor Safety Research Program Quarterly Report, October-December 1978, SAND79-0820 (Albuquerque: Sandia Laboratories, July 1979).
- ¹²Light Water Reactor Safety Research Program Quarterly Report, January-March 1979, SAND79-1542 (Albuquerque: Sandia Laboratories, Nov 1979).
- ¹³M. S. Kazimi, Massachusetts Institute of Technology, to M. L. Corradini, Sandia Laboratories, at Specialist's Meeting on Material Dynamics, Los Alamos, NM, Mar 1979.
- ¹⁴R. H. Cole, Underwater Explosions (Princeton, NJ: Princeton Univ Press, 1948).

3.0 Statistical LOCA Analysis (M. Berman, L. D. Buxton, R. K. Byers, G. P. Steck)

3.1 Summary

The primary task this quarter was preparation of the topical report (SAND79-1206) on the blowdown phase of the statistical study performed with RELAP4/MOD6. The draft report was completed and submitted to NRC and the Response Surface Review Group members for comment. A complete presentation of the results from this portion of the study was also given to the Review Group at the end of the quarter.

Other RELAP-related tasks addressed in the quarter involved: interpretation of the relative importance of the statistical variables as determined by response surface analysis; rechecking the nonreproducibility of code output problems sometimes encountered in the blowdown study; and slightly extending the study to investigate the effect of loss of power to the primary coolant pumps and the effect of larger critical heat flux. These tasks are discussed in Section 3.2.

Minimal progress was made on initiation of the statistical LOCA analysis with the TRAC code. A small part of a transient calculation was run. It is discussed in Section 3.3.

3.2 RELAP Blowdown Calculations and Statistical Analysis

This quarter, the PCT response surface models, developed during the study, were used in further investigations of the relative influence of various input variables. Recalculations to check the effect of the metal-water reaction yielded the same results as previously observed. A comparison of problems calculated at INEL and at Sandia showed no essential differences. Finally, calculations were made to assess the effect of critical heat flux and of loss of power to the primary coolant loop pumps. All calculations were performed with the Zion nodalization (Figure 3-1).

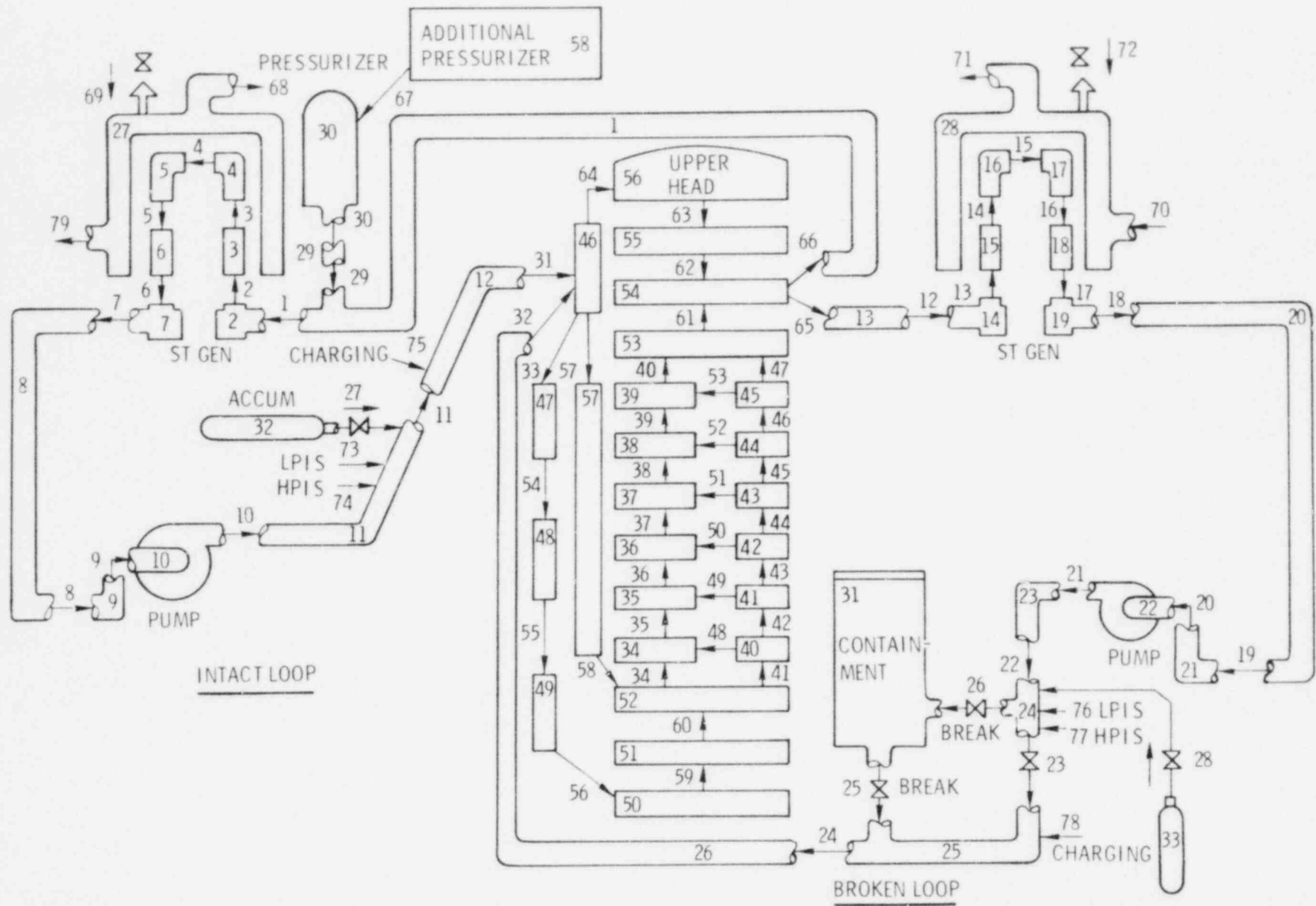


Figure 3-1. RELAP4 Nodalization for Statistical Study

3.2.1 Reproducibility of RELAP Results

It may be recalled from the previous quarterly report that we occasionally observed instances in which identical input sets did not result in identical output from RELAP4/MOD6 calculations. A great deal of effort and a large number of computer runs were devoted to an attempt to find the source of this problem. No conclusive evidence was found that RELAP was the source of the error. We concluded, without concrete proof, that sporadic computer system problems, either in the software or hardware, had caused the observed differences in output.

As a final check on our version of RELAP4/MOD6, a comparison was made between calculations run at Sandia and at INEL. All information necessary to repeat one of our calculations was sent to INEL, the calculation was performed there, and the resulting plot/restart tape sent to Sandia. When comparisons were made (to the limits of machine accuracy), we saw no differences in output that could not be attributed to differences between operating systems and computing environment. Our confidence in our version of RELAP4/MOD6 is thus reinforced.

We also performed recalculations of six runs which had been done when attempting to assess the effect of the metal-water reaction (MWR) parameters. For calculations yielding PCT below about 1900°F, the effect on PCT of varying MWR appeared to be physically inconsistent with the process being modelled, so those calculations were viewed as possible further instances of erroneous results. However, the recalculated results showed no differences from those obtained earlier. We, therefore, retain our previous conclusion that, at the lower temperatures, the effect of MWR is dominated by other artifacts of the calculations, such as timestep size during a particular run.

3.2.2 Critical Heat Flux Sensitivity Calculation

One of the calculations performed during the quarter was a so-called "star-point" run for a further check on PCT sensitivity to critical heat flux (CHF). We had previously performed this comparison for nominal

and low (0.3 times nominal) values of CHF; the current calculation uses the high CHF value of 3.0 times nominal.

As was observed in the previous comparisons, CHF seems to have little effect on PCT. Figures 3-2 through 3-4, showing surface temperatures for three of the hot pin slabs, are representative of the effects of varying the CHF multiplier. The most significant effect is seen (Figure 3-2) on post-PCT behavior. In our previous comparison, changing the CHF multiplier from 0.3 to 1.0 resulted in a PCT decrease of about 40°F; here, the change from 1.0 to 3.0 gives a further decrease of only about 13°F. Virtually no differences were observed in fuel-stored energy (Figure 3-5), or such measures of hydraulic behavior as break flow, intact loop accumulator flow, or core flows (Figures 3-6 through 3-8).

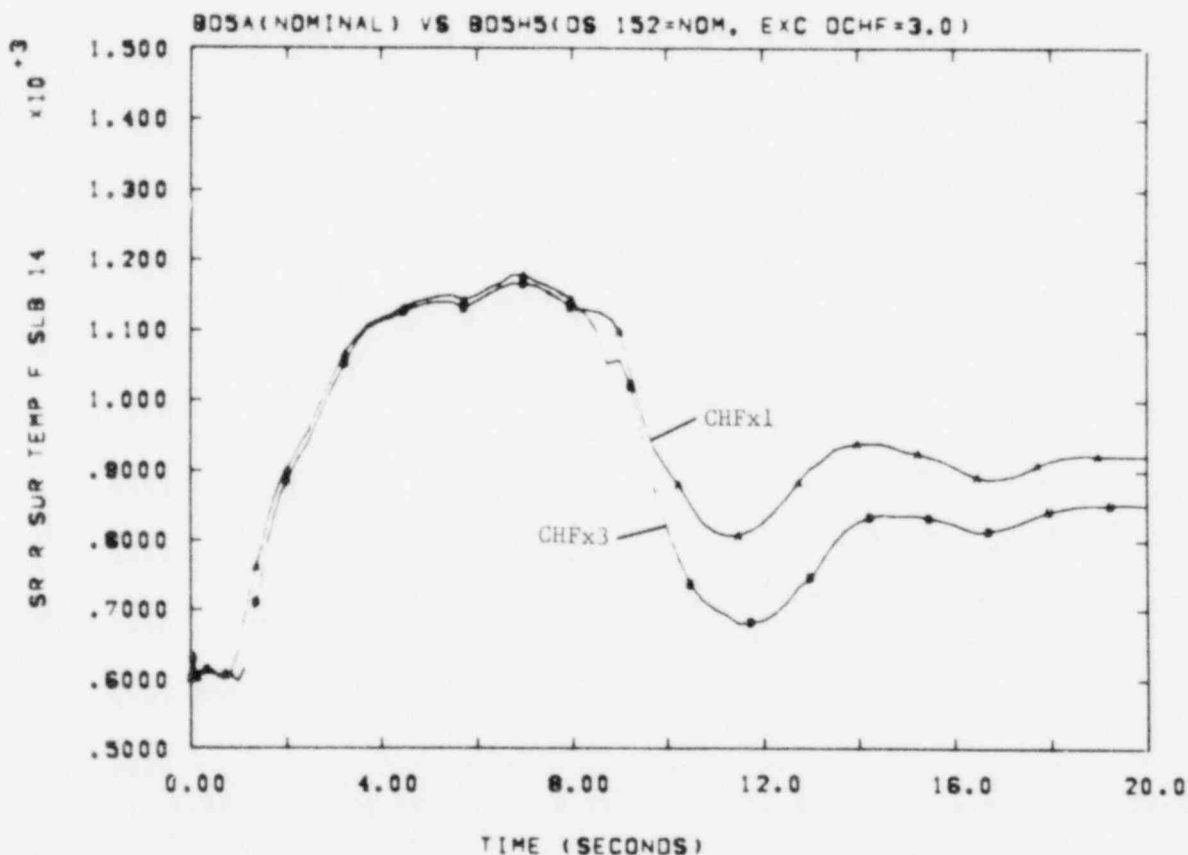


Figure 3-2. Surface Temperature, Slab 14; Effect of CHF Multiplier

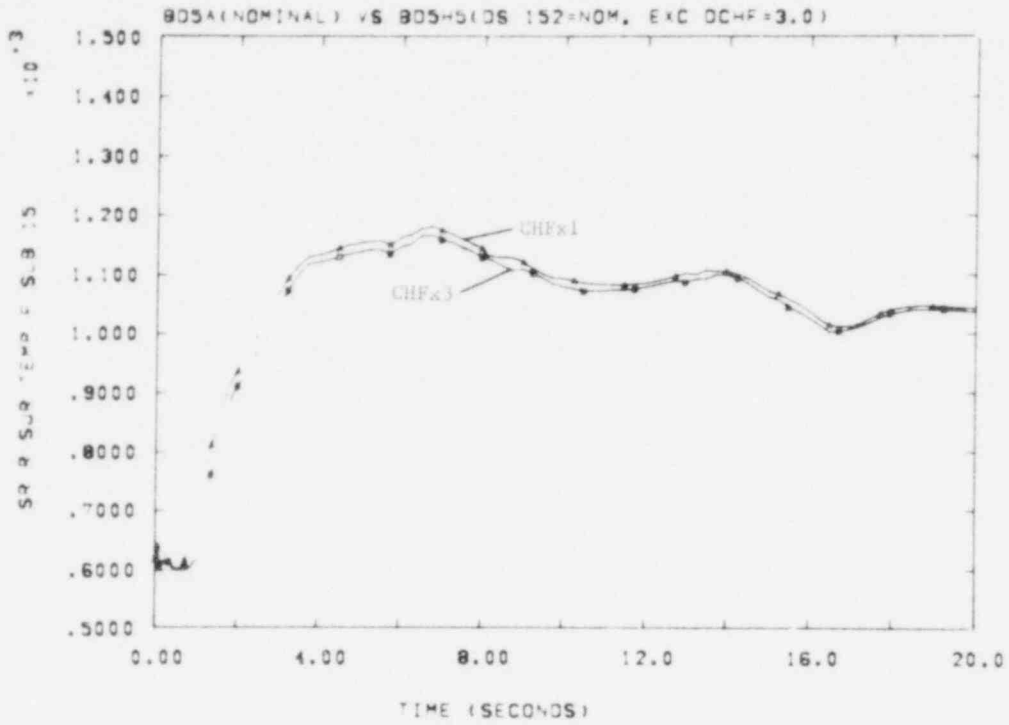


Figure 3-3. Surface Temperature, Slab 15; Effect of CHF Multiplier

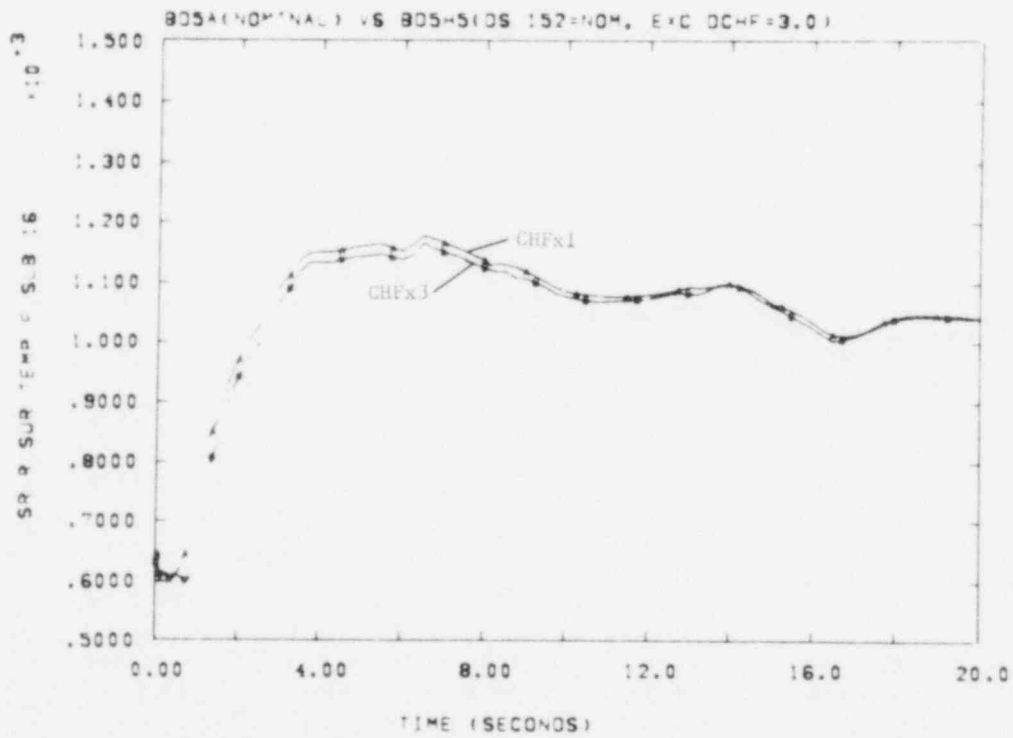


Figure 3-4. Surface Temperature, Slab 16; Effect of CHF Multiplier

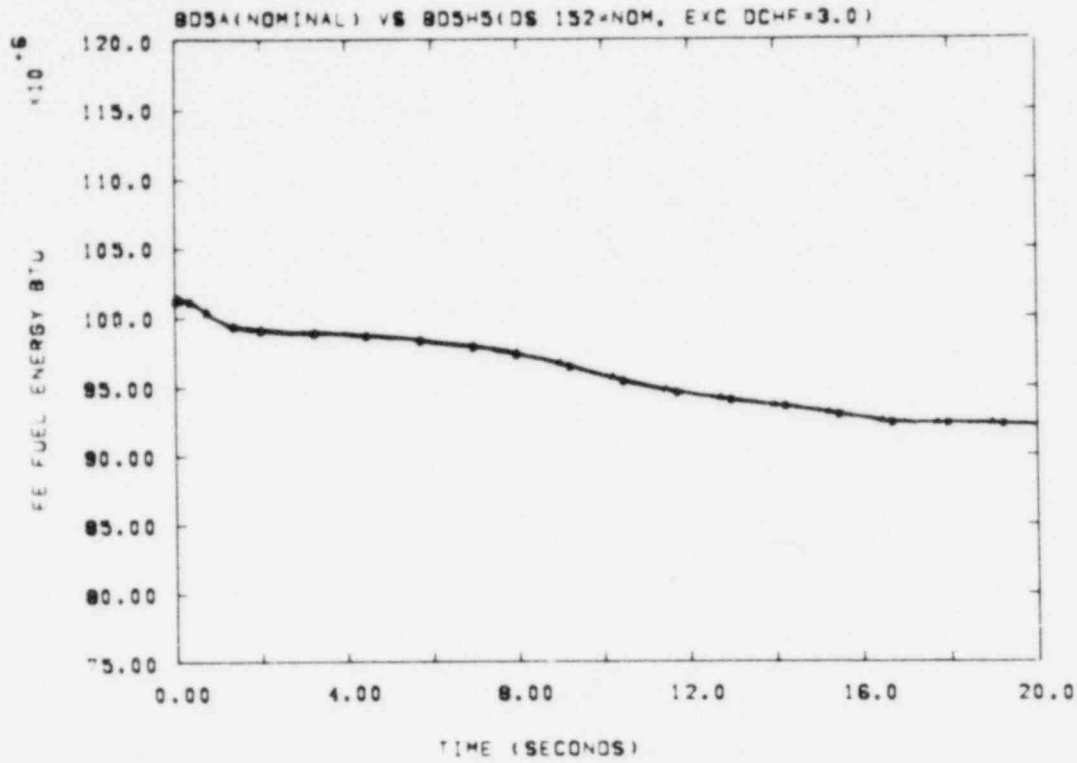


Figure 3-5. Fuel Stored Energy; CHF_{x3} and CHF_{x1}

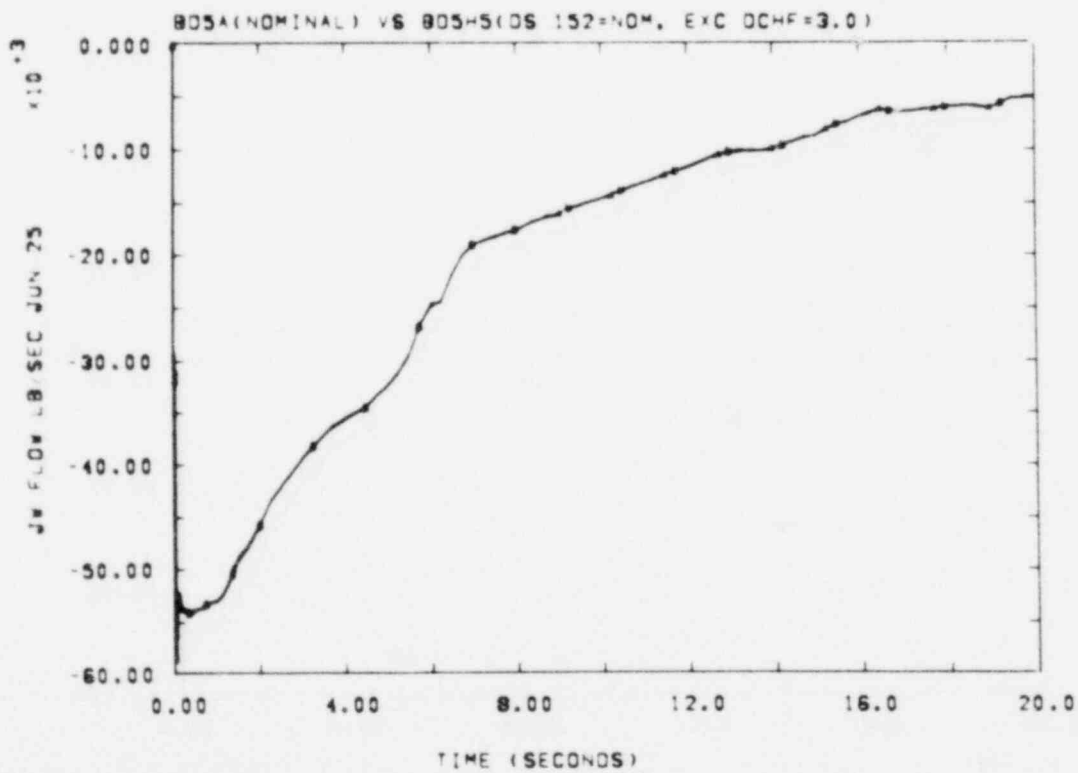


Figure 3-6. Pump Side Break Flow; CHF_{x3} and CHF_{x1}

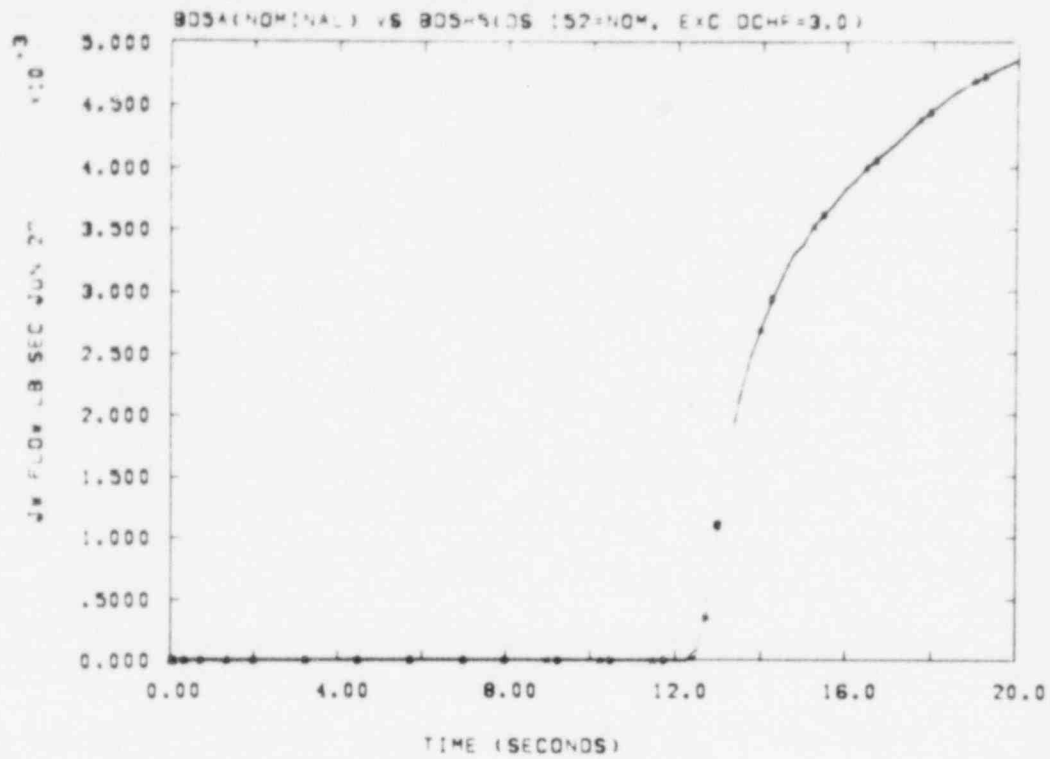


Figure 3-7. Intact Loop Accumulator Flow; CHF_{x3} and CHF_{x1}

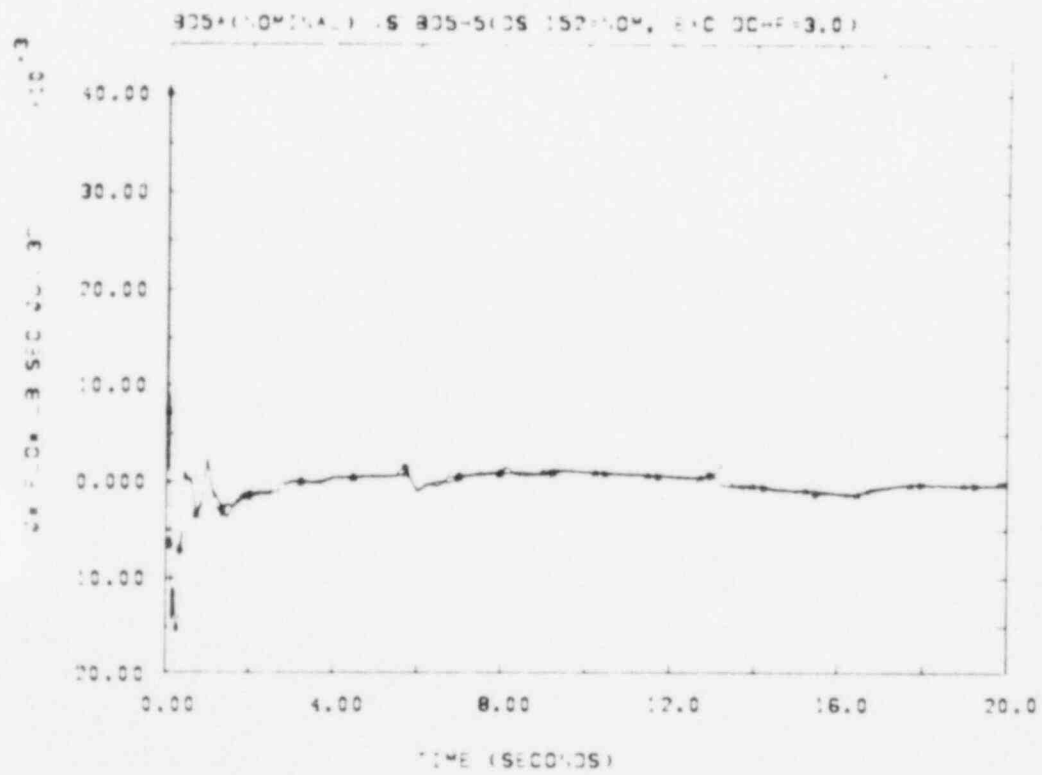


Figure 3-8. Flow at Midplane of Average Core; CHF_{x3} and CHF_{x1}

3.2.3 Calculation with Loss of Pump Power

Another blowdown calculation performed during the quarter was intended to simulate the effects of loss of electrical power to the primary coolant loop pumps. The ZION nodalization (Figure 3-1) was again employed, and the pumps were assumed to lose power simultaneously with break initiation. During the course of preparing for this calculation, we discovered and corrected a minor error in the pump torque-speed specification. The point in error was outside the normal operating range for our usual blowdown calculations (with pump power on), so it could have no effect on previous calculations in the study. In the following, we denote the nominal calculation as BD5A; BD5PMP is the same problem except that the pumps have no electrical power.

Comparison of results from BD5A and BD5PMP showed differences in pump behavior that appear quite reasonable. For the intact loop (IL) pump, torque and head (Figures 3-9 and 3-11, respectively) drop more rapidly (after the initial brief transient) with no motor power. The same effect on the magnitudes of torque and head (Figures 3-10 and 3-12) is seen at the broken loop (BL) pump. Note that during most of the blowdown, the IL pump continues to force fluid through the loop.

Flows at the IL pump outlet junction also show differences attributable to the presence or absence of pump power (Figure 3-13). With power on, coolant flow, after the initial rapid decrease, is roughly maintained for about 5 s, while in BD5PMP the flow decreases at a faster rate. The IL pump outlet flows, however, show virtually no differences (Figure 3-14). The reason for this is that break flows are choked throughout both calculations, and flows between the pump and the break are choked for about the first half of the transient.

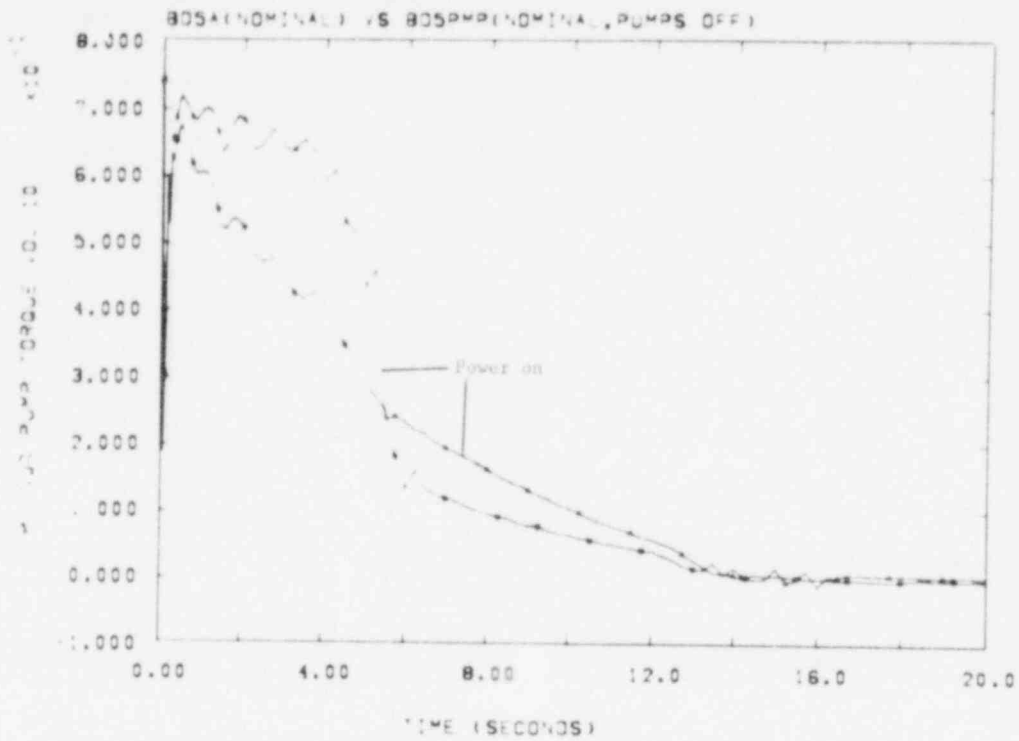


Figure 3-9. Intact Loop Pump Torque; Effect of Loss of Pump Power

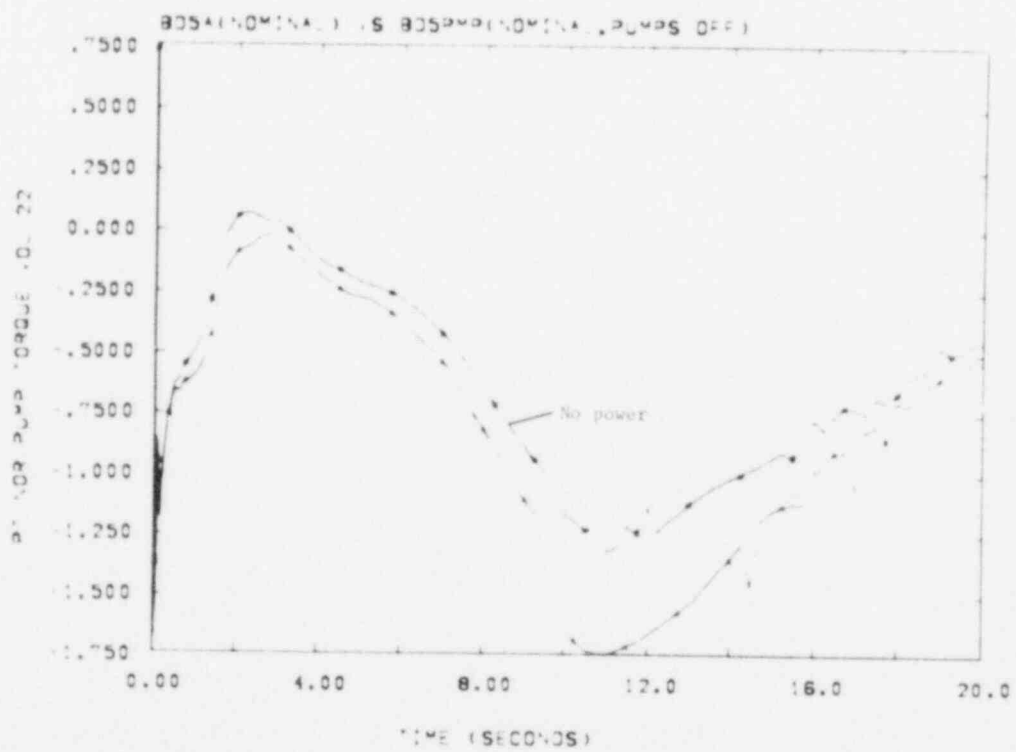


Figure 3-10. Broken Loop Pump Torque; Effect of Loss of Pump Power

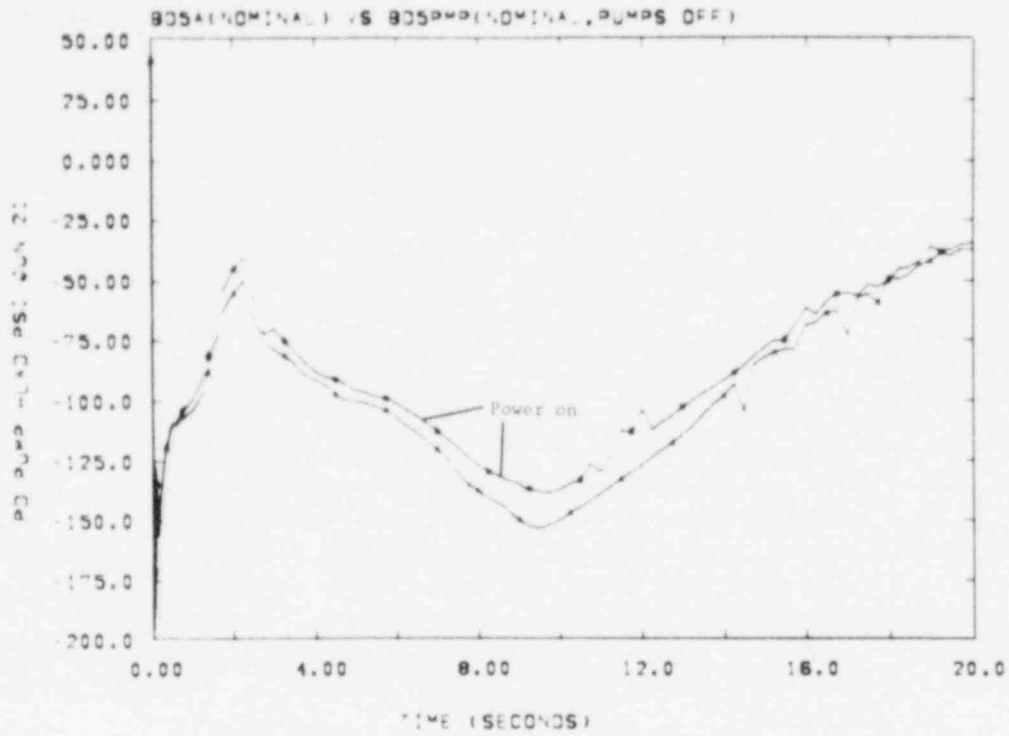


Figure 3-11. Intact Loop Pump Head; Effect of Loss of Pump Power

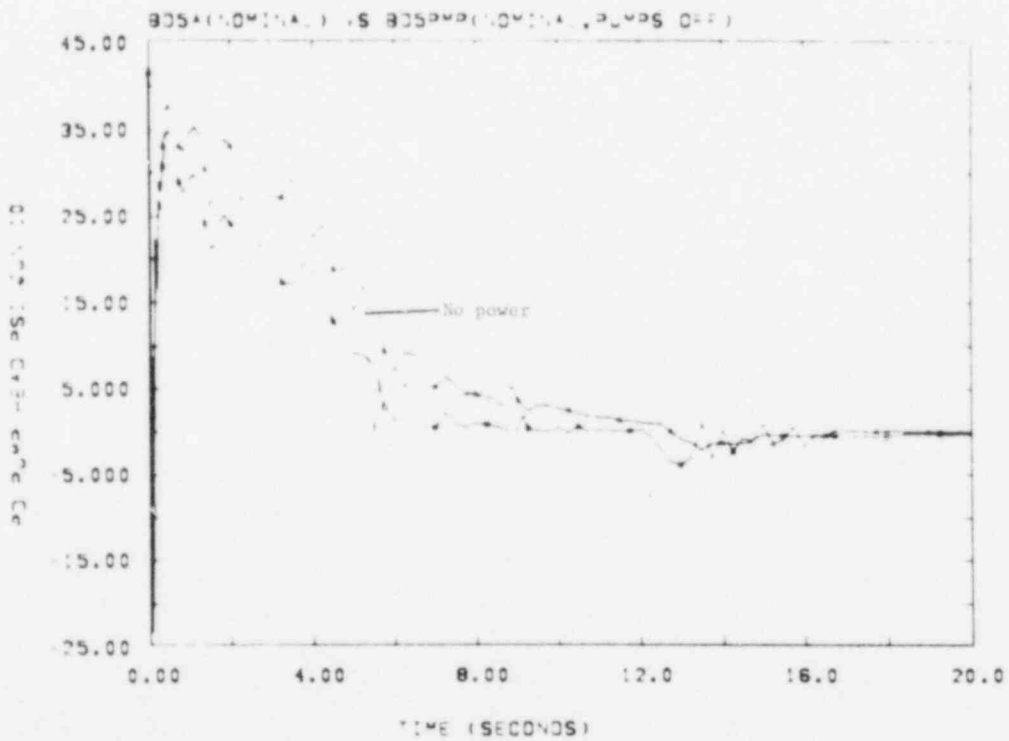


Figure 3-12. Broken Loop Pump Head; Effect of Loss of Pump Power

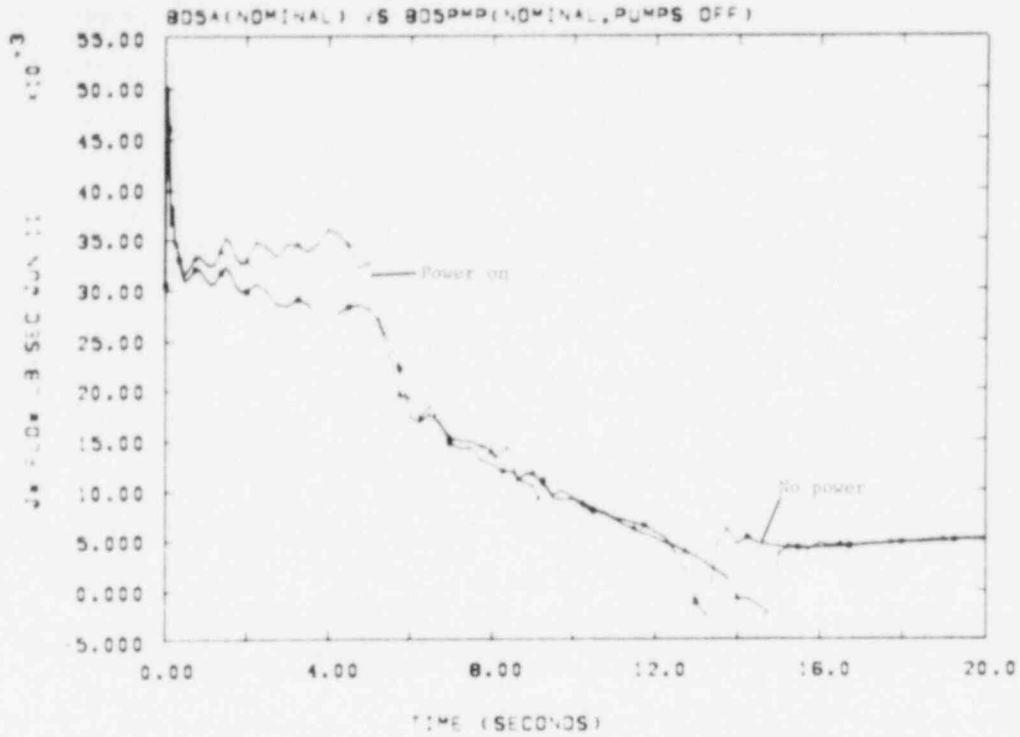


Figure 3-13. Intact Loop Pump Outlet Flow; Effect of Loss of Pump Power

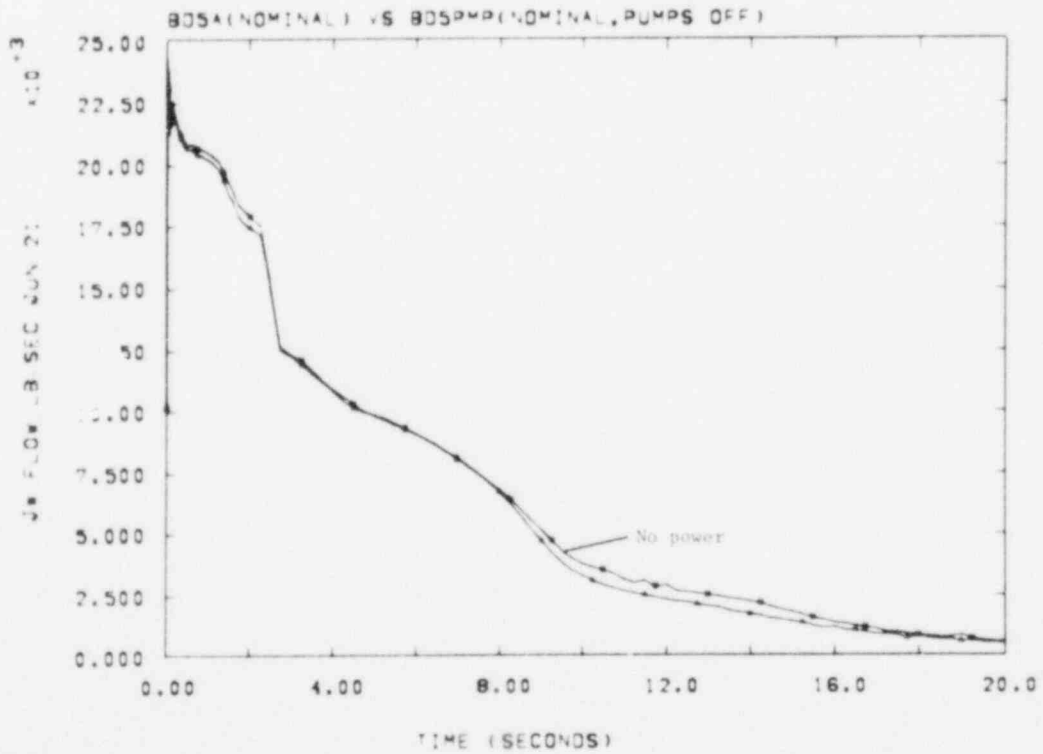


Figure 3-14. Broken Loop Pump Outlet Flow; Effect of Loss of Pump Power

Core upflow occurs to a larger extent in the BD5A calculation (Figure 3-15). Although core volume quantities are frequently higher for BD5A (Figure 3-16), the increased flow compensated sufficiently to improve the heat transfer; BD5A shows lower slab surface temperatures (Figure 3-17) and occasionally higher coolant temperatures (Figure 3-18) in the core. BD5A had a PCT of 1183°F at about 6.6 s; corresponding figures for a BD5PMP are 1273°F and 11.3 s.

Finally, we examine the effects of pump motor power loss on pump speed, as seen in Figures 3-19 and 3-20. Both pumps stay within normal operating range when the power is maintained. With power off, the IL pump speed (Figure 3-19) decreases, then levels off at about the time the rate of reduction in pump torque and head diminishes (Figures 3-9 and 3-11). Because of the lack of motor power, the BL pump speeds up and is still doing so at the end of the calculation (Figure 3-20).

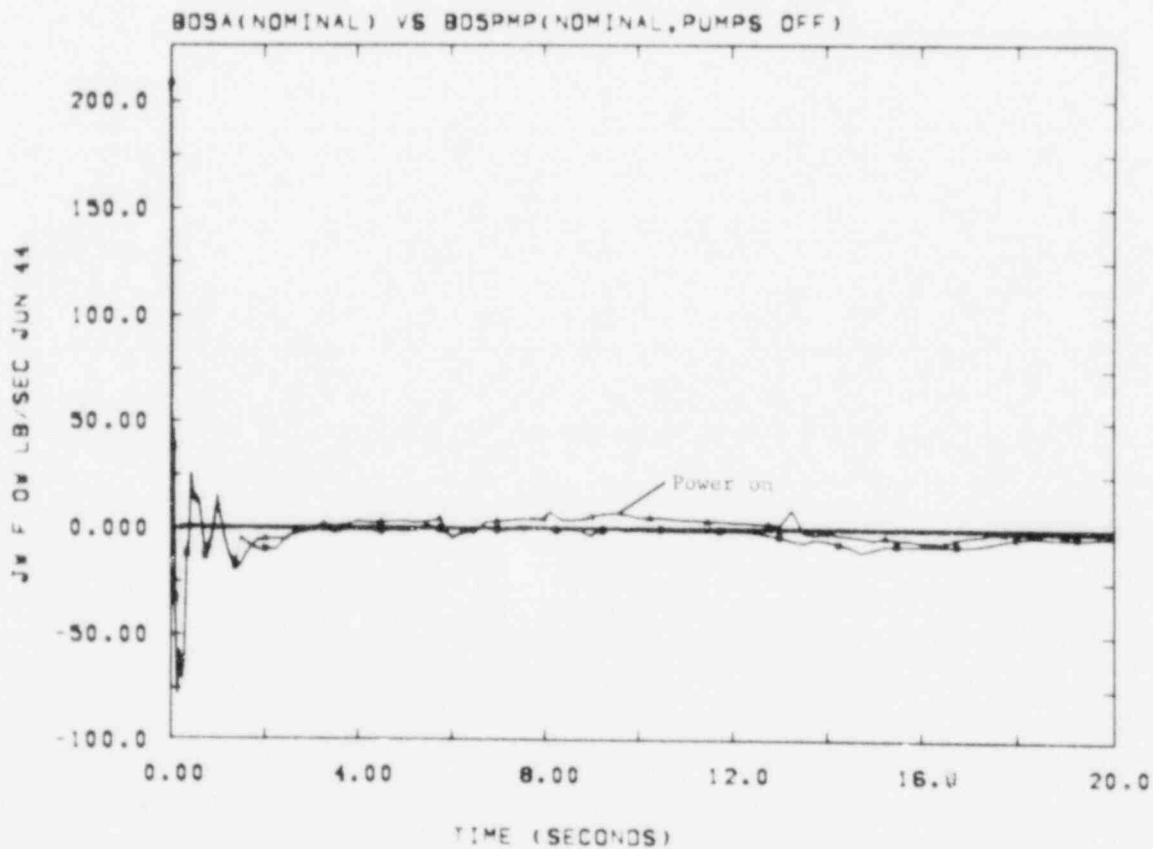


Figure 3-15. Flow at Midplane of Hot Channel; Effect of Loss of Pump Power

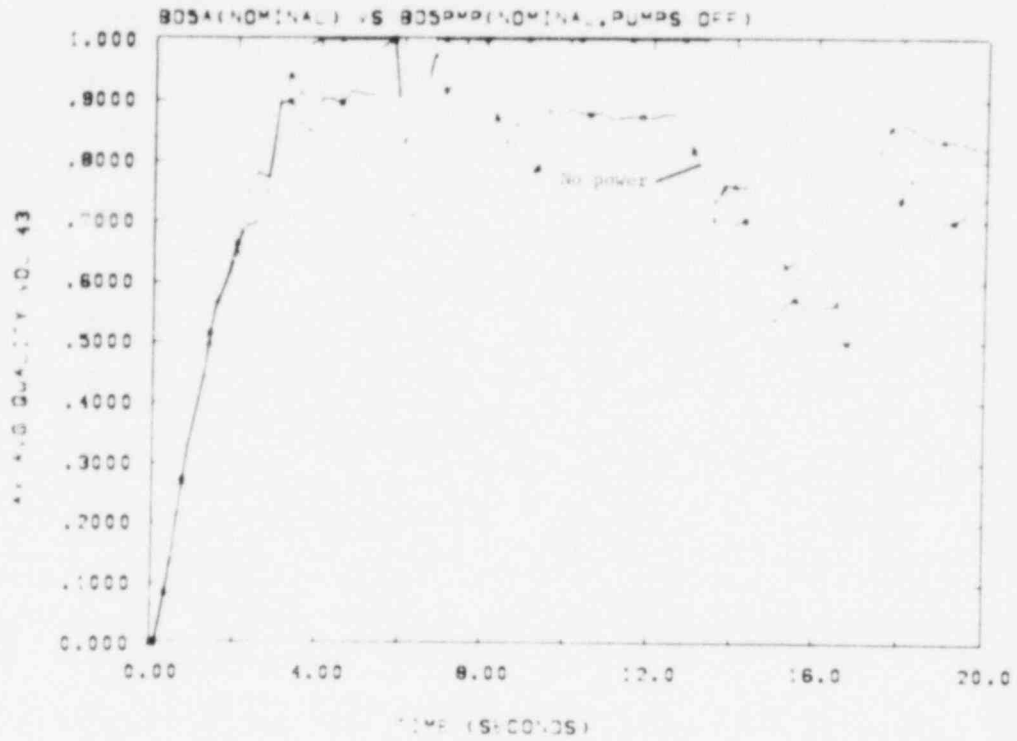


Figure 3-16. Quality of Midplane of Hot Channel; Effect of Loss of Pump Power

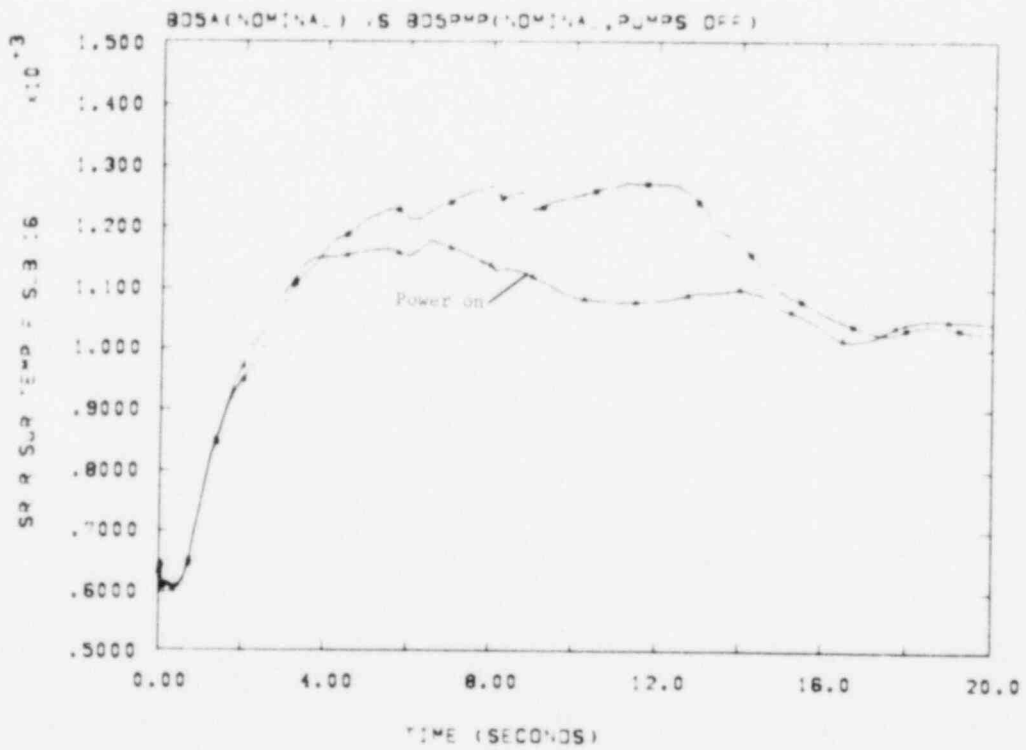


Figure 3-17. Surface Temperature, Slab 16; Effect of Loss of Pump Power

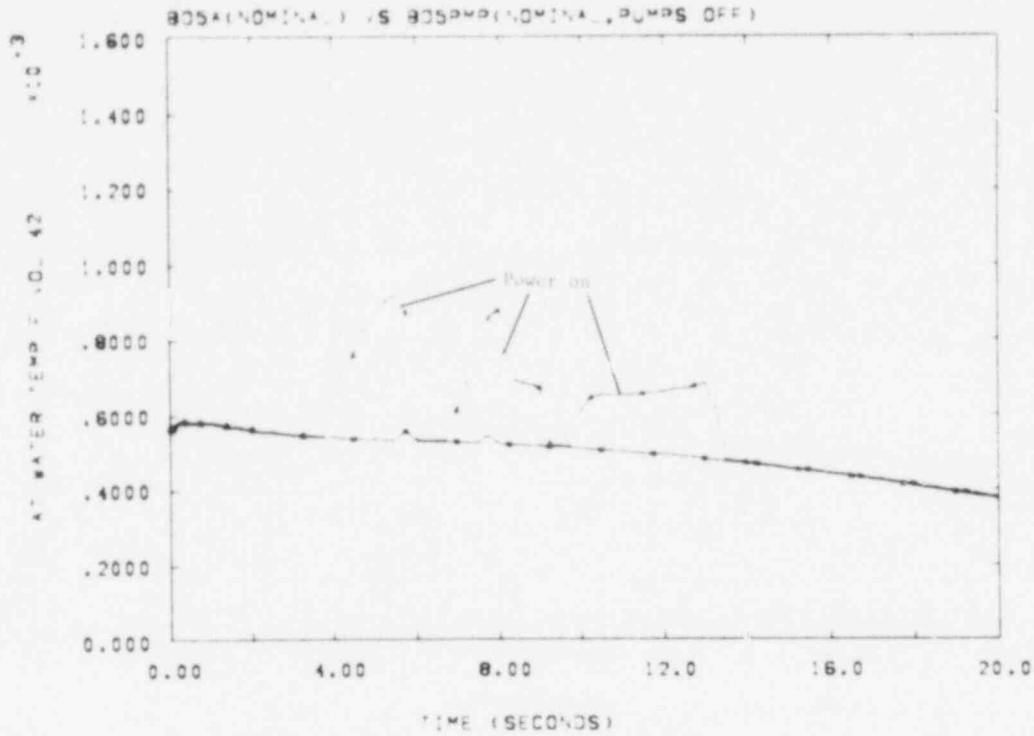


Figure 3-18. Volume Temperature in Hot Channel; Effect of Loss of Pump Power

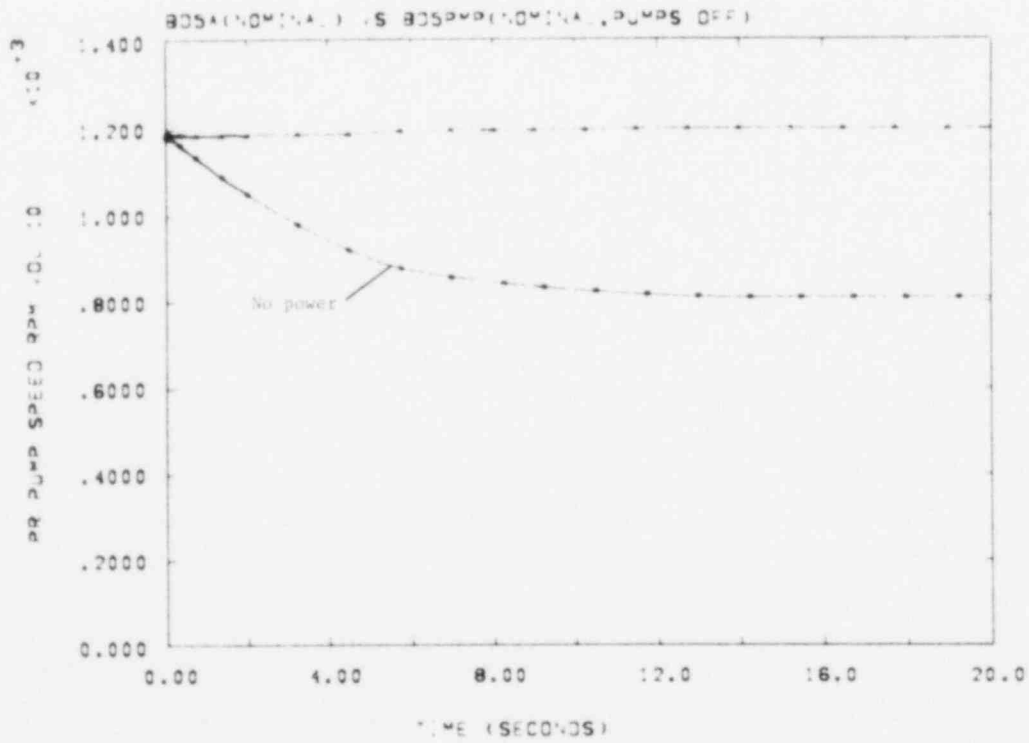


Figure 3-19. Intact Loop Pump Speed; Effect of Loss of Pump Power

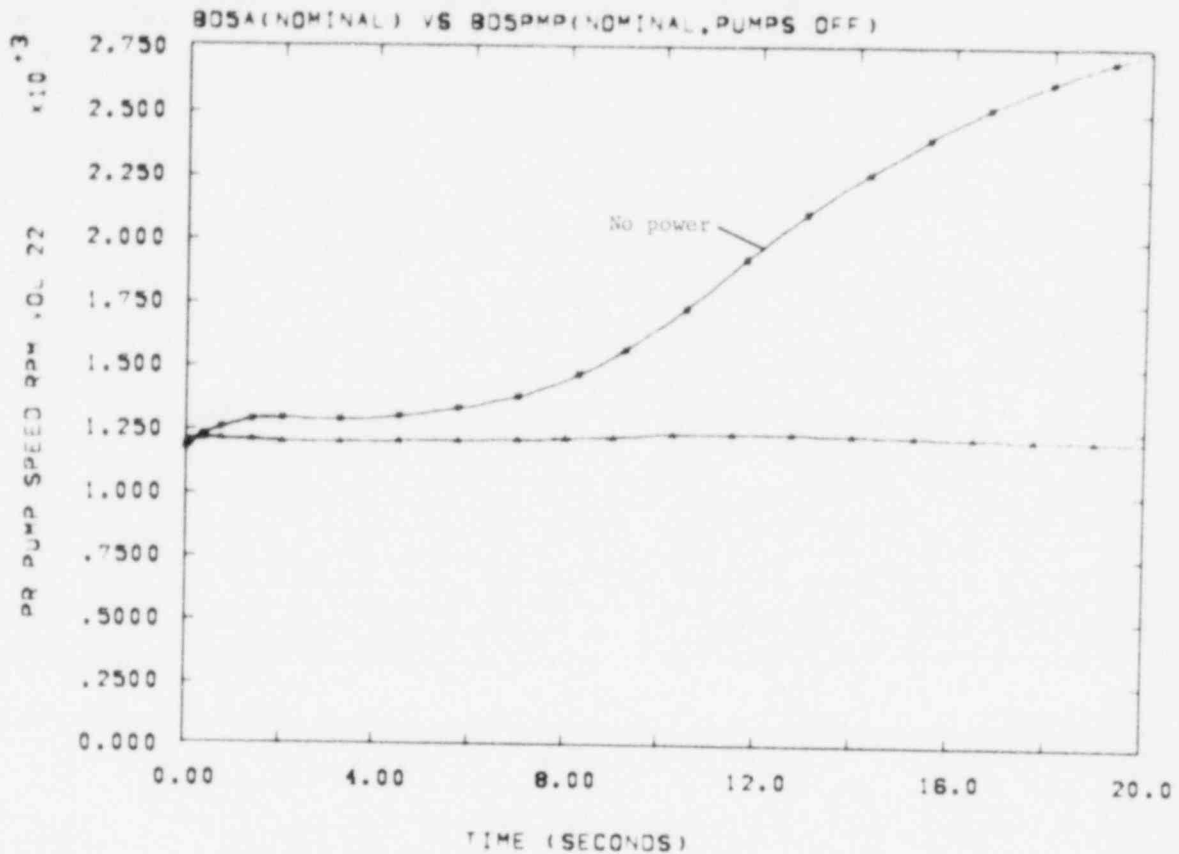


Figure 3-20. Broken Loop Pump Speed; Effect of Loss of Pump Power

3.2.4 Response Surface Results

In order to obtain further information on the behavior of our PCT response surface models, we have performed further analysis of the results from those models. We have also used the response surface to estimate relative importances of the statistical study variables when input conditions are other than nominal. In what follows, results are presented for a surface model with behavior that is fairly typical of all the twelve models developed in the study.

The statistical analysis of RELAP results showed that the variables with significant influence on PCT were slip, two-phase friction, Condie-Bengston heat transfer, power level, peaking factor, fuel thermal conductivity, and gap width. Table 3-I provides a list of these variables and various information about their types and values. In the table, the

notation "A" means the variable is an additive one; "M" indicates multiplicative. The entry F(T) denotes a variable whose value depends on time-in-life of the fuel; this quantity varied in the statistical study, but its effect is only seen indirectly, through tap width and peaking factor. Note also that, for these two variables, the values used in the base case RELAP calculation are different from those used in the midrange calculation.

Table 3-I

Seven Most Important Variables

Variable K	Name	Type	Nominal	Base Case	Midrange	Range	STD Coeff	
							A(K)	B(K)
3	Slip	A	0.0	1.0*	1.0*	0.3-3.0*	0.00033	0.66234
4	Friction	M	1.0	1.0	1.0	0.4-1.6	0.98985	0.41653
6	CB-HT	M	1.0	1.0	1.0	0.5-2.0	1.04941	0.41261
12	Power	M	1.0	1.0	1.0	0.94-1.06	1.00635	0.04159
18	PF	M	F(T) ⁺	1.575	1.782	1.24-2.32 ⁺	1.68059	0.26314
19	1/k	M	1.0	1.0	1.0	0.77-1.67	1.16475	0.31304
20	Gap	A	F(T) ⁺⁺	2.736 mils	2.825 mils	0.35-5.3 ⁺⁺	3.00084	1.19928

*Range and base case for DV = 1 + D * Slip for $\alpha < 0.8$

⁺PF: $1.48 \leq F(T) \leq 2.0$, $+3\sigma = +16\%$

⁺⁺Gap: $1.85 \leq F(T) \leq 3.8$ mils, $+3\sigma = +1.5$ mils

Table 3-II describes the model, CG-11, that we have chosen to exemplify response surface behavior. The PCT distribution referred to is the result of 10,000 samples of this surface. Regression calculations lead to equations for PCT in terms of the input variables; these result in estimates for PCT values and sensitivities.

Table 3-II

Response Surface CG-11

$$\begin{aligned} \text{Log (PCT)} = & 7.188 - 0.02314 * Z(3) + 0.03041 * Z(4) \\ & -0.03324 * Z(6) + 0.02465 * Z(12) \\ & +0.08017 * Z(18) + 0.07163 * Z(19) \\ & +0.09211 * Z(20) - 0.02244 * Z(18)^2 \\ & -0.02811 * Z(19) * Z(20) + 0.01691 * Z(18)^2 * Z(20) \\ & -0.01459 * Z(20)^3 \end{aligned}$$

Standardized, Log, L" (Linear Terms First)

$$R^2 = 0.9350, \text{ RMSR} = 4.8\% (62.5^\circ\text{F})$$

$$Z(K) = [X(K) - A(K)]/B(K)$$

"Nominal" = 1290°F

Median of PCT Distribution = 1227 (1237)

90th Percentile of PCT Distribution = 1376 (1376)

99th Percent = 1493 (1466)

Numbers in parentheses are intercepts of regression equations. They may be considered as estimates of the mean, 90th and 99th percentiles.

By using the response surface model to calculate changes in PCT due to changes in the input variables in the vicinity of their nominal or midrange values, Table 3-III may be constructed. "Standardized Change" refers to a quantity, either above or below a variable's nominal value, that is calculated in different ways for variables A and M. For example, a variable A is one-third of the way between its nominal value and its upper or lower limit; for variables M, the natural logarithm of the variable is treated in this way. We see from the table that, because of differing variable ranges compared to nominal or midrange values, the relative importance ranking for absolute sensitivity can be quite different than when referred to fixed fractional changes from the nominal values. We also note, as expected from the surface description, that significant nonlinearities occur only for variables 18 and 20 (peaking factor and gap width).

Table 3-III

Relative Importance of Input Variables to PCT
Surface for CG-11 Model

Variable	$^{\circ}\text{F}/\sigma$		$^{\circ}\text{F}/1\%$		$^{\circ}\text{F}/1\%$ Based on Δ	
	At X^-	At X^+	At 0.99 N	At 1.01 N	Δ^-	Δ^+
3 Slip	15	-15	0.6*	-0.2*	0.5*	-0.2*
4 Friction	-25	16	-0.9	0.9	-1.0	0.9
6 CB-HT	22	-27	1.0	-1.0	1.1	-1.0
12 Power	-16	15	-7.6	7.7	-7.8	7.7
18 PF	-77	37	-5.5	5.2	-6.8	4.0
19 $1/k$	-26	59	-3.1	3.1	-3.1	3.2
20 Gap	-83	98	-3.3	3.3	-2.8 (100) ⁺	3.4 (119) ⁺

$\Delta \equiv$ Standardized change

N \equiv Midrange

* A $+1\sigma$ change of slip yields a 67% change in DV

A -1σ change of slip yields a 33% change in DV

⁺ $^{\circ}\text{F}/\text{mil}$

We have also used the surface models to evaluate the influences of peaking factor (18) and gap width (20) when base case values were used instead of midrange. For variable 18, this amounts to a change of about 1 standardized change (Δ_{18}^-) from nominal; variable 20 is changed only about $0.1 \Delta_{20}^-$. The resulting PCT is 1201°F , comparing well with the RELAP value of 1183°F . (Midrange RELAP PCT was 1268°F compared to the response surface value of 1290°F .)

Tables 3-IV and 3-V compare the influences of the variables for the base case and midrange conditions, for 1σ and 1% variable changes, respectively. Again, as may be expected, the largest changes in sensitivity appear for peaking factor.

Table 3-IV

Influence of 1σ Parameter Variations ($^{\circ}\text{F}$)
(CG-11 Response Surface)

Variable	Base Case (PCT = 1201 $^{\circ}\text{F}$)		Midrange Case (PCT = 1290 $^{\circ}\text{F}$)	
	ΔT^-	ΔT^+	ΔT^-	ΔT^+
3 Slip	14	-14	15	-15
4 Friction	-23	15	-25	16
6 CB-HT	20	-25	22	-27
12 Power	-14	14	-16	15
13 PF	-61	81	-77	37
19 $1/k$	-25	57	-26	59
20 Gap	-73	95	-83	98

Table 3-V

Influence of 1% Parameter Variations ($^{\circ}\text{F}$)
(CG-11 Response Surface)

Variable	Base Case (PCT = 1201 $^{\circ}\text{F}$)		Midrange Case (PCT = 1290 $^{\circ}\text{F}$)	
	ΔT^-	ΔT^+	ΔT^-	ΔT^+
3 Slip	0.6	-0.2	0.6	-0.2
4 Friction	-0.9	0.9	-0.9	0.9
6 CB-HT	1.0	-1.0	1.0	-1.0
12 Power	-7.1	7.1	-7.6	7.7
18 PF	-7.4	7.2	-5.5	5.2
19 $1/k$	-3.0	3.0	-3.1	3.1
20 Gap	-2.9	3.0	-3.3	3.3

Finally, we used the response surface model to evaluate PCT sensitivity for cases in which all variables are $\pm 1\sigma$ and $\pm 2\sigma$ away from nominal. Table 3-VI displays the results of those calculations, and shows the sometimes striking differences in relative importance that can occur when regions of the data spaced far from the most populous region are explored. In fact, the entries for gap width sensitivity, which are both positive,

with all variables at -2σ from nominal, should serve to emphasize the care that should be used in applying the response surface model results.

Table 3-VI

Influence of 1σ Parameter Variations ($^{\circ}\text{F}$) With Parameters at Off-Nominal Conditions (CG-11 Response Surface)

Variable	Midrange Case (PCT = 1290 $^{\circ}\text{F}$)		$+1\sigma$ (PCT = 1478 $^{\circ}\text{F}$)		-1σ (PCT = 1102 $^{\circ}\text{F}$)		$+2\sigma$ (PCT = 1659 $^{\circ}\text{F}$)		-2σ (PCT = 930 $^{\circ}\text{F}$)	
	ΔT^-	ΔT^+	ΔT^-	ΔT^+	ΔT^-	ΔT^+	ΔT^-	ΔT^+	ΔT^-	ΔT^+
3 Slip	15	-15	17	-17	13	-13	19	-19	11	-11
4 Friction	-25	16	-33	22	-15	10	-43	28	-10	6
6 CB-HT	22	-27	31	-38	15	-18	44	-54	10	-12
12 Power	-16	15	-18	18	-13	13	-21	20	-11	10
18 PF	-77	37	-78	46	-96	55	-112	93	-112	76
19 1/K	-26	59	-26	60	-25	59	-23	52	-24	55
20 Gap	-83	98	-102	74	-41	82	-91	9	9	52

3.3 Statistical LOCA Program - TRAC Progress

A very high priority was given by the NRC sponsors to the performance of TRAC calculations for the UHI Semiscale program again this quarter. Consequently, little was done on the redirection of the statistical LOCA program from using RELAP to using TRAC in order to allow continuous predictive capability from blowdown through reflood.

As mentioned in the last quarterly report,¹ TRAC-PIA was released in the latter part of March 1979 and it was used to run a steady-state calculation in preparation for calculating the system behavior following a 200% double-ended, guillotine break in the cold leg of a full-scale, four-loop, pressurized water reactor (PWR). The particular PWR nodalization used did not exactly correspond to the ZION I facility modelled in the RELAP portion of the statistical LOCA study, but the reactor vessel nodalization was for the ZION facility.

During this quarter, the transient portion of that LOCA calculation was begun with the release version of TRAC-PIA. That calculation was carried out to about 26 s of transient time. However, in the course of

supporting LASL on the Semiscale S-07-6 calculation (see Section 4.1), it was discovered that several corrections had been made by LASL to TRAC-PIA which might affect the predicted transient behavior. Therefore, the steady-state calculation was repeated incorporating these corrections (with no significant effect on the results) and the transient calculation was begun again. This time the calculation was carried out to about 37 s of transient time.

At that point, it was noticed that the core had temporarily filled with water far too early, starting at about 30 s. This incorrect behavior has been traced to a modelling assumption error. The vapor fraction of the containment boundary condition for the vessel side of the break was set to 0.0 at the start of the transient in order to keep the calculation from "seeing" an instantaneous jump in vapor fraction before the flow field turned around and flow started out the break. Unfortunately, alpha was never properly reset to 1.0 after the break flow started. During a break pipe flow reversal at about 30 s into the transient, this caused a huge slug of liquid to be sucked into the system instead of vapor.

No further calculations are planned with this particular nodalization since the nodalization will be modified to more closely resemble ZION in the exterior loops as well as the vessel during the next quarter. No comparisons of the TRAC blowdown prediction and the RELAP base case blowdown prediction have been made yet since the system modelled is not the same.

3.4 References

¹Light Water Reactor Safety Research Program Quarterly Report, January-March 1979, SAND79-1542 (Albuquerque: Sandia Laboratories, Nov 1979).

4. UHI Model Development (M. Bernan, L. D. Buxton, T. J. Bartel)

4.1 Summary

Upper head injection (UHI) describes a new emergency core cooling system developed by Westinghouse for pressurized water reactors (PWR) that use ice condenser containment systems. Analytic tools presently available for studying loss-of-coolant accidents (LOCA) are inadequate in treating several phenomena whose importance has increased with UHI. These phenomena include

- Two-phase flow with slip
- Occurrence of top quench in the core
- Upper head draining during refill

Sandia has embarked on a model development and testing program to improve the treatment of these phenomena in the RELAP4 and TRAC codes. Following are the results for this quarter.

We made considerable progress in the application of TRAC to Semiscale experiments. On-site assistance was provided to support LASL in its S-07-6 calculation. Sandia provided computer time, thermal-hydraulics, and programming assistance. In addition to this support, we generated a Semiscale MOD3 UHI nodalization based primarily on the engineering drawings of the system. The nodalization attempted to circumvent the 1-D drift flux problems in TRAC by incorporating much of the system into the vessel module. This permitted the use of the two-fluid equations for counter-current flow analysis in regions where this was expected to be important. Steady state calculations were performed and yielded results close to design predictions. Transient calculations, however, were stopped at about 18 s into the transient, apparently by numerical instabilities in the broken loop pump volumes.

We continued to analyze the reflood phase of a LOCA by utilizing a Westinghouse UHI geometry. The calculational procedure employs the FRAP-T4¹ fuel code to obtain a detailed core temperature profile at the beginning of reflood by utilizing hydraulic boundary conditions from a RELAP4/MOD5² blowdown calculation. Currently, 10 power regions are evaluated with the FRAP code. These results are used as input to RELAP4/MOD5-FLOOD to calculate core hydraulic conditions during reflood. Finally, TOODEE2³ will use these boundary conditions to determine a peak clad temperature (PCT) for reflood.

This quarter we concentrated on completing the carryout-rate-fraction (CRF) model and addressing several nodalization and system initialization concerns. The Westinghouse CRF model⁴ incorporated into flood has been slightly modified to produce a stable calculation. These modifications include several control criteria and the smoothing of a discontinuity. Calculations were made to determine the effect of core exit enthalpy and the inclusion of an intact loop accumulator model. A code error was discovered and corrected. This correction affected all junction flows where the FLOOD option was used in the RELAP4/MOD5 code.

4.2 TRAC Progress

4.2.1 Introduction

The high priority given by the NRC sponsors to Semiscale MOD3 calculations with TRAC continued through this quarter. Consequently, again this quarter a considerable amount of assistance was given to LASL for performing S-07-6 calculations. The emphasis in the new calculations was on a revised nodalization of the MOD3 vessel which incorporates the downcomer into the vessel module. This allows the two-fluid equations to be used for the downcomer instead of the drift flux equations. The primary intent of this change was to improve the code's predictive ability for counter-current flow in the downcomer.

Four new sets of S-07-6 calculations were performed this quarter, each with different variations on the special heat sources and heat slabs used in the downcomer and lower plenum regions. As discussed in the last quarterly report,⁵ Sandia did not have the primary responsibility for the S-07-6 calculations. Therefore, no discussion of the results will be given here; they will be reported independently by LASL. Sandia's contribution was to provide the required computing time and all assistance possible to expedite the calculations. It should be noted that specialized vessel graphics capabilities were developed by Sandia in the course of the calculations to help analyze the results since the normal graphics package provides no information on such factors as vessel flows and heat transfer.

In addition to the indirect work on Semiscale UHI modelling by supporting the LASL S-07-6 calculations, calculations directly applicable to the Semiscale Series 8 (UHI) were also begun. The basic MOD3 system nodalization developed by LASL for the S-07-6 runs was extensively modified by Sandia to incorporate the upper head, guide tube, support columns and upper head bypass line into the reactor vessel module. These modifications were made to predict counter-current flow better than was possible with the 1-D drift flux models currently used in TRAC. In this case, the counter-current flow was expected in the guide tube and support columns. Other modifications to the MOD3 nodalization used for S-07-6 involved adding a UHI accumulator system, moving the pressurizer from the intact loop to the broken loop, and modifying the broken loop pump data to reflect the most recent INEL data.

The Semiscale MOD3 UHI nodalization thus generated was then used to predict the steady state behavior just before the initiation of a UHI systems operation drain test to be performed at INEL.⁶ Predicted flow rates and temperature drops in the calculation were very close to the design values. Several attempts were then made to perform a transient calculation, but they all failed at about 18 s of transient time. The failures were apparently caused by broken loop pump instabilities. No resolution of this problem was achieved this quarter.

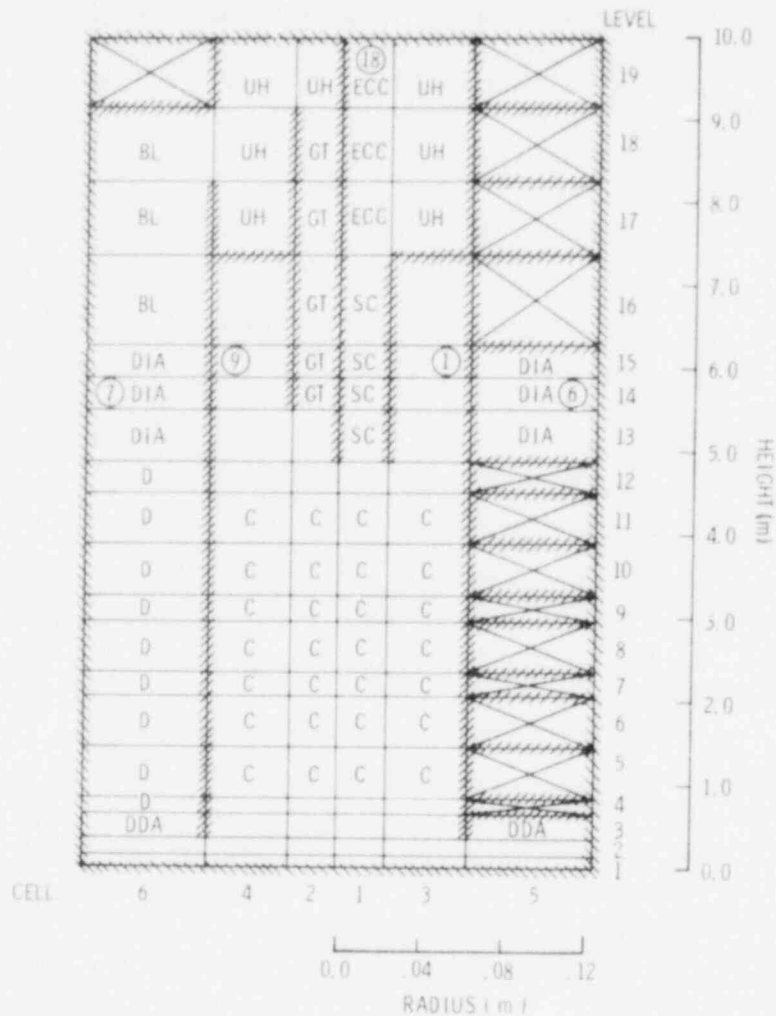
4.2.2 UHI Drain Test Prediction

Before initiating the Semiscale MOD3 Series 8 (UHI) tests, INEL will perform a systems operations test to evaluate the ability of the MOD3 system to meet the Series 8 objectives. This test will be a 200% noncommunicative, cold-leg break, loss-of-coolant experiment (LOCE) with core power tripped to zero at initiation of disc rupture.⁶ Sandia was asked by NRC to make a pretest prediction of this test with the TRAC code.

Because of the upper head injection for this test, we decided that the MOD3 system nodalization developed by LASL for S-07-6 (which modelled the upper head and main vessel as separate components connected by pipes representing the guide tube, support columns, and bypass line) was not adequate. That decision was based on the fact that the slip correlations used in the 1-D drift flux equations for flow in the pipes could not properly describe the counter-current flow expected in the guide tube and support columns. Consequently, the MOD3 vessel module was totally revised to consolidate the five separate components which used a combination of drift flux and two-fluid equations into one vessel module which uses the two-fluid equations everywhere.

Since no detailed documentation was available on how the original MOD3 nodalization was developed, the new nodalization was based almost totally on the engineering drawings. INEL personnel were consulted as necessary when information was not readily available from the drawings.

Figure 4-1 shows a cross-section through the new MOD3 vessel nodalization; the nomenclature used in the figure is listed immediately afterward. As indicated, the vessel contains 100 computational cells (14 cells pictured are not active in the calculation); there are 6 fluid cells per axial level and there are 19 levels. The core region has seven axial levels, two radial rings, and two azimuthal segments. The radial rings were chosen to allow a reasonable representation of the high power region of the Semiscale core even though the drain test currently being modelled will not use the high power region capability.



- Cell Fluid cell number within an axial level for TRAC numbering convention
- Level Axial cell number for TRAC numbering convention
- No flow permitted across this boundary
- Computational cell blocked off and inactive
- Cell in vessel for which component connected to junction N serves as a source
- UH Upper head
 - BL Bypass line
 - ECC Upper head injection nozzle
 - GT Guide tube
 - SC Support columns
 - DIA Downcomer inlet annulus
 - D Downcomer pipe
 - DDA Downcomer distribution annulus
 - C Core region

Figure 4-1. Cross Section Through Vessel 13

It should be noted that a code modification was required to properly model the bypass line connecting the downcomer inlet annulus and the upper head. For flow purposes, TRAC ordinarily calculates a hydraulic diameter based on the actual cell boundaries with no regard for any reduction in cell size by the volume fraction input data. This procedure leads to a large wall friction factor error when trying to model a small diameter line with a very large cell. The correct hydraulic diameter was hardwired into the code for the bypass line cells to eliminate this error.

As indicated in the introduction, other portions of the S-07-6 nodalization also had to be modified to accurately model the UHI drain test. For example, the pressurizer is specified to be in the broken loop for the drain test and it was in the intact loop for S-07-6. The broken loop configuration for the UHI drain test does not include an ECC injection system, so it was removed from the S-07-6 nodalization (the S-07-6 test actually did not have ECC in the broken loop either, but the test description from which the nodalization was developed gave specifications for one and it was included in the model). An accumulator with no high pressure or low pressure injection system was added to the upper head in the new nodalization. In addition, all of the system piping volumes were checked against the test specifications and a few minor changes were made to achieve agreement.

The final modelling modification involved the broken loop pump specifications. As a result of measured pump performance data in their S-A7-6 test, INEL produced a new set of homologous head curves and associated rated conditions for the Semiscale broken loop pump.⁷ These new data were used for the drain test calculations performed this quarter instead of the head curves and rated conditions used in the S-07-6 calculations. The older broken loop pump curve data had been supplied to LASL by INEL long before S-A7-6 was performed. Neither the new pump head curves nor the pump head curves used for the S-07-6 calculations corresponds to the TRAC built-in curves which were based on Semiscale MOD1 pump data.

A schematic of the new Semiscale MOD3 system nodalization is given in Figure 4-2. Although not noted in the figure, there are approximately 110 cells in all of the 1-D components with about one-fourth of those being in the two break nozzles. This makes the total number of computational cells about 210 which is a reasonable number for a complete system model.

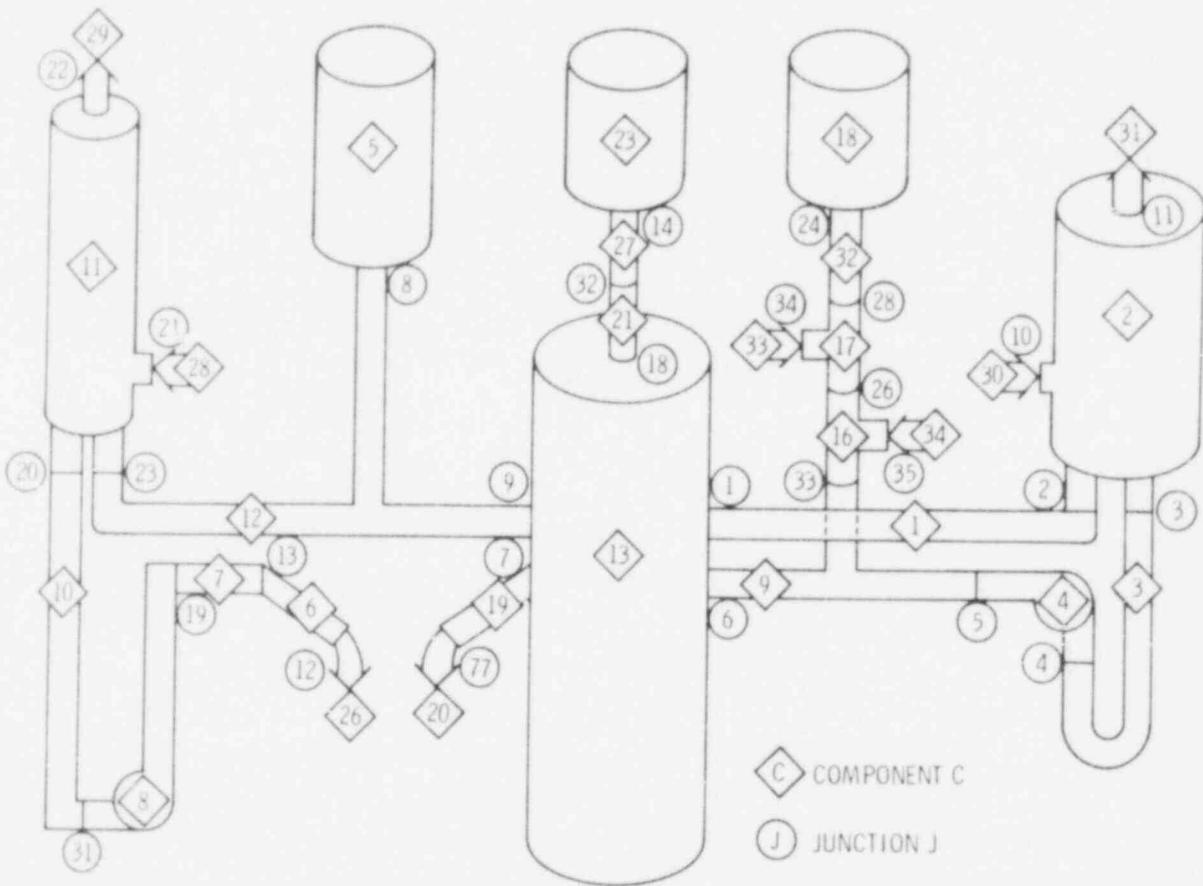


Figure 4-2. UHI Drain Test Nodalization

The only suspected shortcoming of the new Semiscale MOD3 nodalization is the heat slab treatment. Since a true conduction solution is not available for heat slabs in TRAC (and especially not for multilayer, insulated structures), no heat slabs were employed to simulate vessel walls which might conduct their heat to the fluid. We decided that the most important walls in the vessel were insulated and too much heat might be inadvertently added if unsupported guesses were made about how large a heat slab to use. If the initial calculations do not predict the data well, that is one area in which improvement of the modeling is possible.

Using the above described nodalization (with a one-cell pipe connecting the two break nozzles), a series of steady state calculations was performed. A considerable amount of effort went into ensuring that the final steady state solution was reasonable. One important factor in achieving a realistic flow split between the downcomer and bypass line involved the correct description of the bypass line hydraulic diameter mentioned above. Another important factor was an additive form loss-friction factor applied at the base of the downcomer inlet annulus. We felt that the tapered cone design of the annulus was not properly accounted for without this additive friction.

Table 4-I contains a summary of a few important parameters from the steady state calculation. Since the pumps will be adjusted to achieve a ΔT_{core} of 37 K during the steady state operation before initiating the transient, the design flow rate values are only nominal. This means the calculated steady state solution is about as good as can be expected for a pretest calculation.

Table 4-I
Steady-State Value for UHI Drain Test

	<u>Design</u>	<u>Calculated</u>
$\Delta T_{\text{Broken Loop}}$	37.0 \pm 0.5 K	37.5 K
$\Delta T_{\text{Intact Loop}}$	37.0 \pm 0.5 K	36.8 K
Downcomer Flow	-	12.45 1/s
Bypass Flow	-	0.43 1/s
Total Flow	13 1/s	12.88 1/s
$\frac{\text{Bypass Flow}}{\text{Total Flow}}$	4%	3.4%

Starting from the steady state condition, a calculation of the drain test transient was then initiated. At about 0.7 s into the transient, the broken loop pump went numerically unstable. As the oscillations grew, a water packing situation developed which caused TRAC to pursue a

slightly different calculational path for a short period of time. This apparently allowed the code to recover from the original instability. However, at about 12.5 s of transient time, the transient calculation started to experience thousands of 1-D drift flux solution errors, most of them at the broken loop pump or the associated break nozzle. This calculation failed completely at about 13.35 s due to a negative specific heat being used in a critical heat flux calculation.

After checking and rechecking the input data, we assumed that some basic problem existed with the differencing scheme used for pumps in the FRAC code. Some minor alterations were made to that scheme and the calculation was rerun, getting to about 18 s of transient time, but again with literally thousands of drift flux solution failures. Obvious pump instabilities were also present in this calculation. Figure 4-3 indicates the beginning of one such instability at about 8.0 s of transient time (plotted on a very expanded scale).

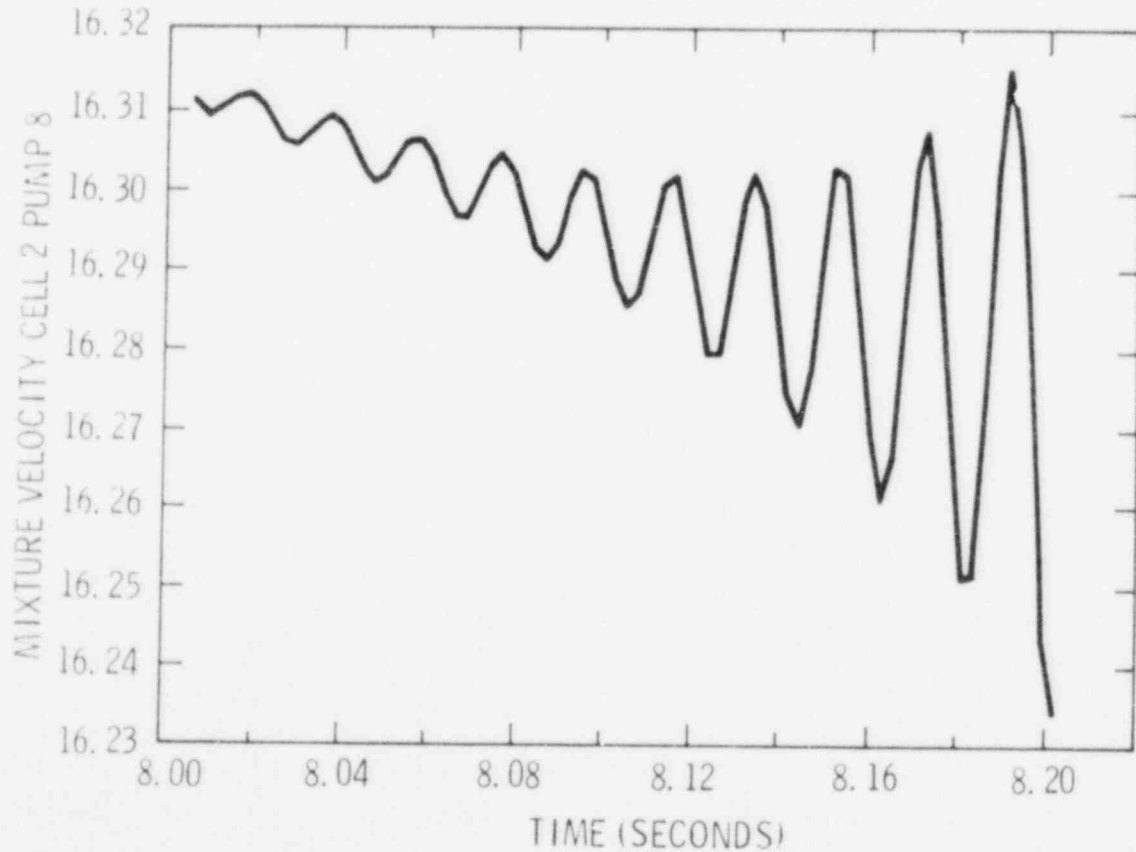


Figure 4-3. Mixture Velocity in Broken Loop Pump

No further attempt was made to resolve the pump instability problem after this second failure. Instead, because of the urgency of generating a pretest prediction for the UHI drain test, the decision was made to go back to the broken loop pump description used for the S-07-6 calculations which had not exhibited such obvious instabilities. Those calculations, however, were not initiated this quarter.

4.3 RELAP Reflood Progress

Several preliminary calculations were performed to resolve questions before the UHI audit calculation could be attempted. A list of those discussed in this quarterly is given in Table 4-II. Figure 4-4 illustrates the system nodalization for those calculations. Although the final UHI calculation will use a CRF averaged over 10 power regions, the calculations presented here used only 1 power region. This was done in order to determine more easily the interrelationship of CRF, core exit enthalpy, initial rod temperature profile, and various code changes and options.

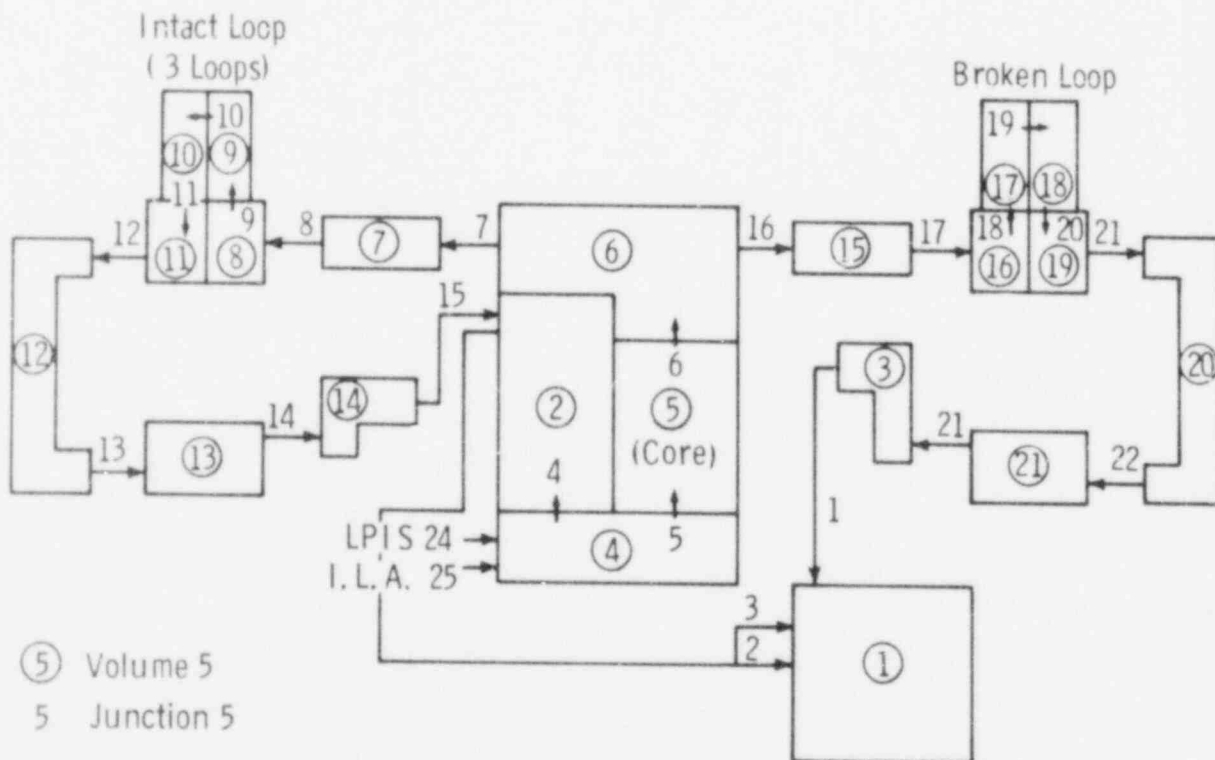


Figure 4-4. RELAP4/MOD5-FLOOD Nodalization

Table 4-II

FLOOD Parameter Study Calculations

Run Name	Rod Thermal State	Core Exit Enthalpy	Comments
FLDEN36	Hot	1160 Btu/lb	Intact loop accumulator fill table for 90 s
FLDEN37	Cold	1160 Btu/lb	Radiation h.t. fix for low temperature rod
FLDEN38	Cold	1300 Btu/lb	Minimum CRF set at 0.0024
FLDEN39	Cold	Variable	Calculation terminated due to instabilities

The following statement was incorporated into the CRF model for the remaining calculations. IF (CRF. GT.0.5) CRF = (CRF+1)*0.5

FLDEN41	Hot	1300 Btu/lb	
FLDEN42	Hot	1160 Btu/lb	Intact loop accumulator fill table for 30 s

The water pack option was utilized in the remaining calculations

FLDEN43	Hot	1160 Btu/lb	No fill contribution from intact loop accumulator
FLDEN44	Hot	1160 Btu/lb	Intact loop accumulator fill table for 30 s
FLDEN45	Hot	1300 Btu/lb	
FLDEN46	Hot	1160 Btu/lb	Error fixed in FLOOD junction flow calculation

Two different initial temperature profiles were used in this analysis: a "hot" and a "cold" rod. The hot rod had an initial quench height of 48 in. and a TINIT of 650°F while the cold rod was considered totally quenched with a TINIT of 430°F. The initial quench height and the TINIT quantity are used in the CRF model.

Figures 4-5 and 4-6 illustrate the effect of the initial rod conditions on the core mixture level and inlet core reflood rate. These results show only the effect of the CRF correlation with the two initial conditions; the hot rod will have a higher CRF than the cold rod at the same elevation. Therefore, the calculation with the cold rod will refill the core much faster than the one with the hot rod. Figure 4-6 shows that the inlet flooding rate is essentially the same for both initial conditions after an early oscillatory period. The reasons for these oscillations and their relative magnitudes will be discussed in a later section of this report.

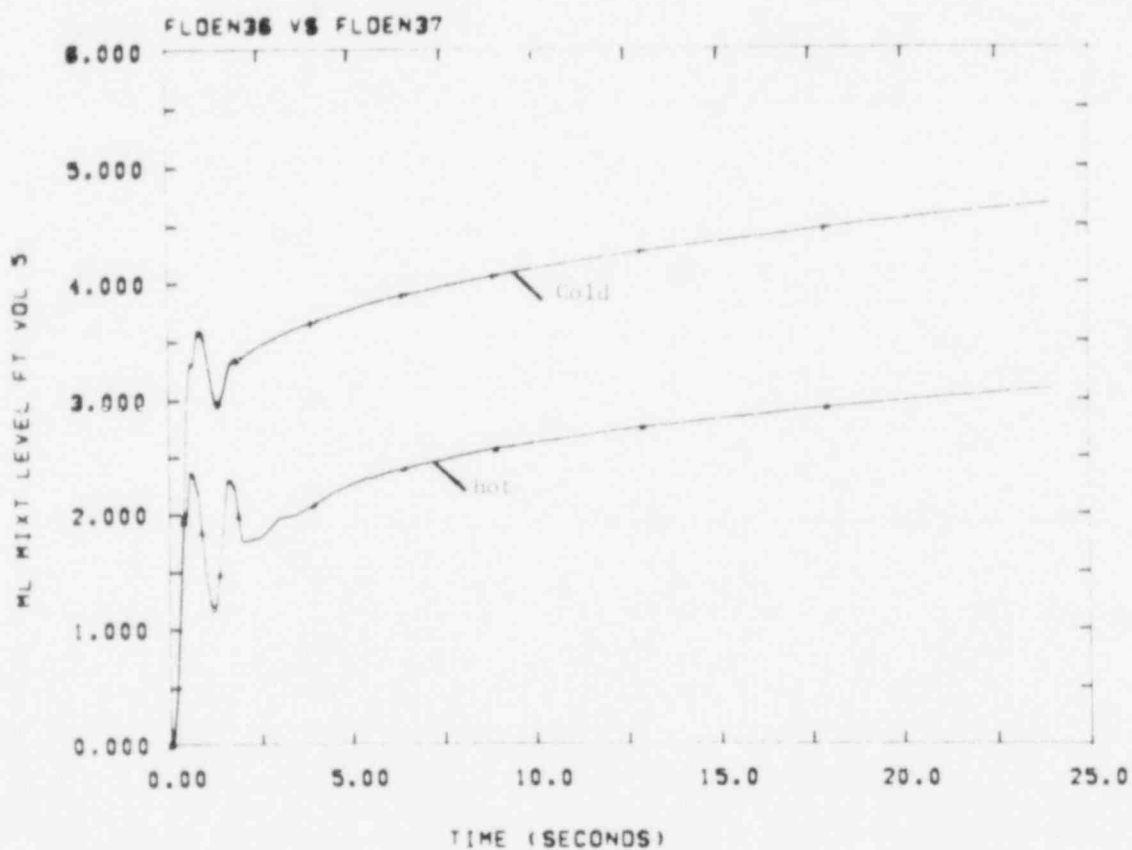


Figure 4-5. Core Mixture Level; Hot vs Cold Rod Conditions

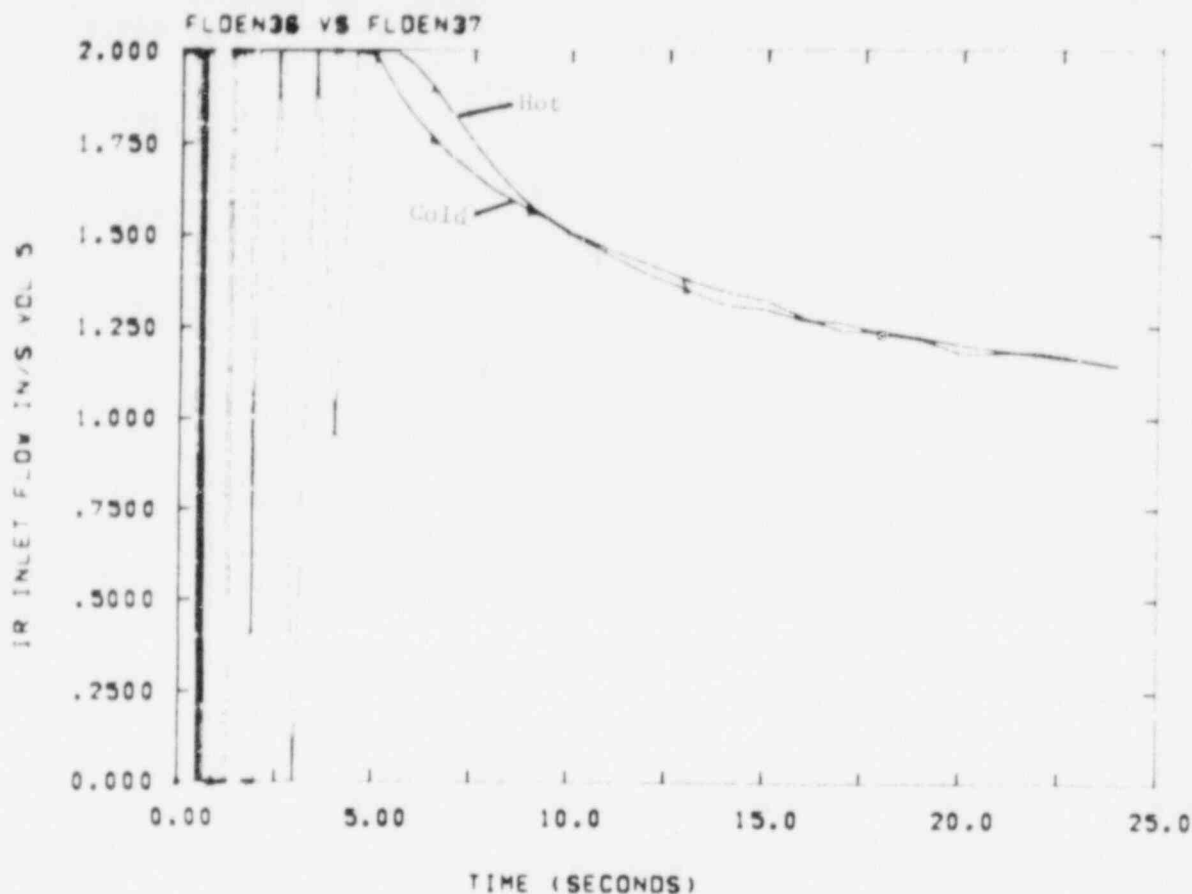


Figure 4-6. Core Inlet Flow; Hot vs Cold Rod Conditions

It should be noted at this point that the FLECHT heat transfer correlation in the current version of RELAP4/MOD5 at Sandia is not able to calculate heat transfer coefficients correctly for the cold rod. This is because the FLECHT correlation is for hot rods; a midplane temperature of less than 700°F results in a negative radiation heat transfer coefficient where positive is assumed from the rod to the fluid. To circumvent this problem, the radiation coefficient was set to 1.0 Btu/hr-ft²-°F for this discussion. Even though this fix does not affect the calculation due to the decoupled way in which the FLOOD code is being utilized, a radiation heat transfer coefficient of this magnitude could be defended on physical grounds. If the FLOOD code were used to determine the time varying clad temperature during the reflood phase of a UHI analysis, the suitability of the FLECHT correlation would have to be reanalyzed in the low temperature region.

Figures 4-7 through 4-9 illustrate the effect of constant core exit enthalpy on the results. Unlike the previous comparison, the CRF is altered only through a change in system conditions; this is the feedback from the inlet flow rate into the correlation. Two other investigations^{8 9} have used a value of 1300 Btu/lb for their non-UHI calculations. However, as will be discussed later, the system initial conditions of the UHI re-flood are different from those of the non-UHI geometry.

Figure 4-7 shows that the long term effect of this input change is a slightly lower core level with the larger exit enthalpy. The higher exit enthalpy results in a lower inlet core velocity, as illustrated in Figure 4-8, which causes the CRF to be lower. A comparison of Figures 4-5 and 4-9 indicates that the effect of exit enthalpy is much smaller than that of the initial state of the rod. Figure 4-9 shows that after a few seconds, the slopes of both curves are approximately the same.

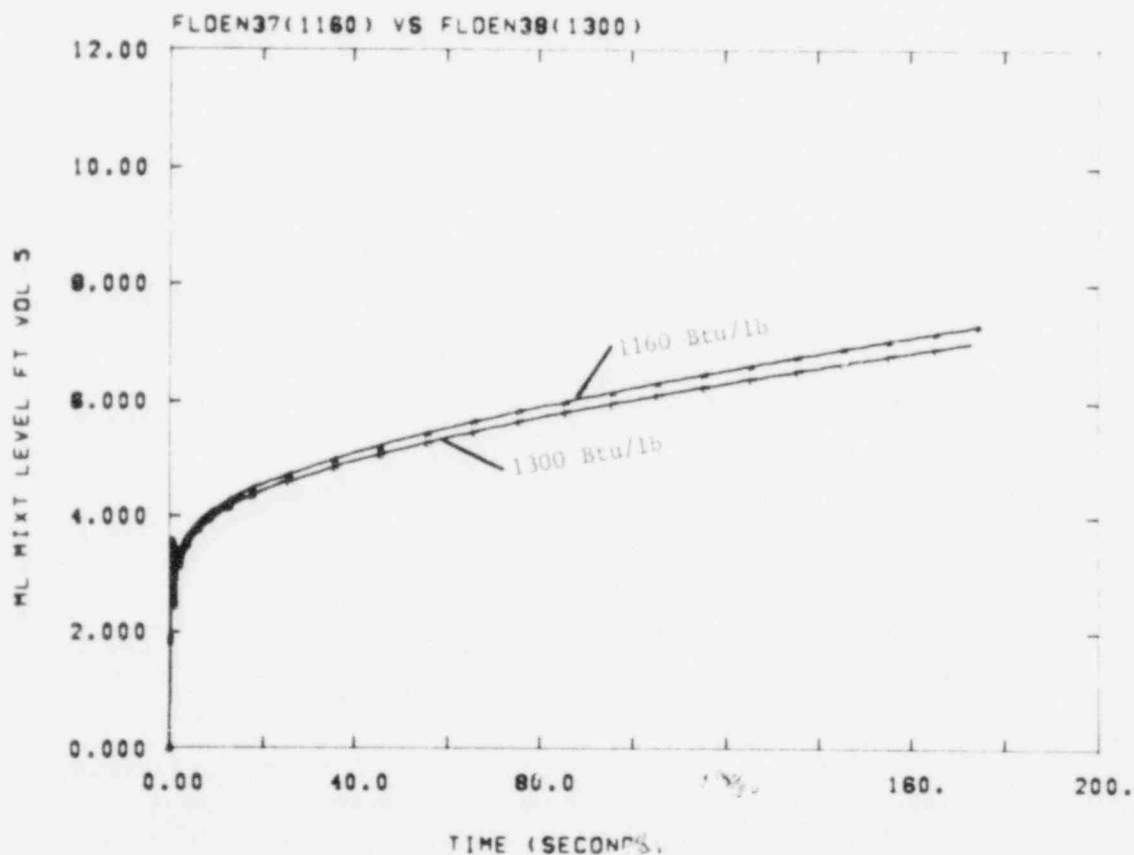


Figure 4-7. Core Mixture Level; effect of Core Exit Enthalpy (Cold Rod)

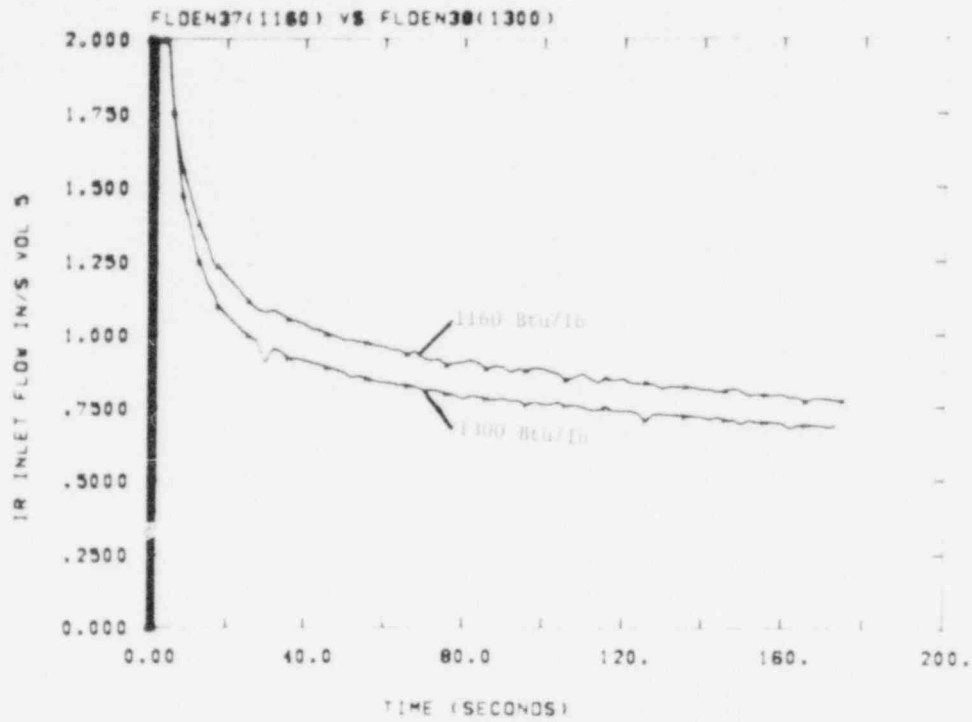


Figure 4-8. Core Inlet Flow; Effect of Core Exit Enthalpy (Cold Rod)

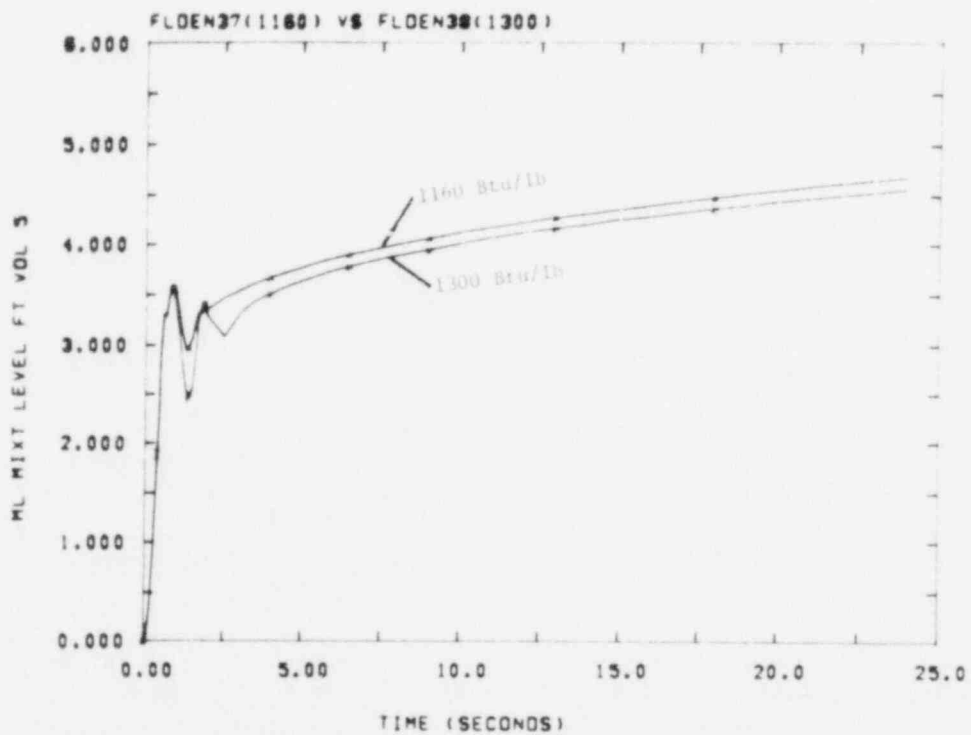


Figure 4-9. Core Mixture Level; Effect of Core Exit Enthalpy (Cold Rod) (Closeup)

Figures 4-10a and 4-10b illustrate the effects of the same variable change, i.e., the core exit enthalpy, as the previous comparison; however, the hot rod temperature profile is used instead of the cold rod in this example. Notice the large oscillations early in the calculation for an enthalpy of 1300 Btu/lb. These are due in part to the higher initial CRF of the hot rod coupled with the higher core exit enthalpy. Another factor, which will be discussed later is the downcomer initialization. However, based on these examples, several conclusions can be drawn concerning the core exit enthalpy. First, the core exit enthalpy must be evaluated for the particular stored energy and system conditions. For the present UHI nodalization, Figures 4-7 and 4-10 clearly show that 1150 Btu/lb should be chosen for stability reasons. Second, the long term results for both figures are surprisingly very similar. That is, the mixture level at 150 s differs by less than 5 in. for the two calculations. Although, as the Exxon report⁹ also indicates, the higher value leads to conservative flooding rates in both examples; initial stability requirements must also be considered. Finally, even though the use of a constant core exit enthalpy does not obey any thermodynamic laws, it is needed for the present UHI-FLOOD analysis. Calculation FLDEN39, without the constant exit enthalpy option, went unstable and terminated at 70 s into the reflood phase. This occurred even though the calculation had appeared to be stable through the initial reflood oscillations. INEL recommends the use of a constant exit enthalpy because of its stabilizing effect on the code due to the limited modelling of core thermodynamics and vapor generation. Also, the present UHI analysis requires the use of a constant value because 10 power regions are being described by the CRF model for the core hydraulics, while only 1 power region can be modelled by the code's limited heat transfer package.

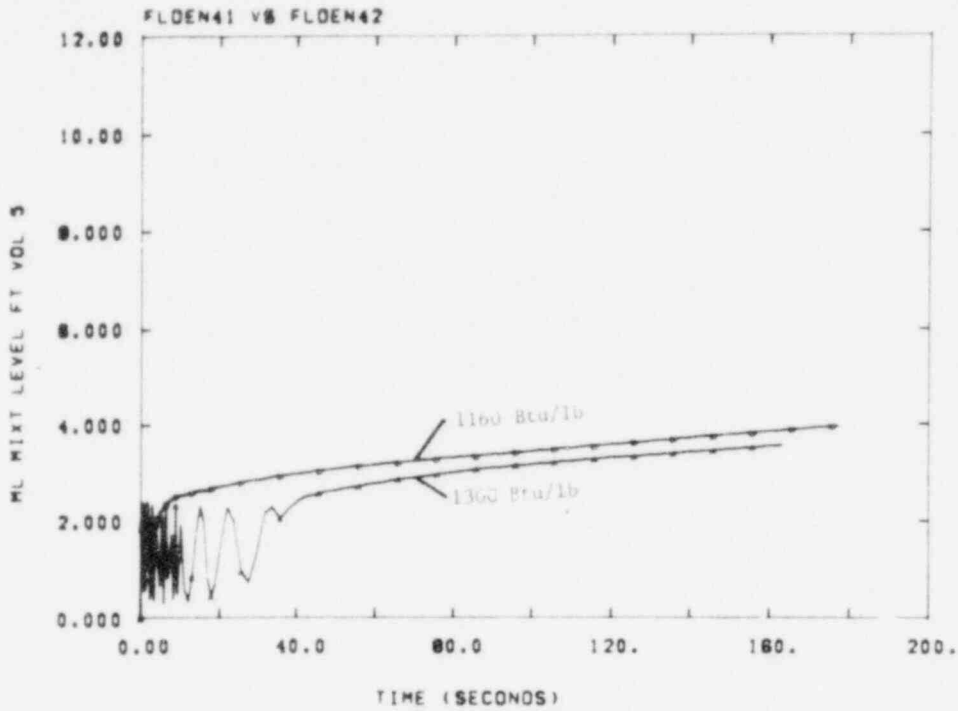


Figure 4-10a. Core Mixture Level; Effect of Core Exit Enthalpy (Hot Rod)

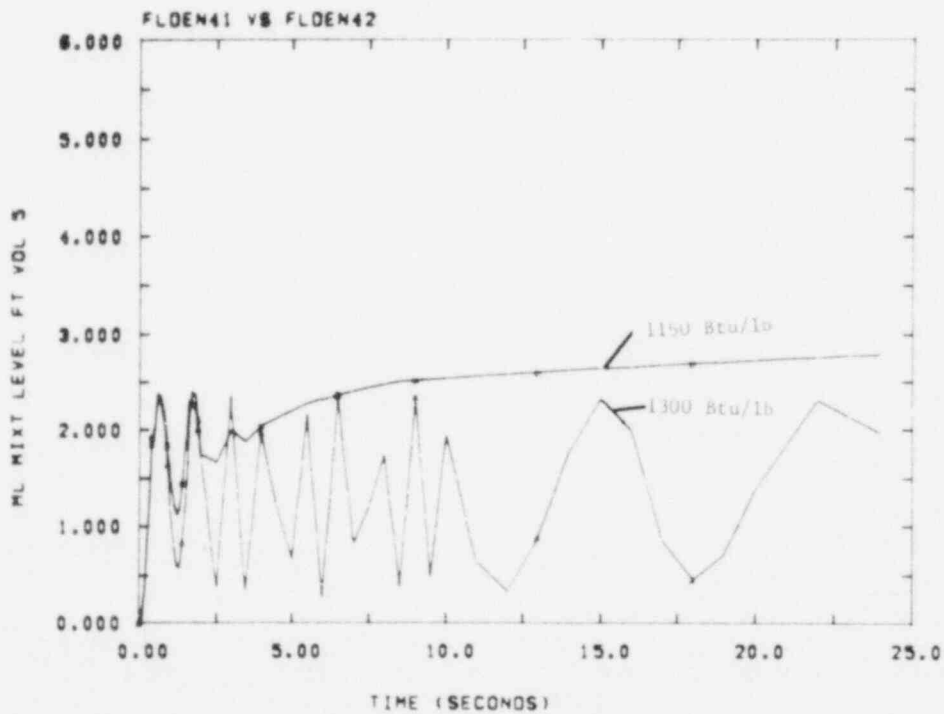


Figure 4-10b. Core Mixture Level; Effect of Core Exit Enthalpy (Hot Rod) (Closeup)

Figures 4-11 and 4-12 illustrate the effect of an NRC licensing requirement for a recalculation with a more conservative CRF if the clad temperature rise is terminated by the quench front. The previous quarterly⁵ described how a discontinuity in the Westinghouse (W) CRF model was smoothed; however, the NRC requirement leads to a large discontinuity in the CRF at 0.5. Figure 4-11 shows that, for this calculation, the jump occurred at approximately 2 s. Figure 4-12 shows the late time effects of this requirement. In our calculations, however, the temperature excursion was observed to be terminated by the transfer to the entrained liquid, rather than by the quench front.

Figures 4-13 and 4-14 illustrate the effect of an intact loop accumulator fill into the lower plenum. At the beginning of reflood, the three intact loop accumulators have 30 300 lb of water remaining. Since the discharge ΔP will remain essentially constant during reflood, a constant initial discharge rate of 1900 lb/s would completely empty the accumulators in approximately 16 s. Figure 4-13 shows the long term effects of an intact loop accumulator fill into the lower plenum. The mixture levels are almost indistinguishable. The initial differences, shown in Figure 4-14, will be explained later when the downcomer initialization is discussed.

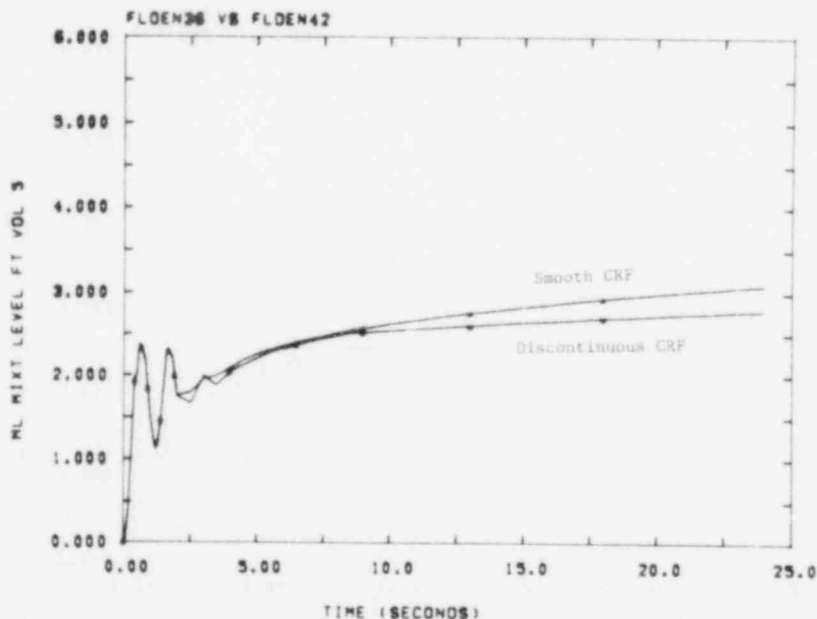


Figure 4-11. Core Mixture Level; Effect of CRF Discontinuity (Closeup)

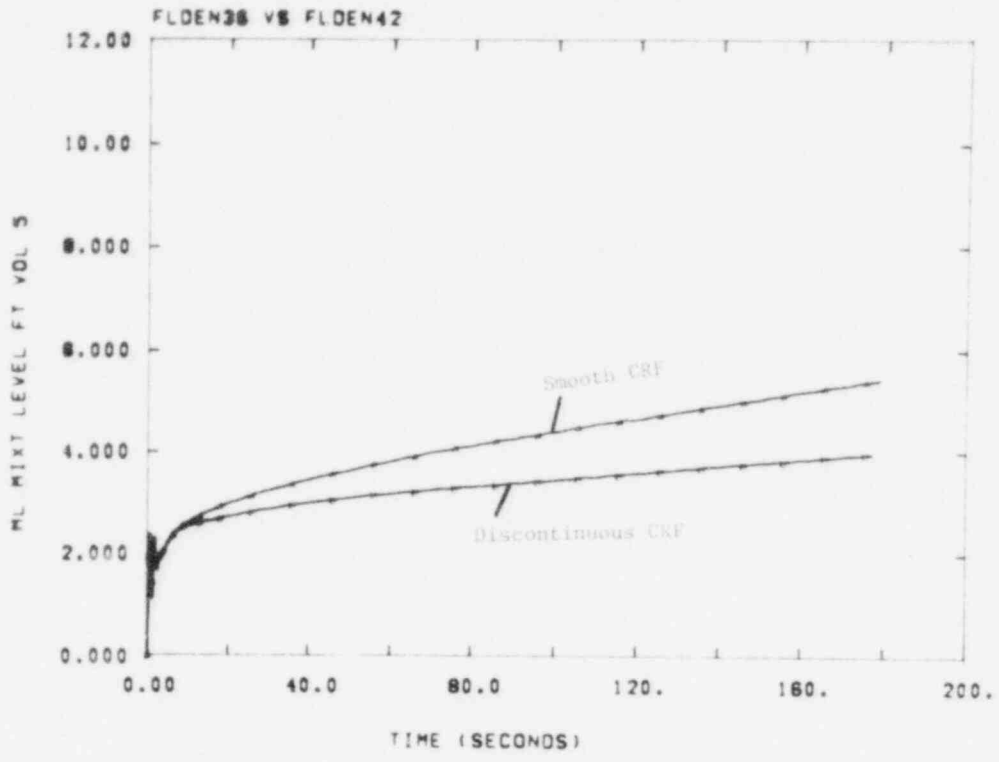


Figure 4-12. Core Mixture Level; Effect of CRF Discontinuity

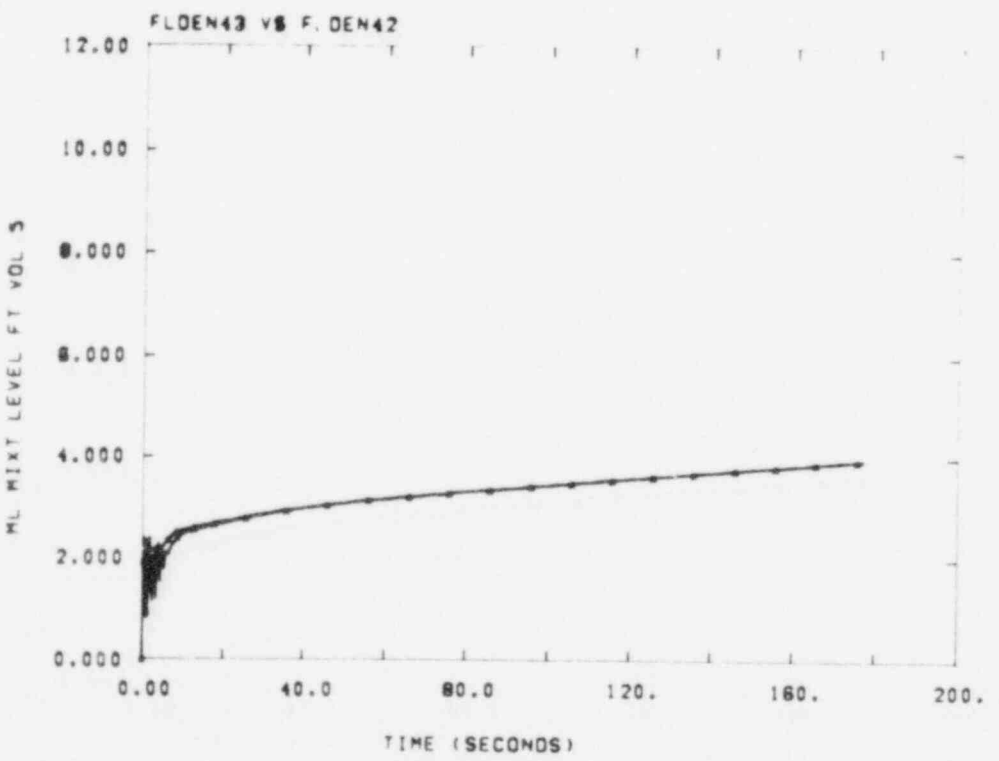


Figure 4-13. Core Mixture Level; No Accumulator Fill vs 30-s Fill

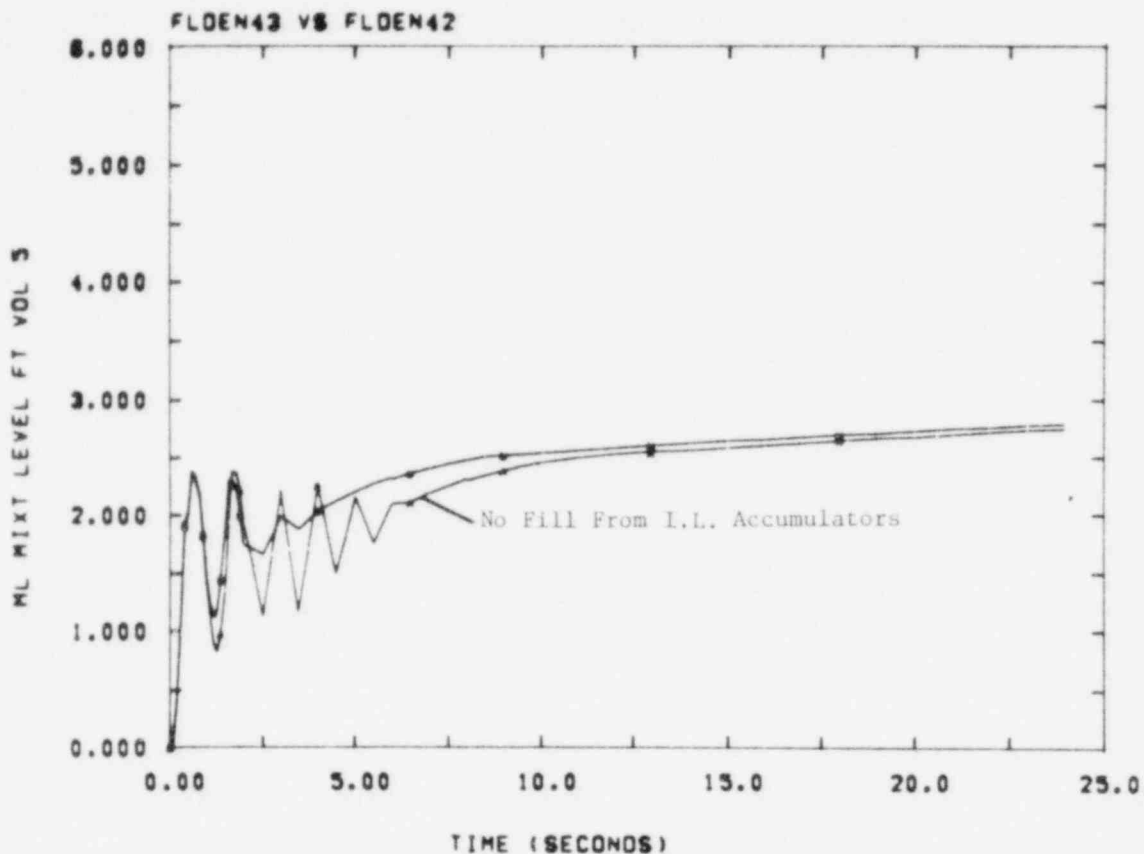


Figure 4-14. Core Mixture Level; No Accumulator Fill vs 30-2 Fill (Closeup)

Figures 4-15 and 4-16 illustrate the effect of the water pack option on the reflood calculation. There is no discernible difference in the results. The water pack option is invoked, because the lower plenum is initially filled with saturated water and a subcooled fill is initiated at the start of reflood. An analysis of the calculation concludes that the water pack option was invoked only about a dozen times; however, the ratio of reactor time to execution time was larger with the option. This is due to the time step control reduction in the calculation without the option. A comparison of calculation FLDEN45 and FLDEN41 showed that the early flow oscillations in the reflood calculation were not due to the water pack phenomenon.

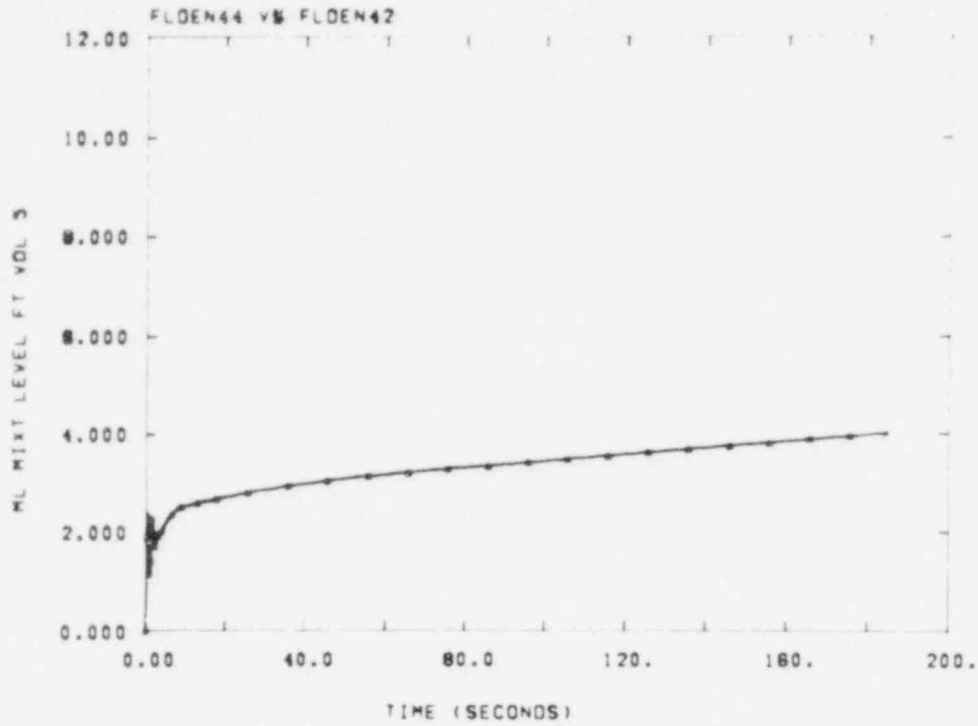


Figure 4-15. Core Mixture Level; Effect of Water Pack Option

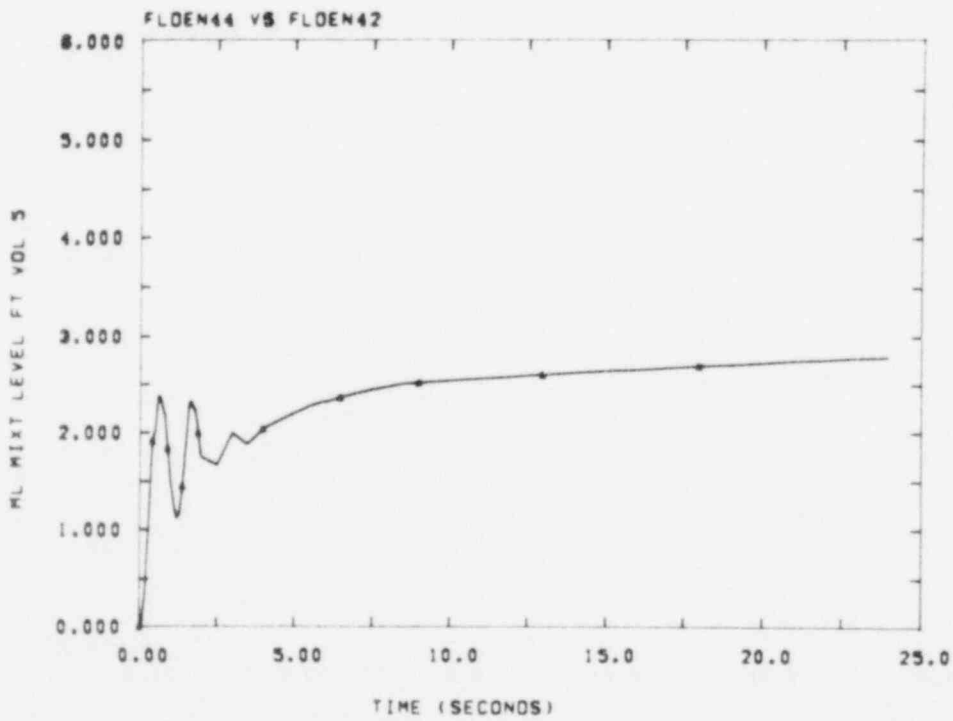


Figure 4-16. Core Mixture Level; Effect of Water Pack Option (Closeup)

Figure 4-17 illustrates the effect of an error in the RELAP4/MOD5 code when the FLOOD option is utilized. This error caused incorrect junction mass flows to be calculated, with the magnitude of the error being dependent on the system nodalization. For example, the intact loop accumulator junction flows produced by the code in the FLOOD option were significantly lower than Bernoulli-calculated flows (570 lb/s vs 1900 lb/s). The flow was highly subcooled and not choked. The hand calculation was verified by a RELAP4/MOD5 calculation utilizing a two-volume problem without the FLOOD option.

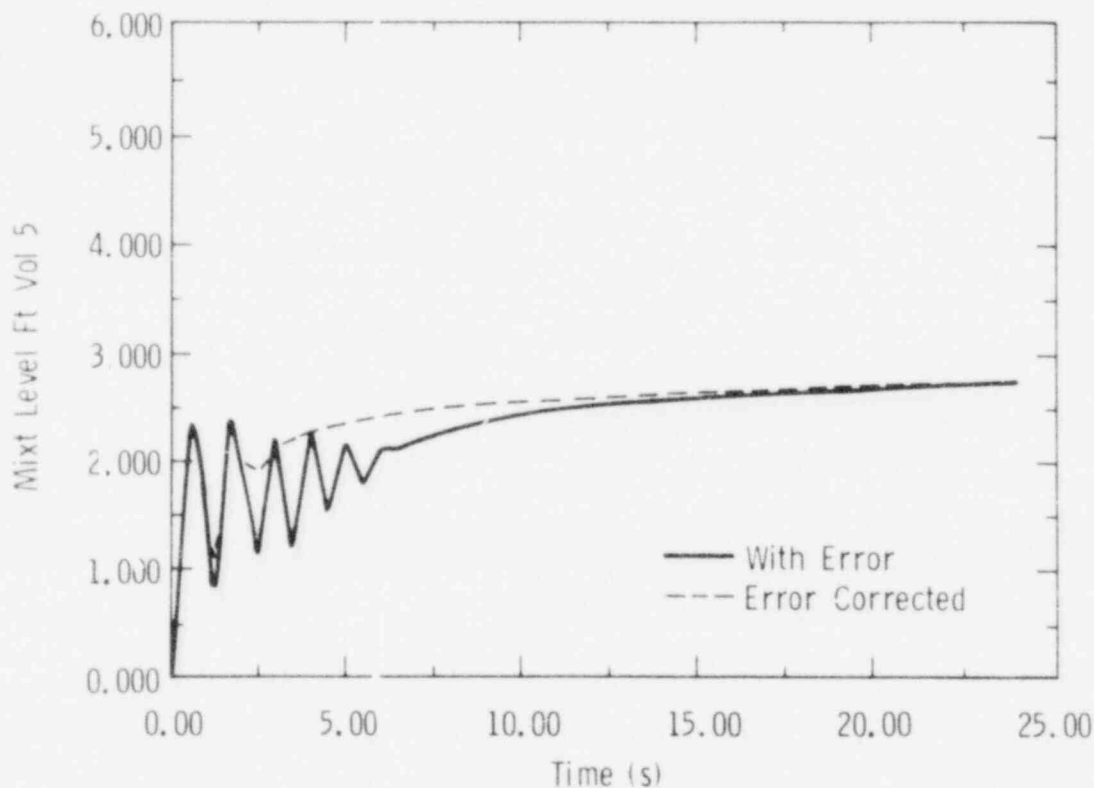


Figure 4-17. Core Mixture Level; Effect of Flow Error Correction

We determined that the horizontal slip option is subroutine FLOSRRH was always activated when the FLOOD option was utilized. That is, all junction areas were altered by the steam and liquid slip junction areas (FLOOD model options) before we calculated the form-loss friction factors. In the accumulator junction flows, this resulted in a reduction of a factor of 3. This error was traced to an INEL update on November 14, 1977 which deleted cards 14656 through 14658. Card 14656 was the control

statement which allowed only the designated junctions to be modified. Therefore, only cards 14657 and 14658 will be deleted in future calculations.

The effect of this error in the present analysis using a UHI nodalization is shown in Figure 4-17, which illustrates the core mixture level. The late time results show little effect due to the error; however, in the initial phase of the calculation, the error produced more oscillations with many flow reversals. This behavior is compounded by the initialization of the downcomer for the UHI analysis, as will be discussed below.

Downcomer Initialization

Figure 4-18 illustrates the downcomer nodalization for the FLOOD analysis. Note that the broken leg junction to the containment has been modelled as two separate junctions; one for steam and one for liquid. This nodalization has resulted in an interesting effect, in part because of its application.

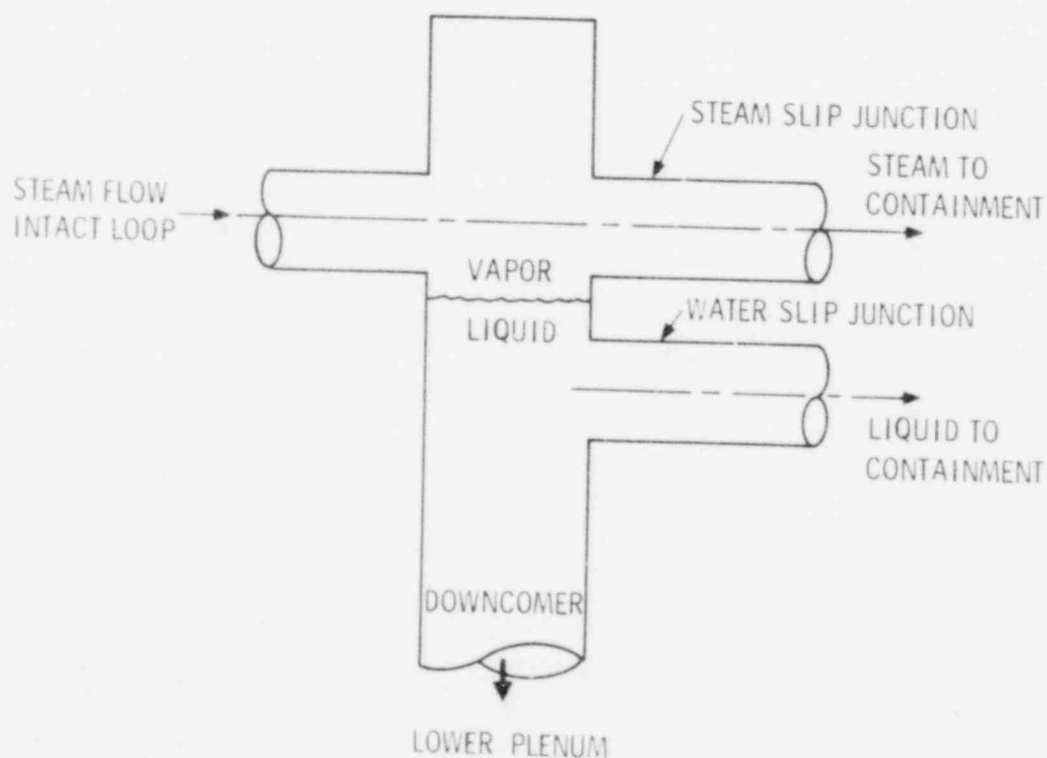


Figure 4-18. Downcomer Nodalization

The state of the downcomer at the beginning of reflood for a UHI analysis is different than for non-UHI calculations; the downcomer is assumed to be full of water due to steam binding in the core. In the preceding calculations, the initial mixture level was 0.96 ft above the intact loop nozzle centerline. At near steady state conditions into reflood, this level had decreased approximately 4 ft to the water slip junction elevations. This drop manifests itself as manometer-like oscillations in the core mixture level. These can be seen in Figures 4-5 through 4-17, but are especially noticeable in Figures 4-8, 4-14 and 4-17. These oscillations continue until they are damped to a steady-state value; the damping is controlled by the oscillating mass inventory.

Therefore, CRF changes affect the initial behavior as illustrated in Figure 4-6. As one would expect, the higher initial CRF of the hot rod resulted in a longer period for the system to stabilize. This trend is continued when an unquenched rod is used; severe oscillations are experienced which result in code failure. The coupling of the CRF and core exit enthalpy is illustrated in Figure 4-10a. The hot rod and high exit enthalpy combine to produce large oscillations before they are finally damped. Figure 4-14 illustrates that additional mass flow into the lower plenum reduced the period of the oscillations for the hot rod. This is reasonable because the higher CRF is offset by the increased system mass. And finally, the error fix as is shown in Figure 4-17, increased the damping of the oscillations.

Figure 4-19 shows typical downcomer mixture levels, with and without the correction. The quasi-steady state level is clearly shown.

Carryout-Rate-Fraction (CRF)

The Westinghouse CRF model⁴ was modified slightly for the present analysis. As discussed in the previous quarterly⁵, a one foot transition region was utilized to smooth the discontinuity which existed when the core mixture level exceeded the initial quench elevation. Figure 4-20 illustrates this transition region for an average power rod with initial

quench height of 48 in. One can notice that although the correlation temperature is simply linearly interpolated in space (36 to 48 in.), the resulting CRF is approximately exponential. Another modification is the insertion of an NRC requirement resulting in a jump discontinuity as shown in Figure 4-20. This requirement forces the calculated CRF to be modified to $(1.0+CRF)*0.5$ when $CRF > 0.5$ and the clad temperature increase is terminated by the quench front.¹⁰ The full impact on the clad temperature during reflood is not clear from the present analysis. The effect cannot be ascertained because FLOOD is essentially being used as a hydraulics code during reflood since the current heat transfer package is inadequate for the colder UHI rods.

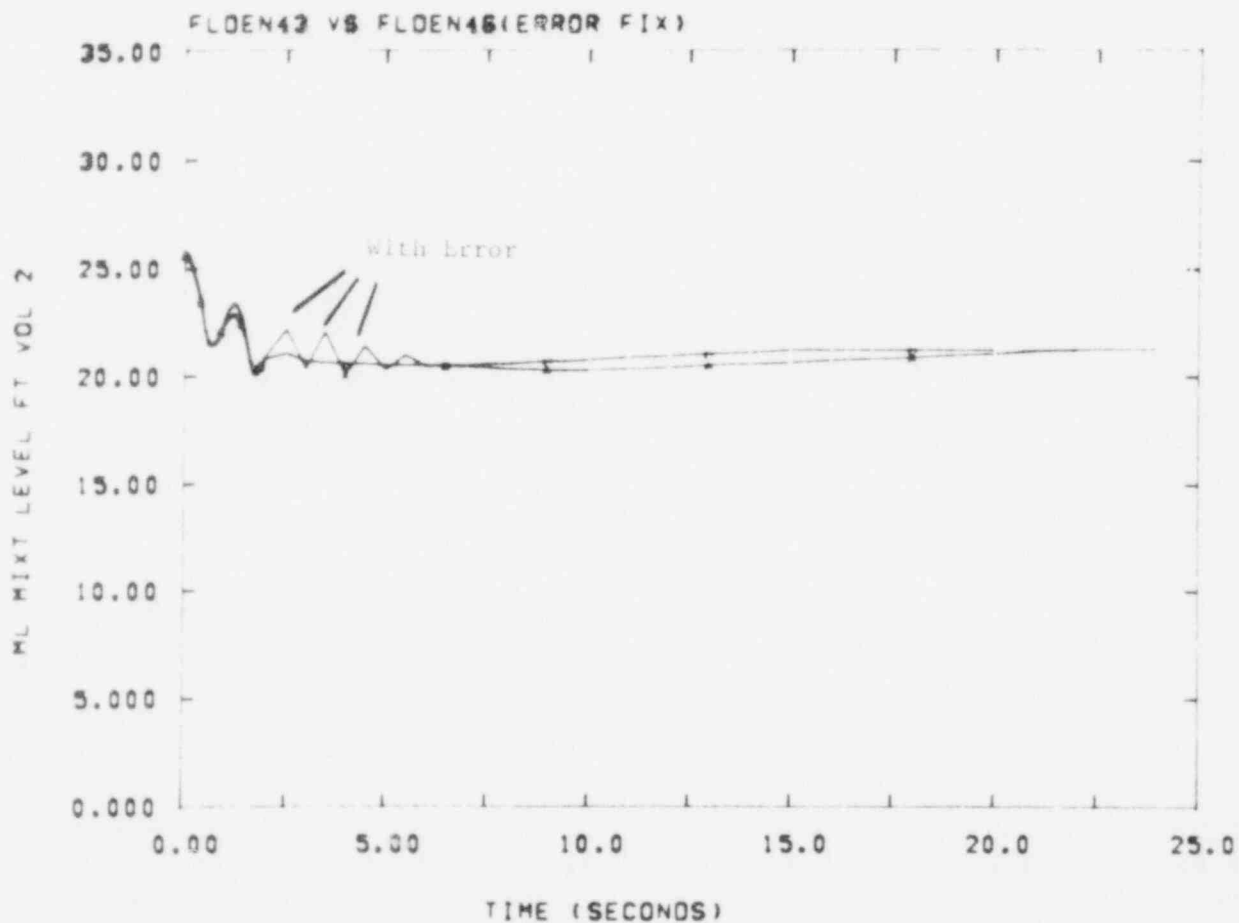


Figure 4-19. Downcomer Mixture Level; Effect of FLOD Error Correction

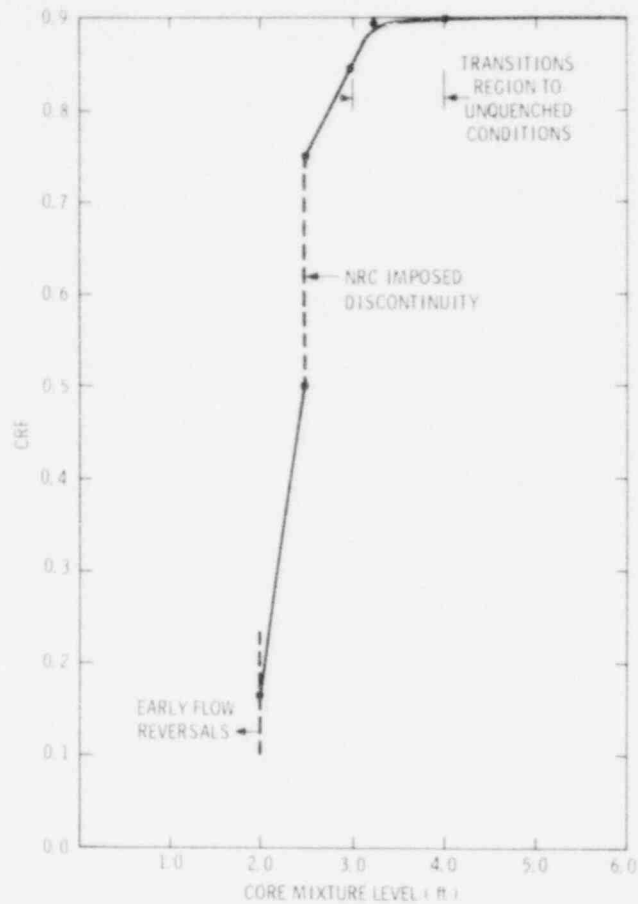


Figure 4-20. Typical CRF Profile

The following minor modifications and control criteria were incorporated into the final CRF model:

let V_{IN} be the inlet core flooding rate (in/s)
 $V_{IN} < 0.0$ $CRF = 0.0024$ (flow reversal)
 $V_{IN} < 0.001$ Use old time step value of CRF
 $V_{IN} > 6.0$ $V_{IN} = 6.0$
 let h be the core mixture level (in)
 $h \leq 6.0$ $CRF = 0.0024$
 and finally,
 $CRF < 0.0024$ $CRF = 0.0024$

These changes are primarily intended to deal with problem initialization and initial flow reversals. They have no effect on the results after the oscillations have been damped and the core is filling smoothly.

4.4 References

- ¹L. F. Siefkin, FRAP-T4--A Computer Code for the Transient Analysis of Oxide Fuel Rods, CDAP-TR-78-027, EG&G Idaho, Inc., July 1978.
- ²RELAP4/MOD5 A Computer Program for Transient Thermal-Hydraulic Analysis of Nuclear Reactors and Related Systems, ANCR-NUREG-1335, Aerojet Nuclear Company, September 1976.
- ³G. N. Lauben, TOODEE2: A Two Dimensional Time Dependent Fuel Element Thermal Analysis Program, NUREG-75/057 (Washington: US Nuclear Regulatory Commission, May 1975).
- ⁴M. Y. Young et al, Westinghouse Emergency Core Cooling System Evaluation Model Application to Plants Equipped with Upper Head Injection, Vol 1, WCAP 8479-P (Rev 2; Pittsburgh: Westinghouse Electric Corporation, Nuclear Energy Systems).
- ⁵Light Water Safety Research Program Quarterly Report, January-March 1979, SAND79-1542 (Albuquerque: Sandia Laboratories, October 1979).
- ⁶The information on this special systems operation test was obtained by private communication from Dale Snider, EG&G Idaho, Inc. (INEL).
- ⁷The information on the broken loop pump was obtained by private communication from Cliff Fineman, EG&G Idaho, Inc. (INEL).
- ⁸C. A. Dobbe, Zion Reflood Plant Decks Results, Internal EG&G Idaho, Inc. (INEL) report.
- ⁹4-Loop PWR with Ice Condenser Large Break Example Problem, XN-76-36, Exxon Company, August 1976.
- ¹⁰Safety Evaluation Report in Westinghouse Electric Company ECCS Evaluation Model for Plants with Upper Head Injection, NUREG-0297 (Washington: US Nuclear Regulatory Commission, April 1978).

5. Two-Phase Jet Loads (D. Tomasko, R. K. Cole, Jr.)

5.1 Summary

The ultimate objective of the Sandia Two-Phase Jet Load study is the development of an improved approximate engineering model to characterize two-phase jets emanating from circumferential or longitudinal breaks in a typical PWR piping system.

The following topics are discussed in this quarterly report: comparisons between TRAC-PIA calculations and experimental data obtained from research project RS-50 of Battelle-Frankfurt, Federal Republic of Germany (FRG); sonic plane locations obtained during simulated blowdowns with the Sandia computer code CSQ; and containment modelling using the TRAC-PIA vessel component.

A summary of the conclusions found in this report is as follows:

- TRAC-PIA calculations are generally in good agreement with Battelle-Frankfurt RS-50 data (pressures and impingement loads).
- Sonic plane locations obtained with CSQ generally occur near the center of the length of the exit pipe ($L/2$) because of the donor cell technique used in solving the fluid-mechanical equations. Resulting differences in exit conditions are small and should not significantly affect impingement load calculations. The magnitude of this effect, however, should be quantified.
- The modelling of a two-phase jet propagating through containment and impinging on a target can be accomplished with the TRAC-PIA vessel component. However, the time step control logic has to be modified to reduce excessive pressure oscillations and asymmetries caused by water packing in downstream cells. This type of

modelling will be very useful for longitudinal break studies which require three-dimensional capabilities.

5.2 Comparisons of TRAC-PIA Results With Battelle-Frankfurt Research Project RS-50

Research project RS-50 was performed by Battelle-Frankfurt at their test facility in Frankfurt.¹ This test facility is a 1/64 volumetric scale model of the German BIBLIS power reactor. A diagram of the circulation system for test RS-50-C12 is shown in Figure 5-1. The system incorporates both a large pressure vessel (5.3 m³) and a surge tank (0.87 m³) in simulating the BIBLIS PWR.

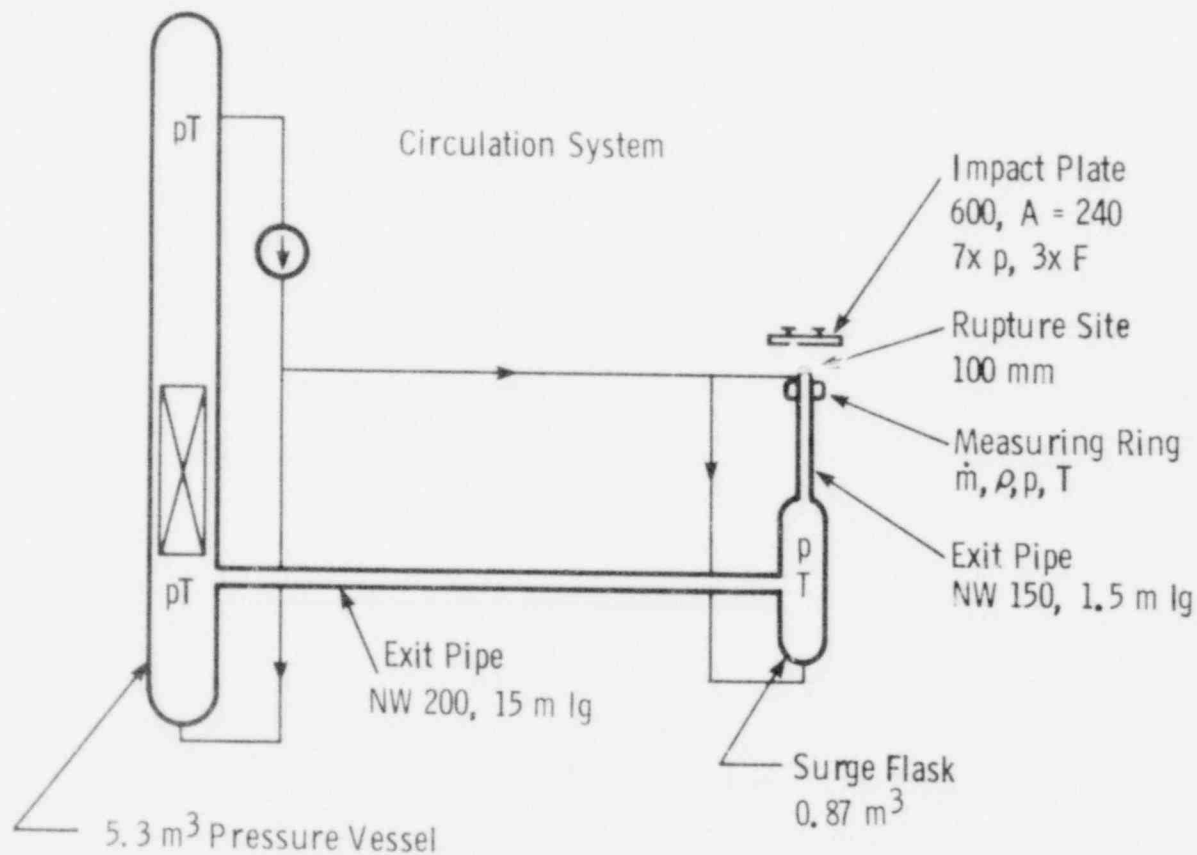


Figure 5-1. Battelle-Frankfurt RS-50 Circulation System

Figure 5-2 shows the nozzle and impingement plate configuration used in the RS-50 tests. Pressure is measured in the exit pipe near the location of the drag disc shown, and both pressures and forces are measured on the impingement plate located 240 mm from the rupture site. Fine time

resolution of the data was possible because of the high sampling frequency used (1 kHz). A gun was used to break the rupture disc and initiate the blowdown process. Asymmetric pressure distributions on the impingement plate and nonreproducible test results probably occurred because of incomplete opening of the rupture disc (restricted flow area in the exit pipe). In modelling RS-50, test C-12 was chosen because it had the largest central pressure on the impingement plate which corresponds to the least amount of flow obstruction.

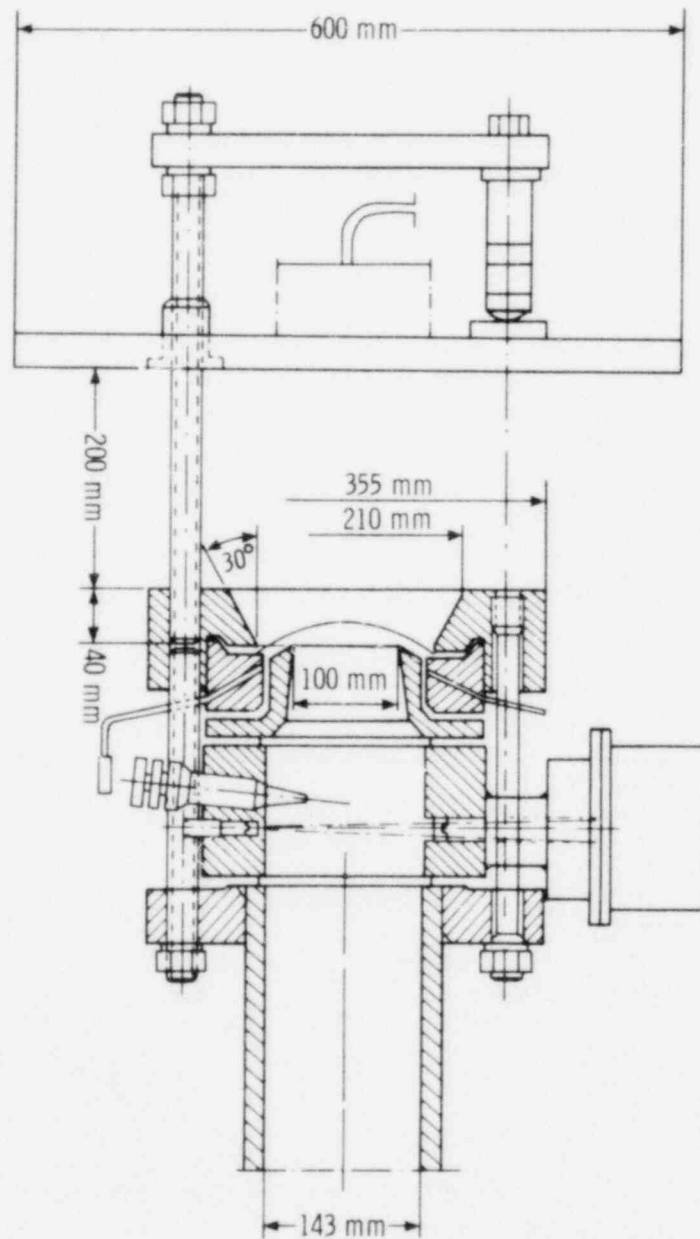


Figure 5-2. Battelle-Frankfurt RS-50 Nozzle Configuration

The TRAC-PIA six component model used for RS-50-C12 is shown in Figure 5-3.² Initial conditions for the blowdown were $P_0 = 140.5$ bars, $T_0 = 294^\circ\text{C}$, and an exit nozzle diameter of 0.10 m.

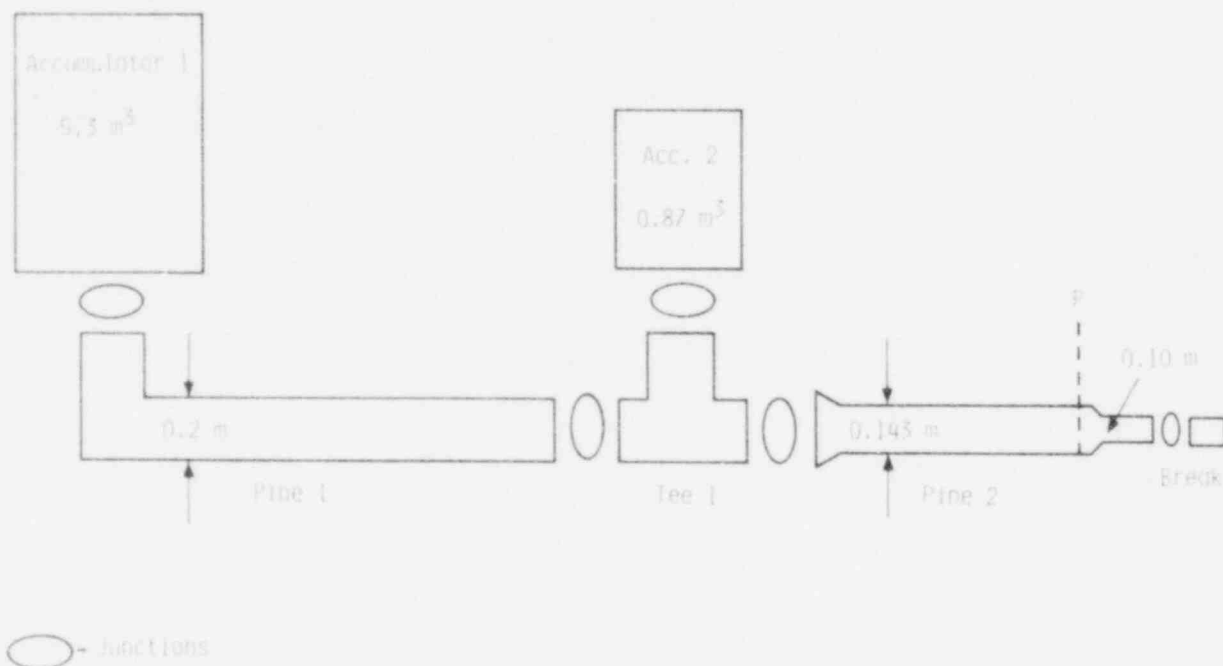


Figure 5-3. TRAC 6 Component RS-50 Model

A comparison of the calculated TRAC-PIA pressure in the exit pipe to that actually measured in the experiment is shown in Figure 5-4. Agreement with the data is very good. Some of the pressure spikes seen earlier in the experiment AL data may have been caused by measurement noise.

Figure 5-5 shows a comparison of the forces measured on the impingement plate (three discrete force transducers used - each should measure one-third of the total force if the load were symmetric) to one-third the force obtained from an extrapolation of the TRAC-PIA nozzle data, using a technique described by D. Tomasko [$F = (P_T - P_A) A + \rho V^2 A$].³ Agreement with the experimental data is fairly good. The early rapid rise seen in the TRAC-PIA load is a result of assuming a "zero-flight time" model in evaluating the force on the impingement target.

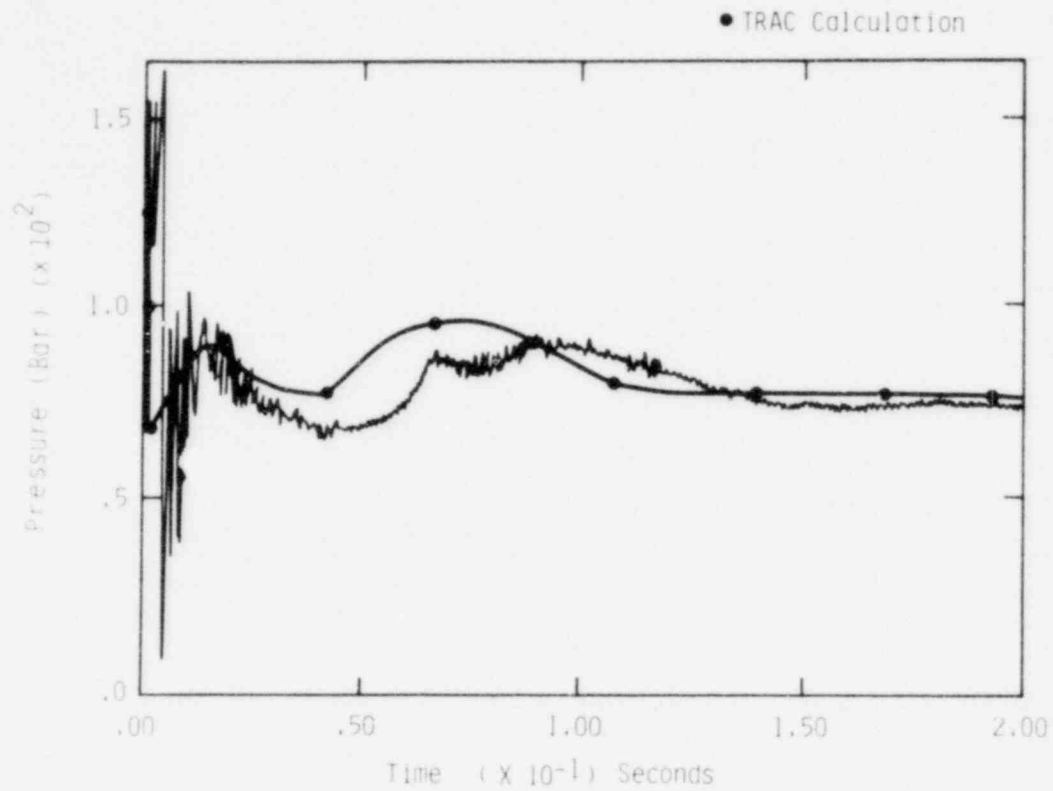


Figure 5-4. RS-50 Pressure Calculation

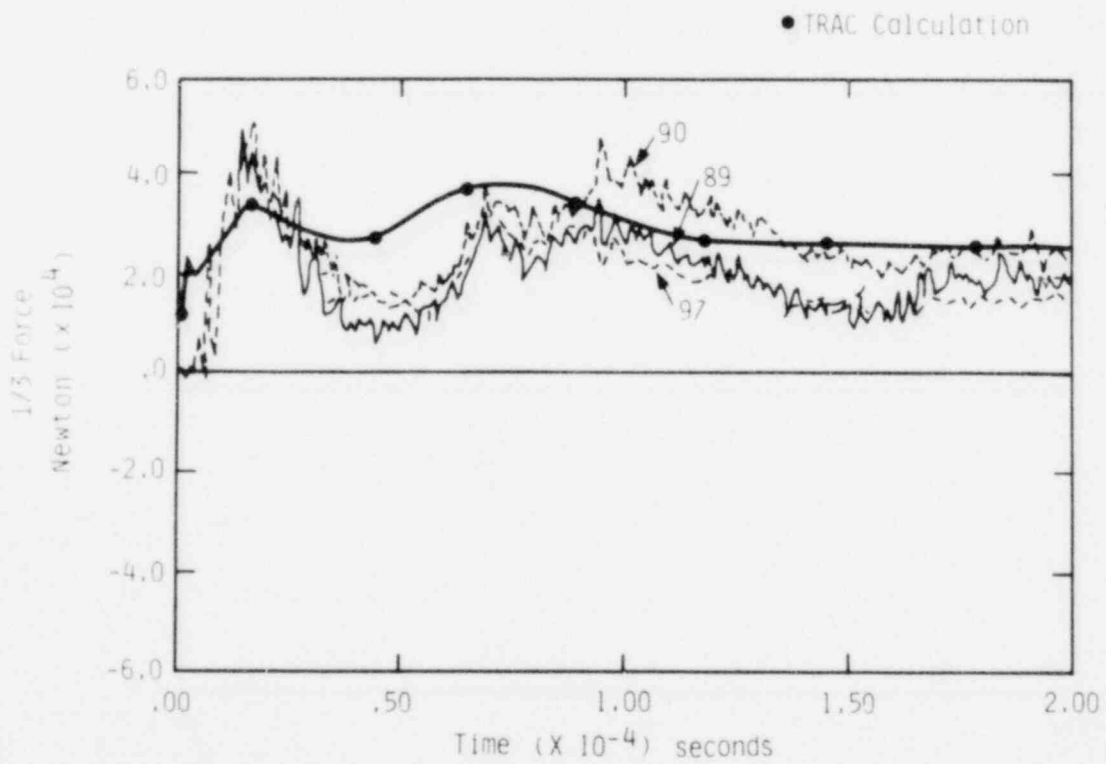


Figure 5-5. RS-50 TRAC Force Calculation

5.3 Sonic Plane Locations Using CSQ

Examination of results obtained with the Sandia computer code CSQ⁴ for blowdown tests reported previously⁵ indicates that the location of the sonic plane (Mach number = 1) occurs near the mid-point of the exit pipe ($L/2$) rather than at the pipe exit (L).

Sonic plane locations for the CSQ models shown in Figure 5-6 are shown in Figures 5-7 through 5-9. For a 1-D pipe model, the sonic plane is at the exit at time = 0.0, then travels upstream with time, and finally oscillates slowly around a pseudo-steady state location near $L/2$. This behavior is seen in Figures 5-7 and 5-8. When the exit pipe is treated as a 2-D region using five radial zones, the sonic plane assumes a parabolic shape with the average value sonic plane occurring near $L/2$, as shown in Figure 5-9.

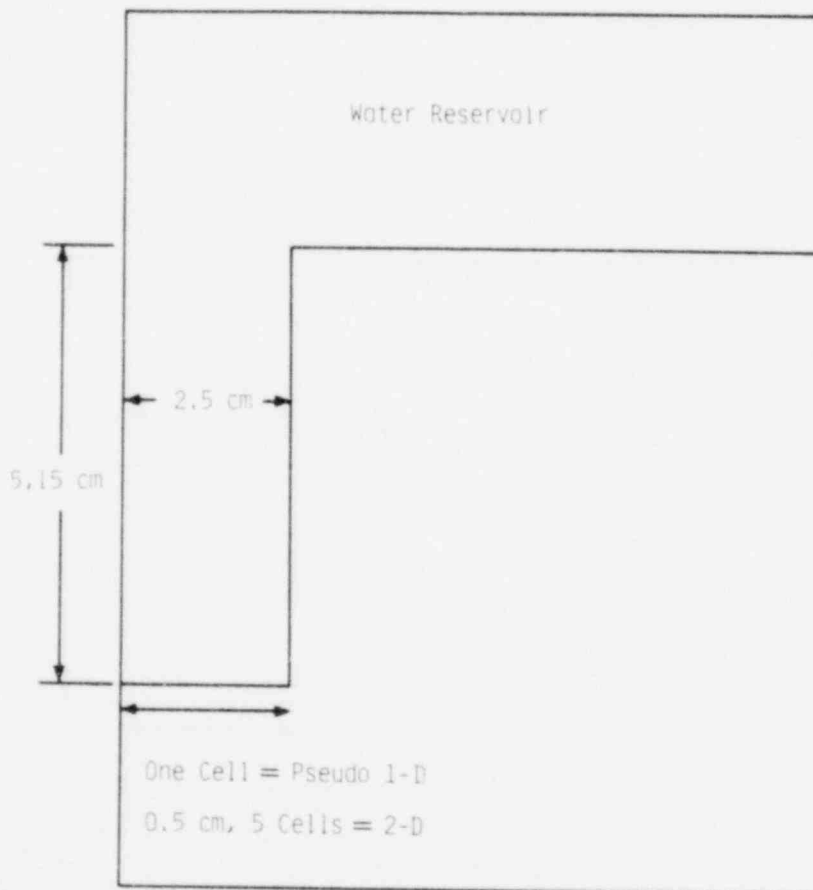


Figure 5-6. CSQ Blowdown Model

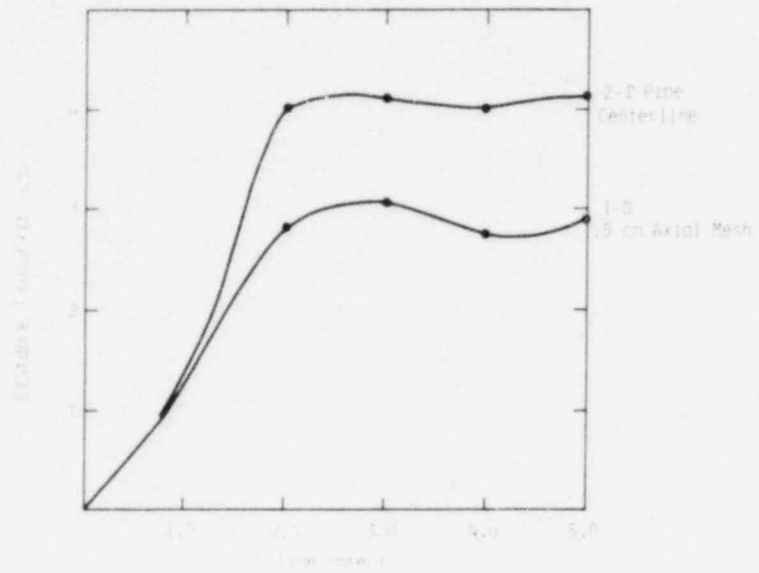


Figure 5-7. CSQ Sonic Plane Location (5-cm pipe)

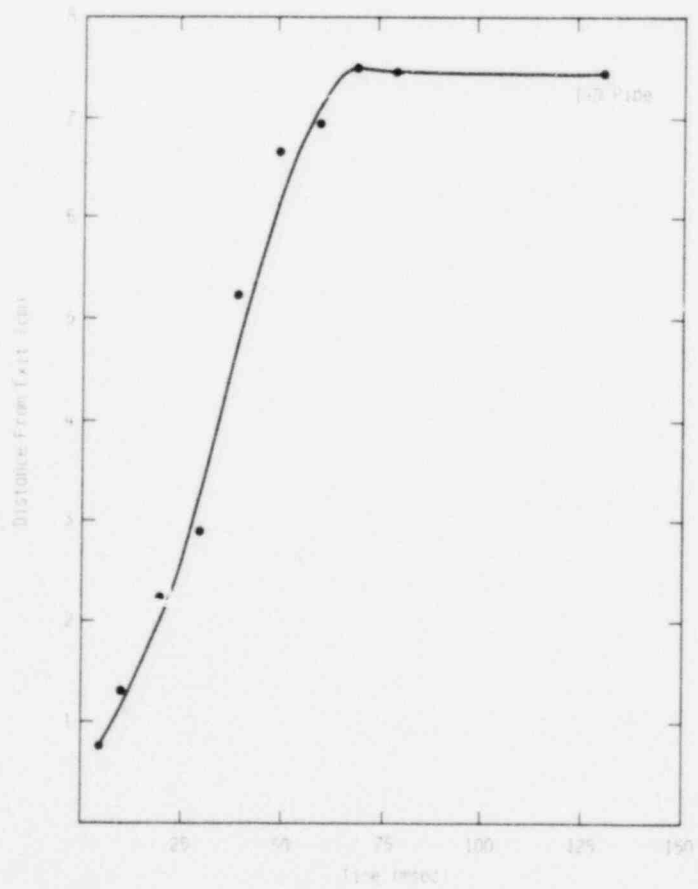


Figure 5-8. CSQ Sonic Plane Location (15-cm pipe)

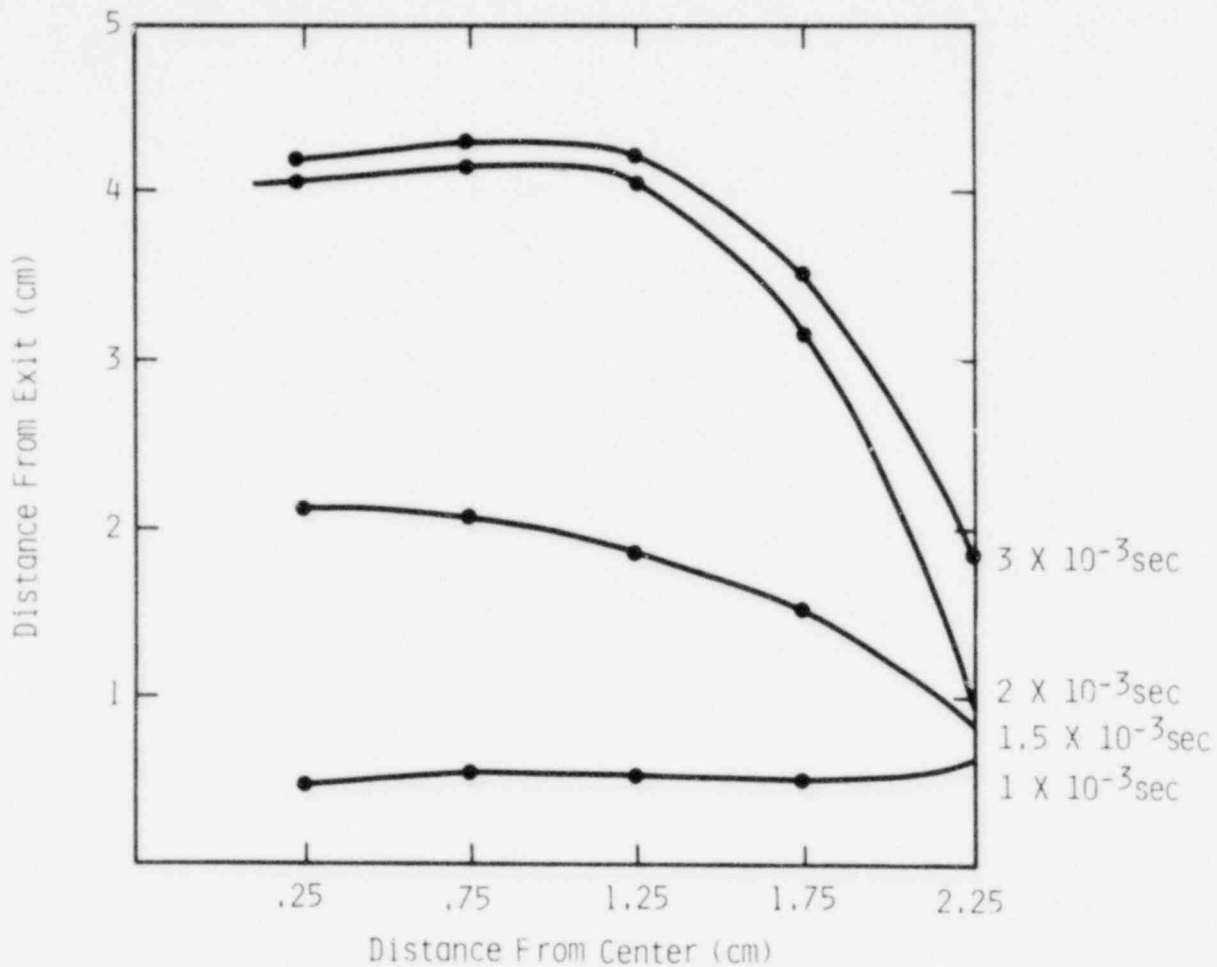


Figure 5-9. CSQ Sonic Plane Location (5-cm 2-D Pipe)

Reducing the axial mesh size by a factor of 2 (0.5 to 0.25 cm) does not significantly move the sonic plane as seen in Figure 5-10, although there is movement towards the exit and a flattening of the sonic plane profile.

The results of having the sonic plane location at $L/2$ rather than at the pipe exit are a decrease in exit pressure ($\sim 5\%$), a decrease in mass flow (1%), and an increase in mixture exit velocity to above sonic values as seen in Figure 5-11. The overall effect on the impingement load is probably small, but should be quantified, if possible.

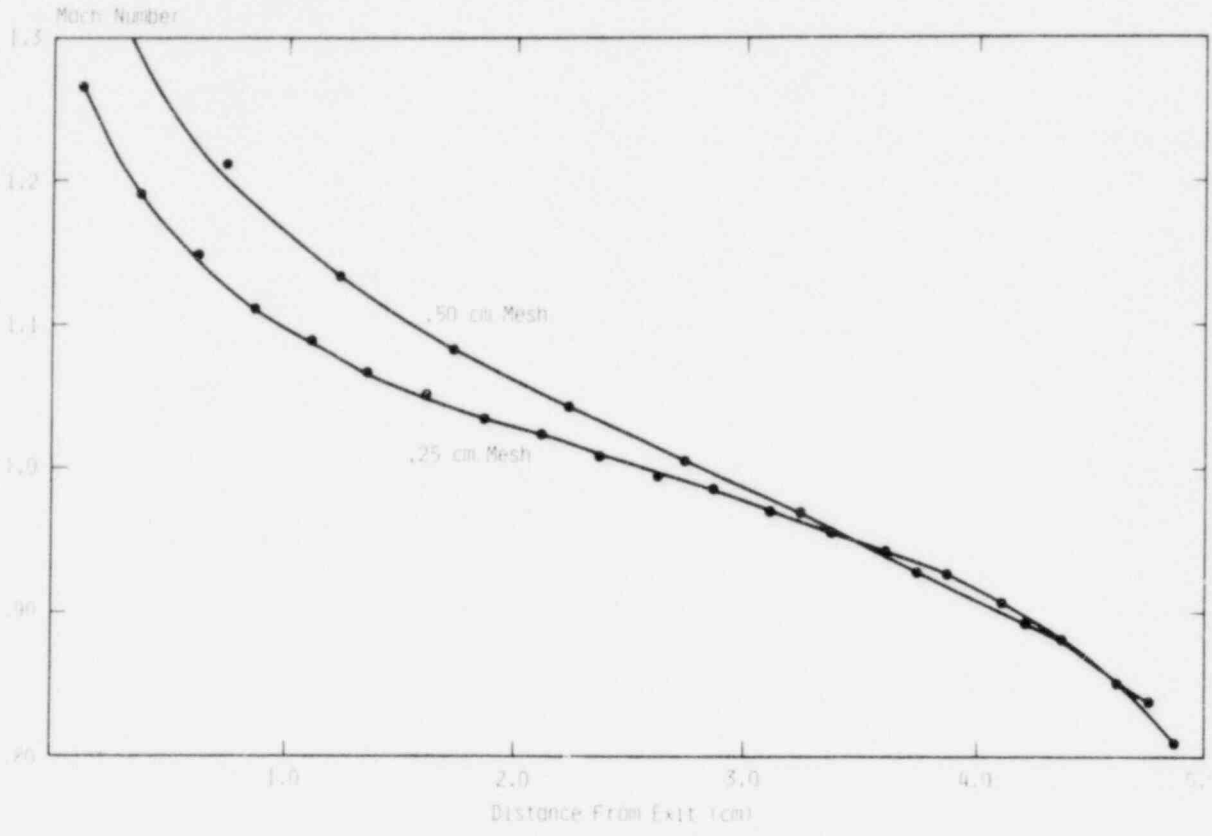


Figure 5-10. CSQ Sonic Plane Location (5-cm 2-D pipe)

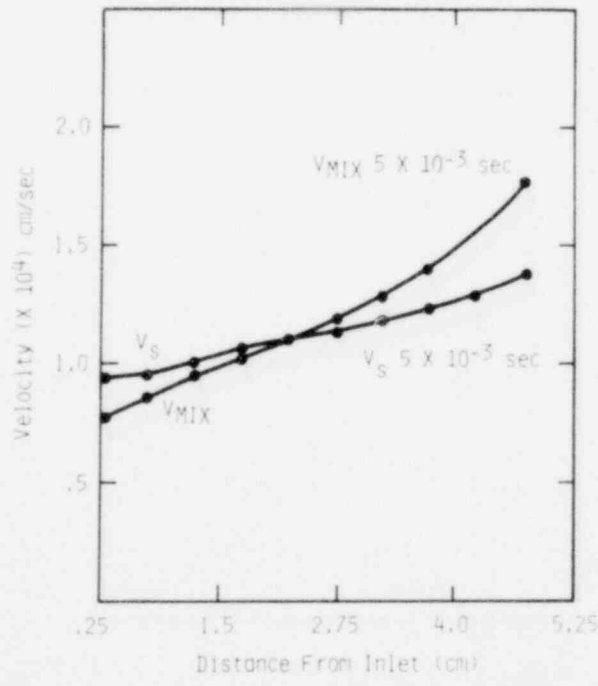


Figure 5-11. CSQ Velocities (5-cm 1-D pipe)

The sonic plane anomaly described above is not unique to CSQ; J. R. Travis et al, found a similar result with the LASL computer codes SOLA-DF and K-FIX.⁶ They found that the sonic plane could be shifted towards the pipe exit (downstream) by varying the degree of donor cell differencing through a parameter called ALPHA (ALPHA = 1.0; corresponds to complete donor cell differencing), or by using a finer axial mesh size. Best results were obtained by setting ALPHA to a value just above that required for stability.

In conclusion, future two-phase jet load studies performed with CSQ should use a fine zone axial mesh to reduce the effects of a $M \pm D$ -length choring plane. Errors introduced by this phenomenon are probably small and are currently being investigated.

5.4 Containment Modelling Using the TRAC-PIA Vessel Component

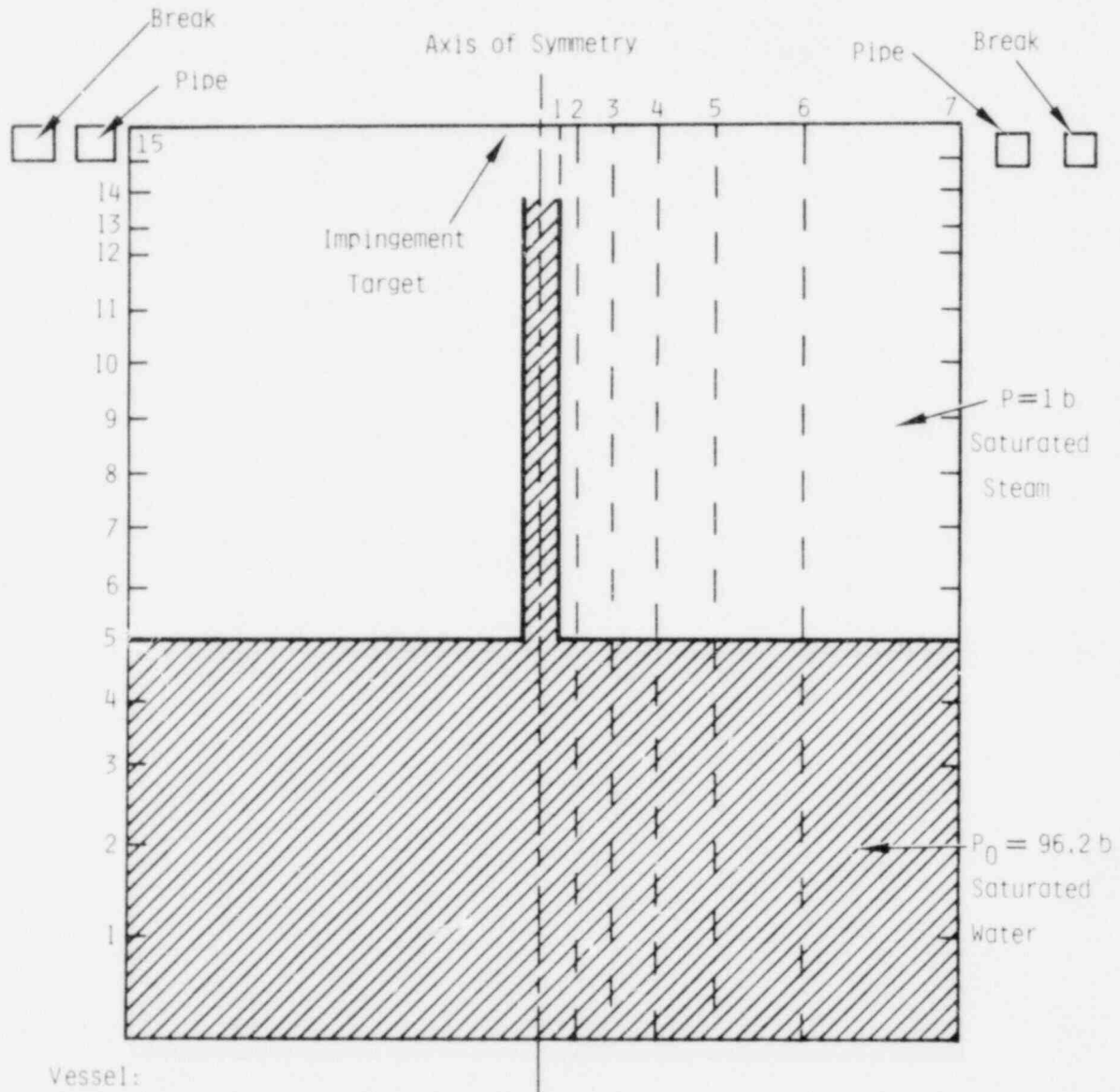
TRAC-PIA models a complex reactor system with individual components for two-phase jet load analysis. A containment component is desirable, but not currently available.

In principal, a containment model can be approximated by using a vessel without the core internals. By blocking off appropriate flow areas, complex blowdown geometries, as well as impingement targets, can be constructed. In this way, both single- and double-ended circumferential breaks and longitudinal breaks can be modelled.

Initial modelling was done for the Kraftwerk union (KWU) BMFT-RS-93 test series.⁷ In particular, test NW-50-6 was chosen as being representative.

Figures 5-12 and 5-13 show the model used to simulate the KWU test facility. This model has a vessel component with 15 axial sections, 7 rings, and 4 angles (dimensions given in Tables 5-I and 5-II). The vessel is connected to 4 pipes in the uppermost Z section (15), using the 4 cells in the outermost ring. These pipes connect to 4 breaks, thereby allowing flow out of the vessel. The upper flow area of section 15 is set to zero

to simulate an impingement target located one pipe diameter away from the pipe exit (Z section 13). The diagonally lined area represents the exit pipe and pressure vessel of the KWU test facility. Initial conditions for the pipe and vessel were 96.2 bars saturated water. The remaining volumes contained saturated steam at a pressure of 1 bar.



- Vessel:
- 15 Axial Sections
 - 7 Rings
 - 4 Angles
 - 4 Pipes
 - 4 Breaks

Figure 5-12. TRAC-PIA KWU Model

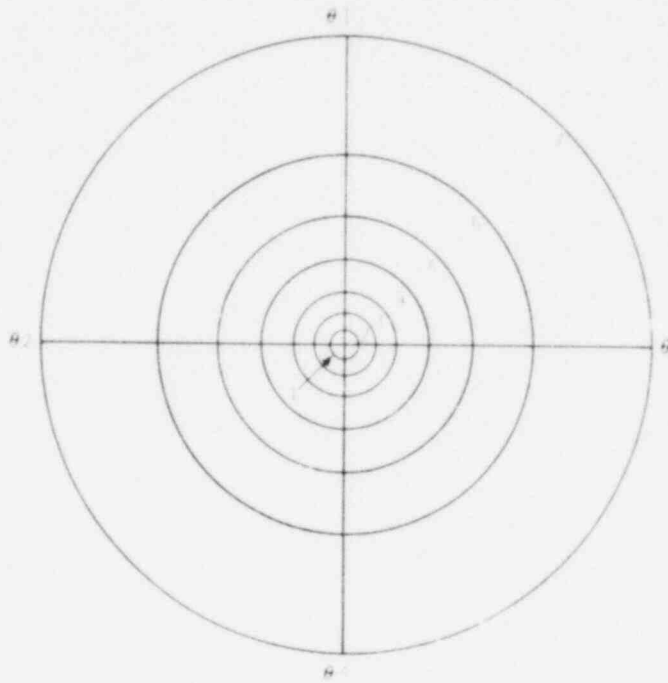


Figure 5-13. Top View of Vessel Showing
Four-Angle Seven-Ring Model

Table 5-I

Axial Segment Locations

<u>Segment</u>	<u>Top of Segment (m)</u>	<u>Center (m)</u>	<u>Segment Center to Pipe Exit (m)</u>
1	5.0	2.5	4.65
2	6.0	5.5	1.65
3	6.5	6.25	0.90
4	6.75	6.625	0.525
5	6.85	6.800	0.35
6	6.93	6.890	0.26
7	6.99	6.960	0.19
8	7.03	7.010	0.14
9	7.06	7.045	0.105
10	7.085	7.0725	0.0775
11	7.110	7.0975	0.0525
12	7.130	7.1200	0.03
13	7.150	7.14	0.01
14	7.175	7.1625	0.0125
15	7.200	7.1875	0.0375

Table 5-II
Ring Locations

<u>Ring No.</u>	<u>Location (m)</u>
1	0.025
2	0.050
3	0.10
4	0.20
5	0.40
6	0.80
7	1.60

Initial attempts to execute a blowdown from this configuration were unsuccessful due to large pressure oscillations and pressure asymmetries in axial sections 13 through 15. These were probably the result of water packing in small downstream cells in one calculational time step.

Substantial reductions in the pressure oscillations and asymmetries were achieved by modifying the time step control logic. This modification consisted of limiting the pressure change and void fraction change per cycle in any cell to a maximum value (10% change in pressure and a 20% change in void fraction). If the code attempted to exceed these limits, the current time step was reduced by a factor of 2. In addition, time step growth was inhibited if the pressure change or the void fraction change exceeded a smaller value (5% and 10%, respectively). Results obtained using the modified time step control logic are shown in Figures 5-14 through 5-26.

The effect of the maximum pressure limit allowed can be seen by comparing Figures 5-14 and 5-15. Pressure in Figure 5-14 were calculated by using a maximum differential pressure of 20% while those of Figure 5-15 used a value of 10%. For early times a reduction factor of 2 in the spike values is seen while, for times greater than 10 ms, the results are nearly identical. It should be possible to reduce the spikes further by an

additional reduction in the maximum pressure change allowed in a cycle. Figures 5-16 through 5-19 show other pressure vs time plots obtained using a maximum $\frac{\Delta P}{P}$ of 10% (cells are numbered counterclockwise starting in the innermost ring). Pressure spikes seen in Figure 5-19 (impingement plate static pressure) are much less pronounced than those of Figure 5-15 but there is still some amount of asymmetry in the calculation.

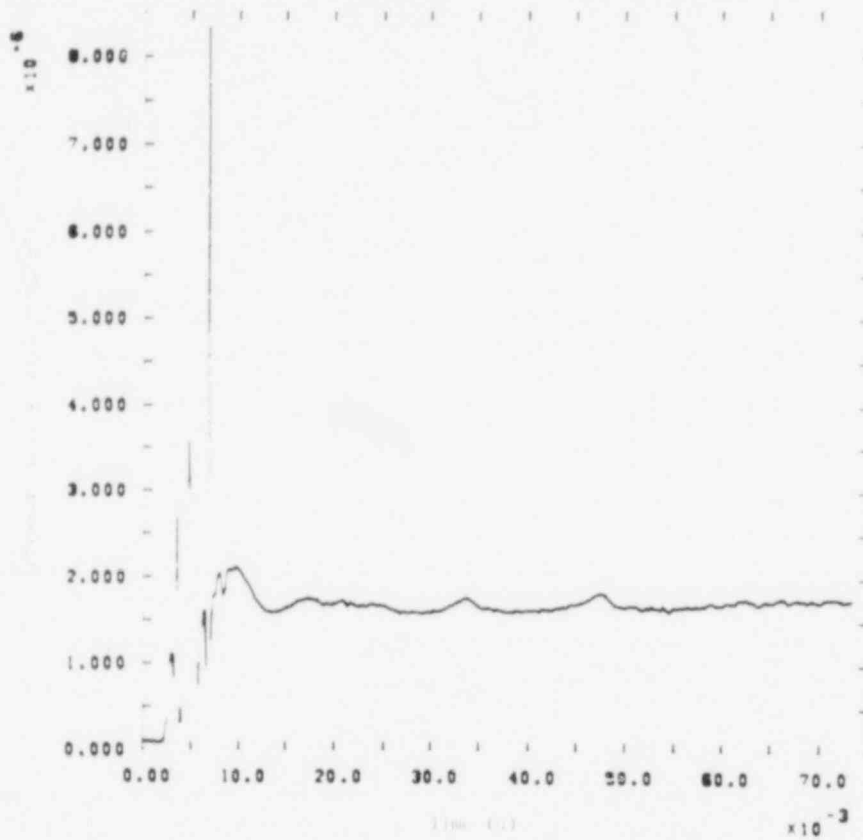


Figure 5-14. TRAC-PIA Static Pressure; Cell 4, Level 15

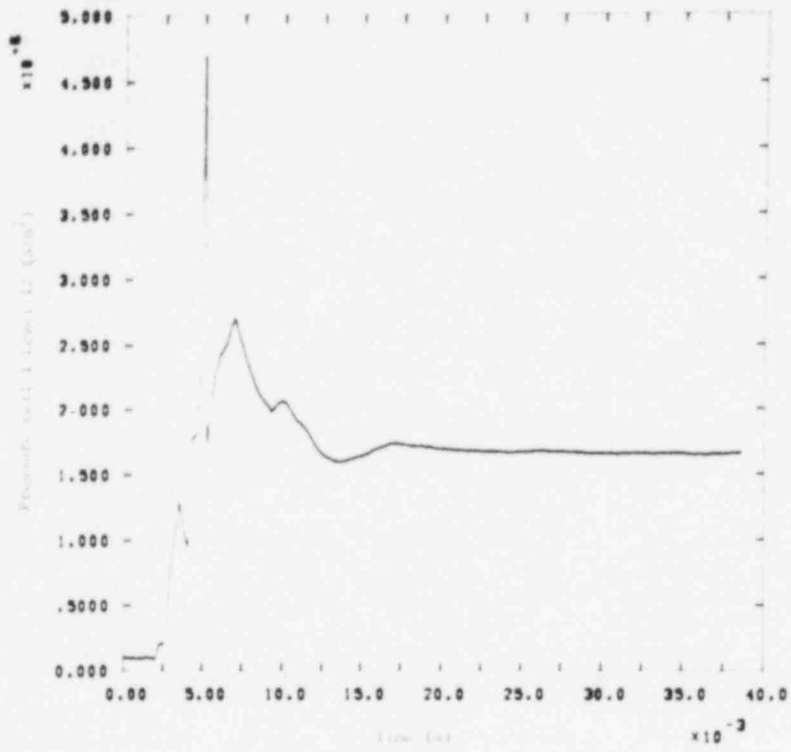


Figure 5-15. TRAC-PIA Static Pressure; Cell 4, Level 15 (Closeup)

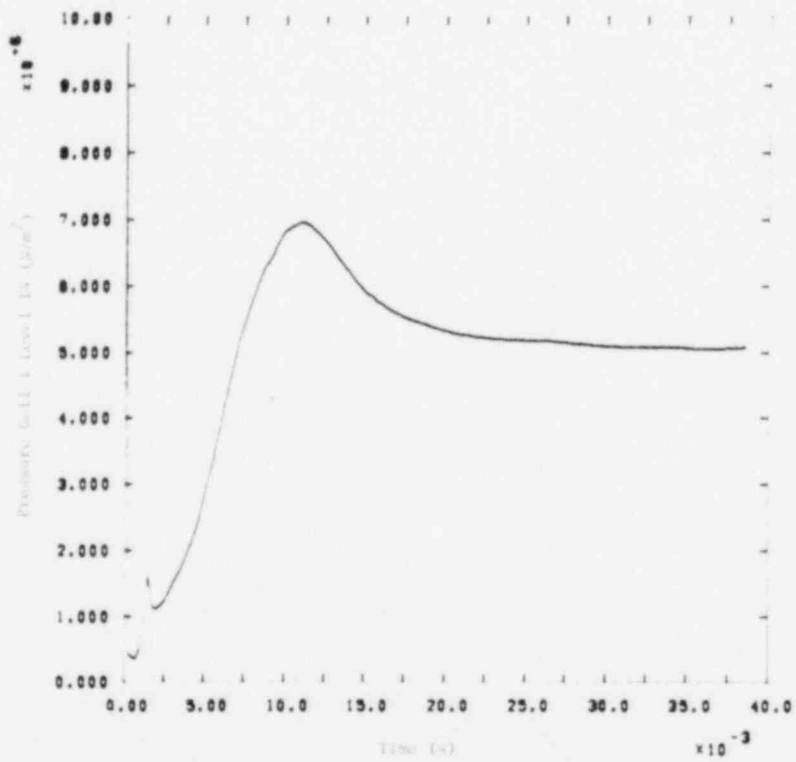


Figure 5-16. TRAC-PIA Static Pressure; Cell 1, Level 12

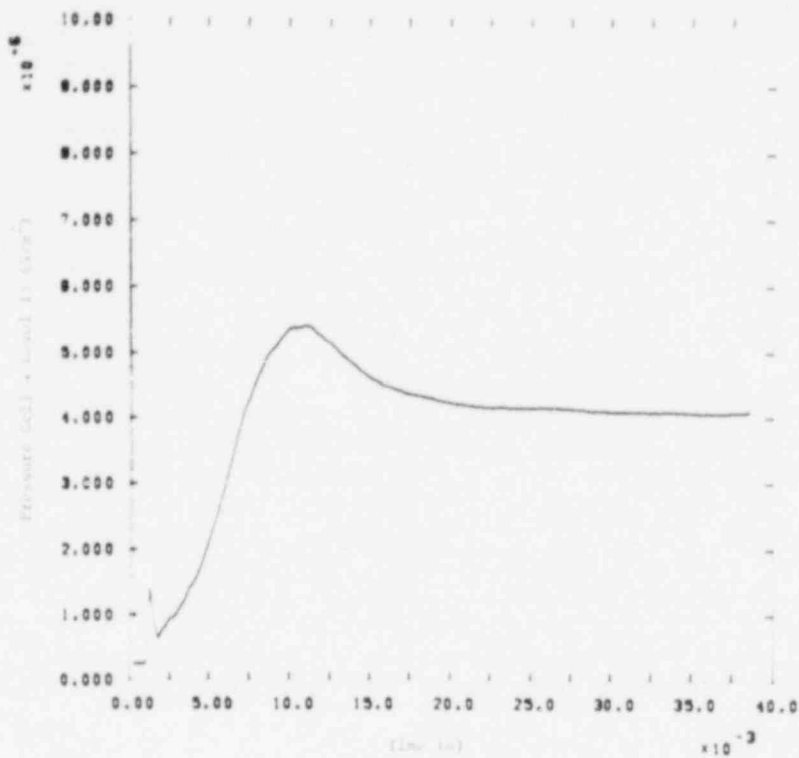


Figure 5-17. TRAC-PIA Static Pressure; Cell 1, Level 13

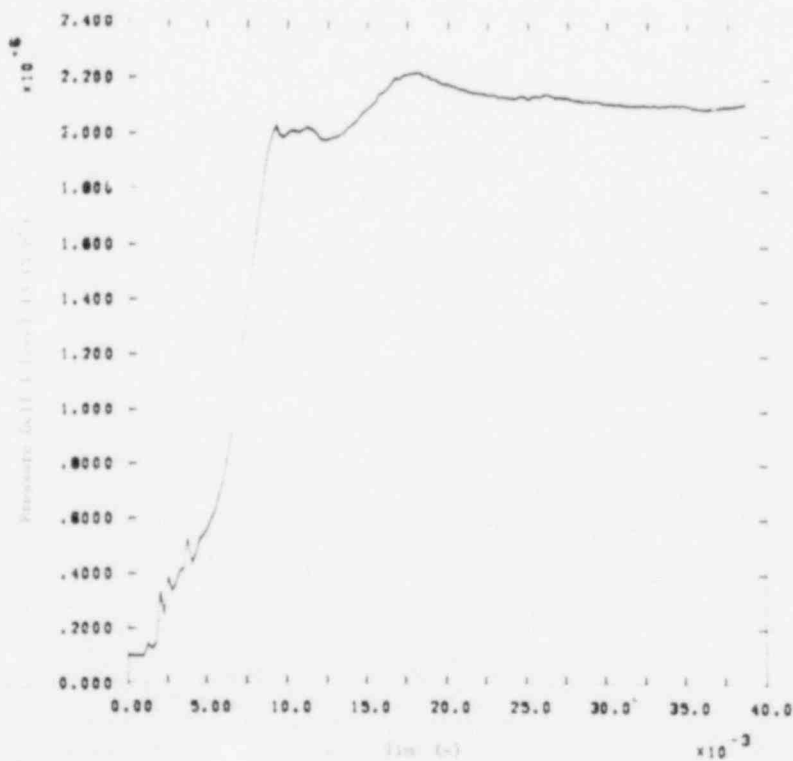


Figure 5-18. TRAC-PIA Static Pressure; Cell 1, Level 14

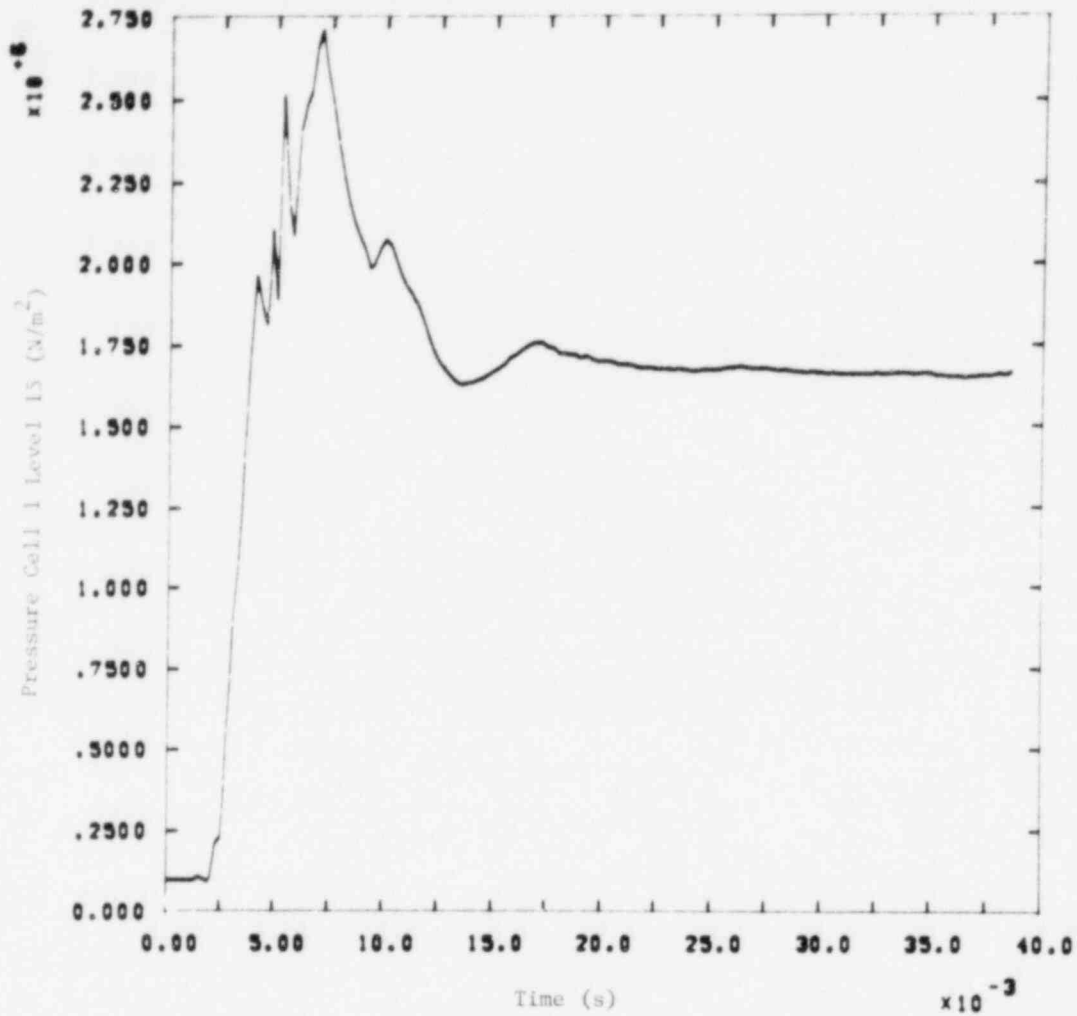


Figure 5-19. TRAC-PLA Static Pressure; Cell 1, Level 15

Dot density plots shown in Figures 5-20 through 5-23 and void fraction plots shown in Figures 5-24 through 5-26 indicate that, at ~ 5 ms, low void fraction water reaches the impingement target (superheated by $\sim 100^\circ\text{C}$). This slug of water produces water packing problems and the pressure spikes discussed earlier.

An axial pressure profile for the exit pipe is shown in Figure 5-27 at a time of 120 ms. The pressure 2 cm upstream of the break (55 bars) compares fairly well with the KWU measured value (58 bars). The calculated mass flow, however, is larger than that measured (69 kg/s vs 56 kg/s). This may be due to the combined effects of a frictionless calculation, the donor technique used, and the coarseness of the axial mesh.

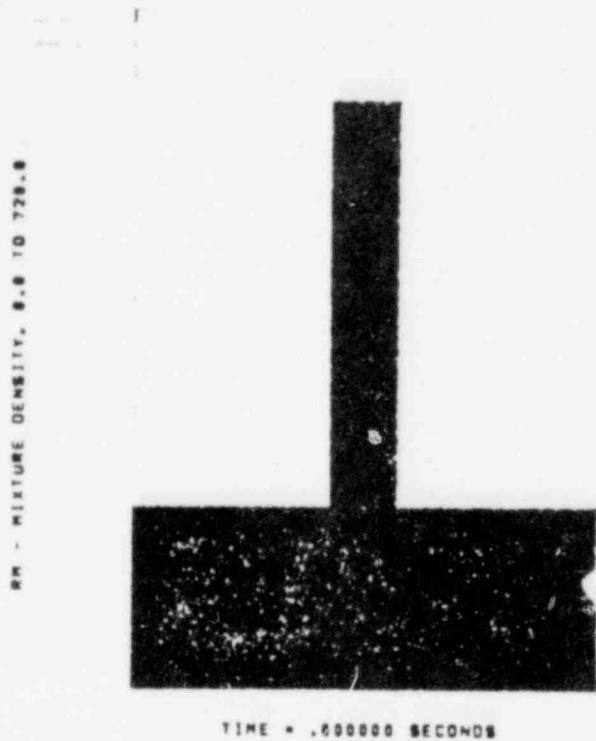


Figure 5-20. TRAC-PIA Density (0.000 s)

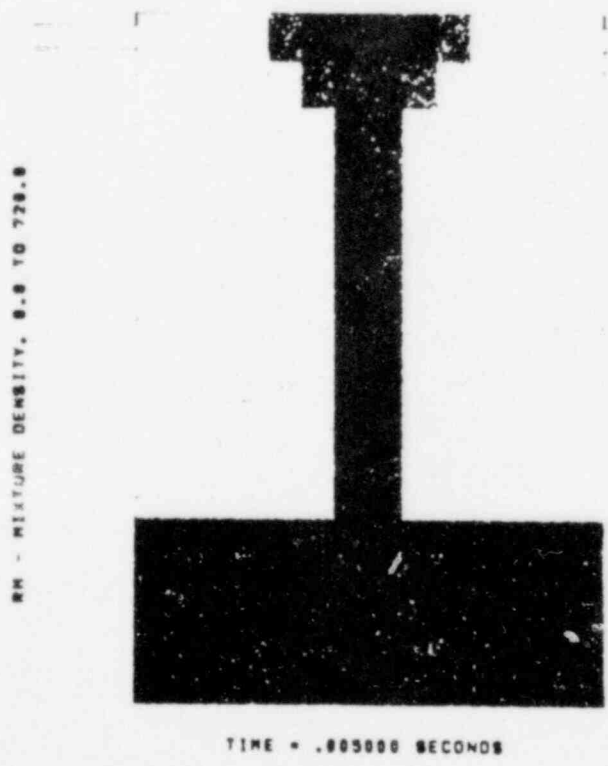
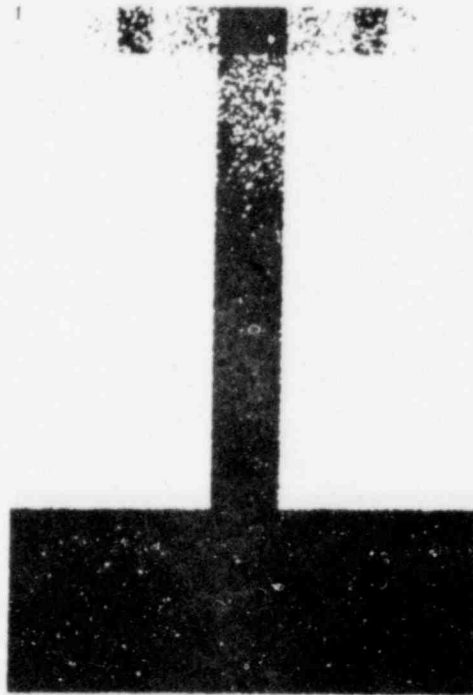


Figure 5-21. TRAC-PIA Density (0.005 s)

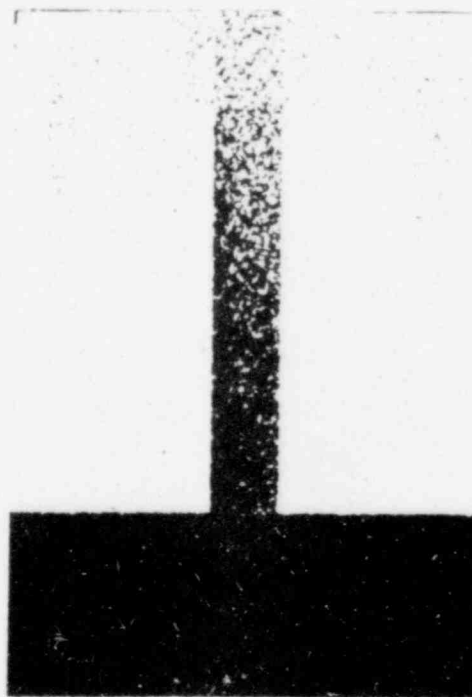
RM - MIXTURE DENSITY, 8.0 TO 728.0



TIME = .010023 SECONDS

Figure 5-22. TRAC-PIA Density (0.010023 s)

RM - MIXTURE DENSITY, 8.0 TO 728.0



TIME = .035001 SECONDS

Figure 5-23. TRAC-PIA Density (0.035001 s)

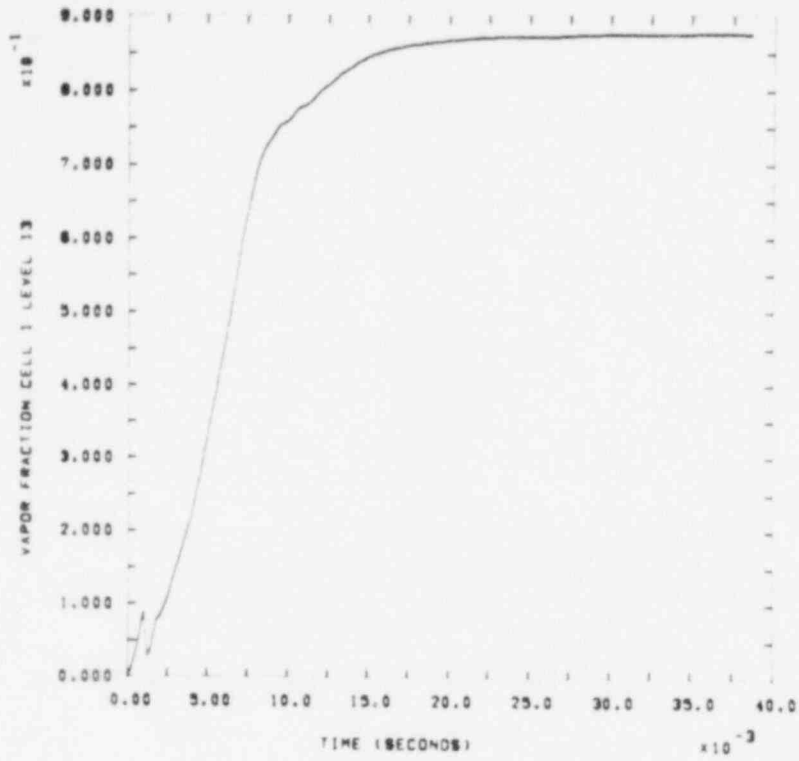


Figure 5-24. TRAC-PIA Void Fraction; Cell 1, Level 15

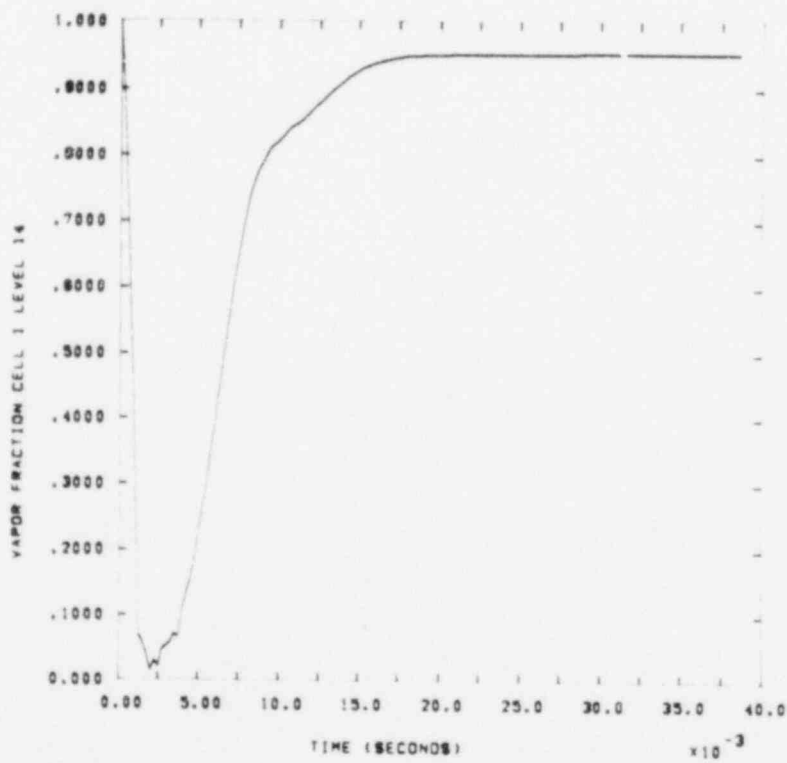


Figure 5-25. TRAC-PIA Void Fraction; Cell 1, Level 14

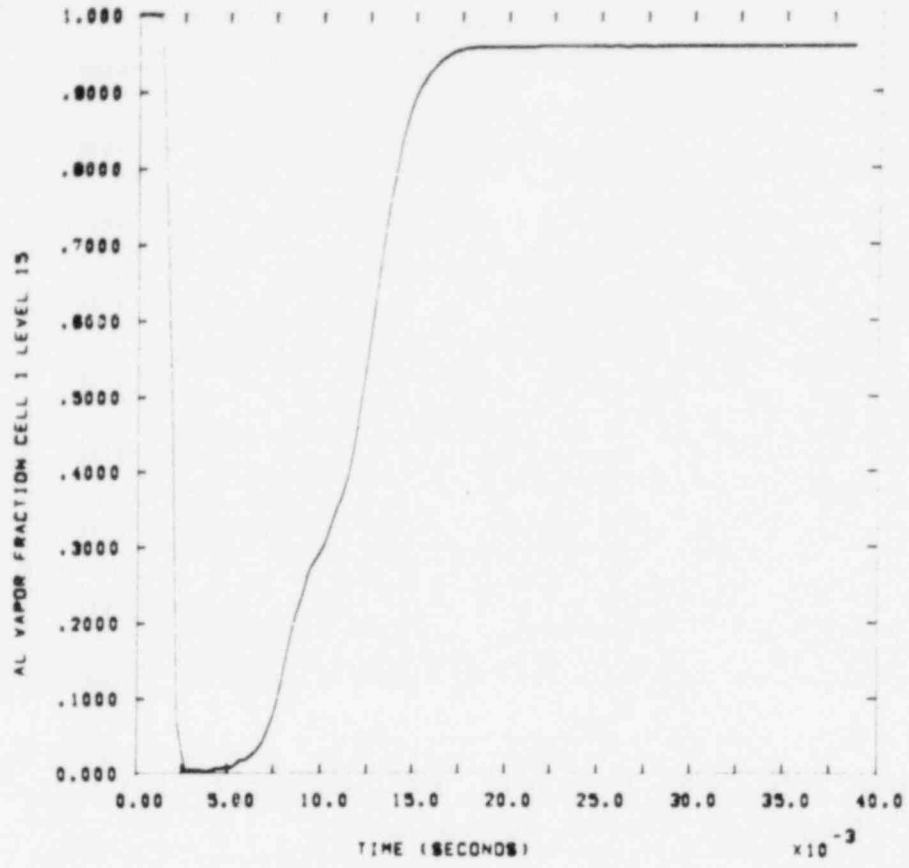


Figure 5-26. TRAC-P1A Void Fraction; Cell 1, Level 13

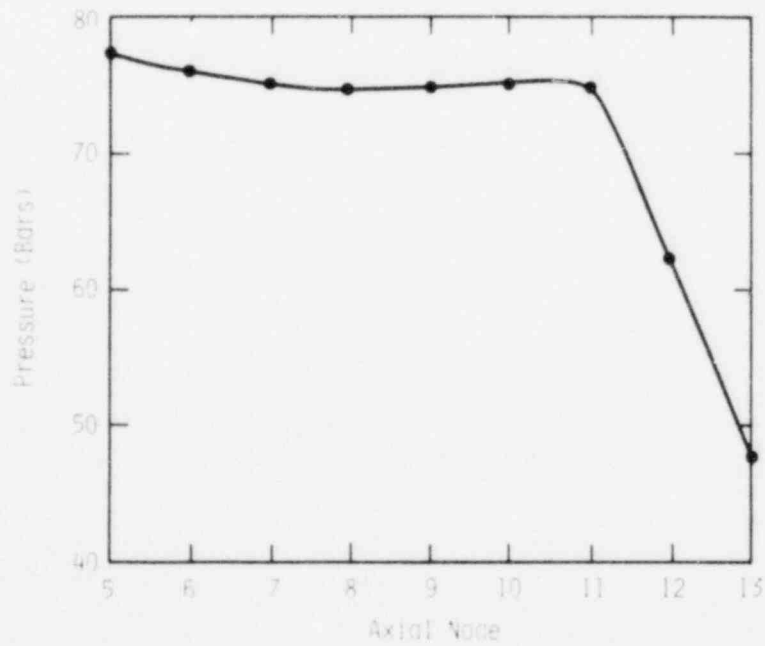


Figure 5-27. TRAC-P1A Axial Pressure Profile (T = 120 ms)

A plot showing the static pressure profile on the impingement plate at 120 ms is shown in Figure 5-28. These pressures are much smaller than those obtained by KWU ($P_{R=0} = 41$ bars). However, the KWU pressures are stagnation pressures while those of TRAC-PIA are static. Stagnation pressure plots should compare much better with the experimental data. This phenomenon is currently being investigated.

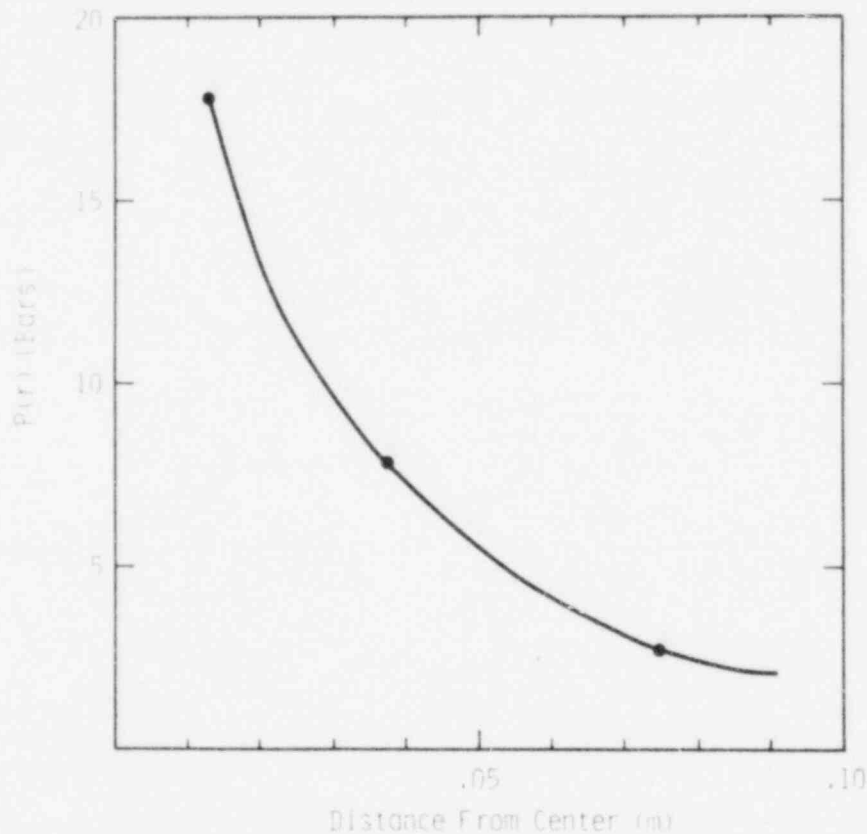


Figure 5-28. TRAC-PIA Static Plate Pressure

In conclusion, it is feasible to model blowdown facilities with the TRAC-PIA vessel component, provided that the time-step control logic is modified to reduce the effects of water packing. This will be especially important in the study of longitudinal pipe breaks which require a 3-D calculational capability.

5.5 Current and Future Work

Current and future work involve the following:

- Modelling the French blowdown facility, Canon, with TRAC-PIA (both pipe and vessel models)^(8 9)
- Investigating friction effects in vessel component modelling
- Reducing pressure oscillations and asymmetries further in the vessel component
- Modelling Canon and Battelle-Frankfurt's RS-50 with CSQ
- Performing a parameter study for PWR geometry using TRAC-PIA pipe and vessel component models

5.6 References

¹T. F. Kanzleiter, Experimental Investigation of the Jet Force and Its Local Distribution in Case of Rupture of a Primary Circuit Pipe, RS-50-62-7 (Frankfurt, Germany: Battelle Institut E.V. Frankfurt, Jan 1979).

²Safety Code Development Group, TRAC-Pl: An Advanced Best Estimate Computer Program for PWR LOCA Analysis, LA-7279-MS (NUREG/CR-0063), Vol 1 (Los Alamos: Los Alamos Scientific Laboratory, June 1978).

³D. Tomasko, Light Water Reactor Safety Research Program Quarterly Report, Jan-March 1979, SAND79-1542 (Albuquerque: Sandia Laboratories, Nov 1979), Chapter 5, "Two-Phase Jet Loads".

⁴S. L. Thompson, CSQ - A Two-Dimensional Hydrodynamic Program with Energy Flow and Material Strength, SAND74-0122 (Albuquerque: Sandia Laboratories, Aug 1975).

⁵D. Tomasko, Light Water Reactor Safety Research Program Quarterly Report, Oct-Dec 1978, SAND79-0820 (Albuquerque: Sandia Laboratories, Jul 1979), Chapter 5, "Two-Phase Jet Loads".

⁶J. R. Travis, C. W. Hirt, W. C. Rivard, "Multi-Dimensional Effects in Critical Two-Phase Flow," Nuc Sc Eng 68:338-48(1978).

⁷R. Eichler et al., Studies on Critical Two-Phase Flow, NRC-477 (Washington: U.S. Nuclear Regulatory Commission, Sep 1978).

⁸B. Riegel, Contribution A L'Etude De La Decompression D'une Capacite En Regime Diphasique (Grenoble, France: L'Institut National Polytechnique De Grenoble, June 1978).

⁹J. C. Rousseau and B. Riegel, "Blowdown Exercises," European Two Phase Flow Meeting, Grenoble, June 1977, HTFS24541 (Grenoble, France: L'Institut National Polytechnique de Grenoble, nd). To be published.

DISTRIBUTION:

US Nuclear Regulatory Commission
(375 copies for R3)
Division of Document Control
Distribution Services Branch
7920 Norfolk Ave
Bethesda, MD 20014

US Nuclear Regulatory Commission (6)
Office of Nuclear Regulatory Research
Washington DC 20555
Attn: W. C. Lyon
N. Zuber
S. Fabric
C. E. Johnson
R. R. Sherry
M. Vagins

US Nuclear Regulatory Commission (3)
Division of Systems Safety
Office of Nuclear Reactor Regulation
Washington, DC 20555
Attn: B. Sheron
N. Lauben
E. Throm

U.S. Department of Energy
Operational Safety Division
Albuquerque Operations Office
P. O. Box 5400
Albuquerque, NM 87185
Attn: J. R. Roeder, Director

Westinghouse Electric Corp
Research and Development Center
Churchill Boro
Pittsburgh, PA 15235
Attn: M. Mazumdar
Mathematics Dept

Florida International University
Department of Statistics
Tamiami Trail
Miami, FL 33144
Attn: S. S. Shapiro

EG&G - Idaho, Inc (2)
P. O. Box 1625
Idaho Falls, ID 83401
Attn: N. D. Cox
D. M. Snider

Electric Power Research Institute
3112 Hillview Ave.
Palo Alto, CA 94304
Attn: J. Carey

Offshore Power System
8000 Arlington Expressway
Box 8000
Jacksonville, FL 32211
Attn: D. H. Walker

Prof. S. Abdul-Kalik
Nuclear Engineering Dept
University of Wisconsin
Madison, WI 53706

Dr. S. G. Bankoff
Chemical Engineering Dept
Northwestern University
Evanston, IL 60201

Westinghouse Advanced Reactor Div
P. O. Box 158
Madison, PA 15663
Attn: L. E. Strawbridge

Westinghouse Electric Corp (2)
Bettis Atomic Power Lab
P. O. Box 79
West Mifflin, PA 15122
Attn: W. D. Peterson
F. W. Lincoln

Westinghouse Electric Corp (2)
Nuclear Energy Systems
P. O. Box 355
Pittsburgh, PA 15230
Attn: R. P. Vijuk
M. Y. Young

Los Alamos Scientific Lab (2)
P. O. Box 1663
Los Alamos, NM 87545
Attn: M. McKay
J. Jackson

DISTRIBUTION (cont):

400 C. Winter
 1200 L. D. Smith
 1223 R. B. Easterling
 1223 I. J. Hall
 1537 N. R. Keltner
 2514 D. E. Mitchell
 4400 A. W. Snyder
 4410 D. J. McCloskey
 4412 J. W. Hickman
 4420 J. V. Walker
 4421 R. L. Coats
 4422 D. A. Powers
 4422 D. W. Varela
 4423 P. S. Pickard
 4425 W. J. Camp
 4440 G. R. Otey
 4441 M. Berman (10)
 4441 R. K. Cole, Jr.
 4441 J. F. Muir
 4441 M. L. Corradini
 4442 W. A. Von Rieseman
 4443 D. A. Dahlgren
 4444 L. D. Buxton
 4444 R. K. Byers
 4444 B. W. Burnham
 4444 D. Tomasko
 4450 J. A. Reuscher
 4533 B. D. Zak
 4550 R. M. Jefferson
 4732 H. J. Sutherland
 5131 W. B. Benedick
 5512 D. W. Larson
 5520 T. B. Lane
 5530 W. Herrmann
 5534 J. F. Assay
 5534 J. E. Smaardyk
 5623 D. J. Rigali
 5623 B. M. Bulmer
 5641 G. P. Steck
 5830 M. J. Davis
 5836 J. L. Ledman
 5836 L. S. Nelson
 5836 F. J. Zanner
 5846 E. K. Beauchamp
 5846 R. A. Sallach
 8266 E. A. Aas
 3141 T. L. Werner (5)
 3151 W. L. Garner (3)
 For: DOE/TIC (Unlimited Release)
 3154-3 R. P. Campbell (25)
 For NRC Distribution to NTIS